High Speed Fiber Optic Spectrometer

Yongxin Wang

Dissertation submitted to the committee members of Yongxin Wang
in partial fulfillment of the requirements for the degree of

Doctor of Philosophy
in
Electrical and Computer Engineering

Dr. Anbo Wang, Chair
Dr. Ira Jacobs
Dr. Yilu Liu
Dr. Yong Xu
Dr. Gary R Pickrell
Dr. Guy J Indebetouw

December 10, 2007
Blacksburg, Virginia

Keywords: Spectrometer, Spectrometry, Spectroscope, Spectroscopy, Signal processing,
Fiber Optics, Fiber Optic Sensor

High Speed Fiber Optic Spectrometer

Yongxin Wang

(ABSTRACT)

This dissertation presents the structure, operational principle and mathematical model of a novel high speed fiber optic spectrometer (HSFOS). In addition, the performance analysis is conducted and preliminary experimental results are listed and discussed. Such a spectrometer is highly desired by the ever-increasing applications of fiber optic sensors.

In the recent decades, a variety of fiber optic sensors have been proposed, built and tested. Compared to their electronic counterparts, fiber optic sensors although still under development, are preferred more by certain industrial and medical applications which benefit from their unique properties such as immunity to electromagnetic interference, ability to withstand harsh environments and composition of purely dielectric materials. In recent years, new fiber optic sensors have been designed for applications where high response frequency up to a few hundred *KHz* is required while advantages of high accuracy and large dynamic range must be maintained. The bottle neck then emerged in the signal demodulation part of the sensor system. The quadrature phase detection could achieve high demodulation speed but with small dynamic range, medium accuracy and measurement ambiguity. The white light interferometry could provide a solution for high accuracy and large dynamic range measurement without ambiguity because of its absolute measurement nature. However the signal demodulation speed is limited due to the low spectrum acquisition rate of the existing spectrometers.

The new HSFOS utilizes time domain dispersion of the sampled incoming light by dispersive fiber rather than the spatial dispersion employed by traditional spectrometers. In addition the signal that represents the spectrum of the light is naturally a serial signal which can be detected by a single detector and recorded by a high speed data acquisition device. Theoretical study of the operation principle is made and a mathematical model for the spectrometer

is developed based on Marcuse's previous work. One major difference of the new derivation is that the propagation constant is expanded about the center circular frequency of each monochromatic light pulse instead of the center frequency of the chromatic light pulse which makes the physical picture of the chromatic light pulse evolution in a dispersive fiber clearer and facilitates both the analytical and numerical analysis. The profile of the dispersed chromatic light pulse could be treated as the superposition of all the dispersed monochromatic light pulses. Another major difference is the Taylor's series of the propagation constant is not truncated as it is in those previous work, which improves the accuracy of the model. Moreover, an approximate model is made which could further reduce the computation tasks in numerical simulations. Performance analysis for accuracy, resolution, speed and noise are conducted through numerical simulations based on the model and the experimental results. The sources of two different errors and their effects on accuracy are discussed respectively. The effects on spectral resolution by the properties of the modulation pulse and the fiber dispersion are studied. The results indicate that by using a rectangle modulation pulse under certain conditions, the resolution can be improved. The speed analysis gives that the spectrum acquisition rate can reach 1 million frames per second when the spectral width is less than 100 nm. In the noise analysis, the erbium-doped fiber amplifier (EDFA) is determined to be the dominant noise source. But by using two EDFAs, the overall signal to noise ratio is improved by 9.2 dB. The preliminary experimental results for FP sensor and FBG sensor signal demodulation are presented. The HSFOS for FP sensor signal demodulation achieves 15 nm resolution. By using the oversampling method, the HSFOS for FBG sensor signal demodulation achieves 0.05 nm spectral positioning resolution.

Dedication

To my grandparents, Zongsu Wang and Huijun Jin

for the strength you gave to me

for the faith you brought to me

Acknowledgments

I would like to express my deepest gratitude to Dr. Anbo Wang, my adviser, for his continuous guidance, support and for his encouragement through my study and research at Center for Photonics Technology. He provide me a good opportunity to learn how to become a researcher from a student. In the past four years, through countless illuminating discussions, he helped me to become more productive and more self-confident when facing difficulties. Further, his spirit of optimism and adventure influence me a lot. I sincerely thank him for being a wonderful mentor and a friend.

I would also like to thank other committee members, Dr. Ira Jacobs, Dr. Yilu Liu, Dr. Yong Xu, Dr. Gary R Pickrell, and Dr. Guy J Indebetouw for serving on my committee and for their valuable help and suggestions. I would like to thank Dr. Ahmad Safaai-Jazi for his encouragement and suggestions, and Dr. Kristie L Cooper for her help in the past four years. I am also grateful to Debbie Collins for her help. She did a lot for all of us and her help really makes our everyday lives easier. I would like to give my special thanks to Dr. Juncheng Xu for his help in sensor fabrications and the 14 year's friendship. My gratitude also goes to Dr. Ming Han for the friendship and suggestions. My thanks also go to all my friends here at Center for Photonics Technology, including those former members Dr. Yan Zhang, Dr. Bing Yu, Dr. Zhuang Wang, Dr. Xiangwei Wang, Dr. Yizheng Zhu, Dr. Zhenyu Huang, Dr. Po Zhang, Dr. Xiaopei Chen, Xin Zhao and Dr. Dawoo Kim and the current members, Bo Dong, Evan Lally, Jiajun Wang, Cheng Ma, Yaoshun Jia, Xiangyu Wei, Yunmiao Wang, Yunjing Wang and Yan Yin. I would like to express my gratitude

to all my friends in Blacksburg. I would like to thank Dr. Chengyu Cao and Jianqiu Liu. We shared a lot of joyful time together. In addition, Chengyu provided lots of help and suggestions to me. My thanks also go to Chao Huang for the 8 year's friendship. We met again in Blacksburg in 2005 and we have shared many joyful time since then.

Finally, I would like to thank my parents who gave me birth, raised me, trust me and support me. I would also give my gratitude to my uncle Duan Jin for his help.

Contents

List of Figures

List of Tables

Chapter 1

Introduction

1.1 Fiber optic sensors

Sensors are a type of physical device through which information about our surrounding world that could not be directly measured and recorded, i.e. the measurands, are transfered or converted to other types of information that could be directly processed, i.e. the output from the sensor. Fiber optic sensors vary the parameters, such as phase, spectrum and polarization, of the light propagating in the optical fibers according with the target measurands, including physical and chemical parameters. Two categories of fiber optic sensors, intrinsic and extrinsic, have been developed during the past three decades due to their unique properties:

- Immunity to electromagnetic interference
- Resistance to harsh environments
- Outstanding chemical stability
- Possibility of miniaturization
- Capability for distributed sensing

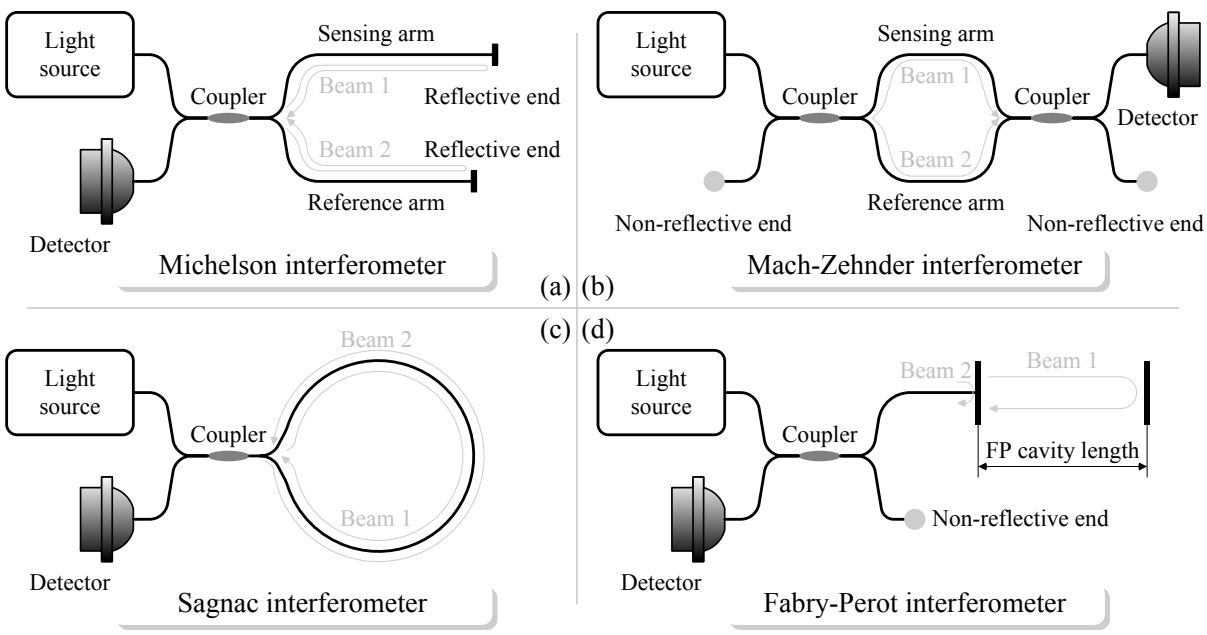

Figure 1.1: Structures of different interferometers

- Composed solely of dielectric materials

Intrinsic fiber optic sensors utilize the optical fiber as the sensing element which reacts with the measurands whereas extrinsic ones just transmit the light signal through the optical fibers and let other parts in the sensor vary the light properties according to the measurands. One example of intrinsic fiber optic sensors is the Fabry-Perot (FP) interferometric temperature sensor developed in our laboratory based on measuring the temperature induced expansion of the optical fiber within the FP cavity [1]. For the extrinsic ones, the diaphragm based pressure sensor for jet engine measurement designed in our laboratory is a good example [2].

Many principles and structures could be applied to build fiber optic sensors. For those sensors based on light interference, interferometers of different types: Michelson, Mach-Zehnder, Sagnac, or FP could be formed for various measurement purposes as shown in Fig.1.1. Among them, the FP interferometer is widely used due to its advantages of simple structure and

small size. In addition, the selection of the cavity and the reflection surfaces is flexible which accommodates the achievement of detecting different measurands with different frequency responses. For example, in a diaphragm based fiber optic FP sensor, when pressure is the measurand, the diameter of the diaphragm could be increased and the thickness could be reduced to achieve higher sensitivity while at the same time lowering the interference from the external surface of the diaphragm which introduces a temperature dependent noise. Under this condition, the two reflection surfaces are the fiber end and the inner side of the diaphragm and the cavity is the space between the two surfaces. When temperature is the measurand, through increasing the thickness and reducing the diameter of the diaphragm together with shortening the length between the fiber end and the diaphragm, high sensitivity to temperature is realized. The interference from air cavity with pressure dependence is minimized. Under this condition, the two reflection surfaces are the two sides of the diaphragm and the cavity is formed by the diaphragm. The first three types of interferometers have polarization induced fading due to the two beams which form the interferogram going through different optical path or through the same optical path but in different directions. The FP interferometers have low polarization induced fading due to the fact that the FP cavity is very short, e.g. several tens of micrometers. This cavity is the only difference between the optical paths of the two light beams interfering with each other. However, the extrinsic FP sensor suffers the fading caused by the high coupling loss and imperfection of the reflection surfaces induced intensity mismatch of the two beams.

In the Michelson, Mach-Zehnder, and FP interferometers based fiber optic sensors, the measurands vary the optical path length of the sensing arm (for Michelson and Mach-Zehnder interferometers) or the cavity length (for FP interferometers) in the sensor thus the difference between the optical paths through which the two light beams travel is changed such that the interferogram from the sensor is then changed which is seen as the output of the sensor corresponding to the measurands. Fiber optic sensors based on Sagnac interferometers are unique. The two light beams travel through the same optical path but in opposite directions. Mostly, they form a special group of sensors, fiber optic gyroscopes, which detect angular

velocity through Sagnac effects.

Fiber grating sensors including fiber Bragg grating (FBG) sensors and long period grating (LPG) sensors are usually made of photo-sensitive optical fibers. Their fiber cores have periodically varying reflective indices along the fiber which form the grating. By using masks, the manufacturing process is easily repeated with high precision which is one advantage of fiber grating sensors over other fiber optic sensors. They are good for strain and temperature measurement. By coating fiber grating sensors with magnetostrictive materials or electrostrictive materials, new sensors are made which could detect magnetic or electric field.

Other effects could also be used to make fiber optic sensors. For example the scattering such as Rayleigh scattering, Brillouin scattering, Raman scattering. They are often applied for distributed sensing where the optical fiber without any manipulation is the sensor, and intensity or the spectrum of the scattering from each point of the fiber reflects the strain or temperature at that point.

In the last decade, several high performance fiber optic sensors have been developed for new applications in which no sensors were available before. The fiber optic FP sensor for partial discharge detection could be put into high voltage power transformers for the partial discharge detection which is critical for safe operation of the transformers [3]. The diaphragm based pressure sensor could be put into jet engine to test the static and dynamic pressure inside the engine which is a great help for the manufacture to design and optimize the engine [2]. In tests for both applications, the fiber optic sensors worked well. In contrast, the harsh environments with severe electromagnetic interference and very high ambient temperature cause unacceptably low signal to noise ratio of the output signal from those traditional electronic sensors, or even the failure of the sensors. To further improve the results, the two applications require the sensors and the signal processing system have high response speed which should be at least 100 KHz while at the same time achieving large dynamic range and high accuracy. However the existing signal processing system can not meet these needs.

1.2 Signal processing for fiber optic sensors

This section will be focused on signal demodulation of fiber optic FP sensors and FBG sensors. For FP sensors built with single mode fibers, the signal processing methods can be divided into two types, the relative demodulation methods and absolute demodulation methods. The former includes the traditional phase demodulation method known as the fringe counting method and the intensity demodulation method known as the quadrature phase detection. For the fringe counting method, a monochromatic light source with wavelength λ_0 is used to illuminate the FP sensor. The intensity of the output light signal from the sensor is a function of cavity length d expressed as:

$$I(d) = I_m \cos\left(\frac{4\pi d}{\lambda_0} + \varphi_0\right) + I_0, \tag{1.1}$$

where I_m is the amplitude of the AC part in signal, I_0 is the constant DC part in the signal, and φ_0 is an arbitrary initial phase which is treated as a constant for a specific sensor.

Since the intensity of the light signal is not a linear function of the cavity length in each period, the detector in the signal demodulation system ignores the amplitude information and only counts the number of the periods encountered during the variation of the cavity so that the relative cavity length change is determined with a resolution of half the wavelength. For the purpose of resolution improvement, a frequency multiplier circuit is added behind the detector so that a signal with n times the frequency of the signal from the detector is acquired. Thus the resolution of the demodulation becomes $\frac{\lambda_0}{2n}$. This method can achieve a good resolution with a large dynamic range (the dynamic range only limited by the capacity of the counter in the system), but the results merely provide the information of the relative FP cavity length change which only indicates the amount of change in the measurand. Calibration could be used each time after the instrumentation unit is turned on to set a reference point to the demodulation system. Then the absolute cavity length could be acquired for the following measurements. However this is not convenient for many applications. In addition, the direction of the cavity length change can not be determined through the demodulation

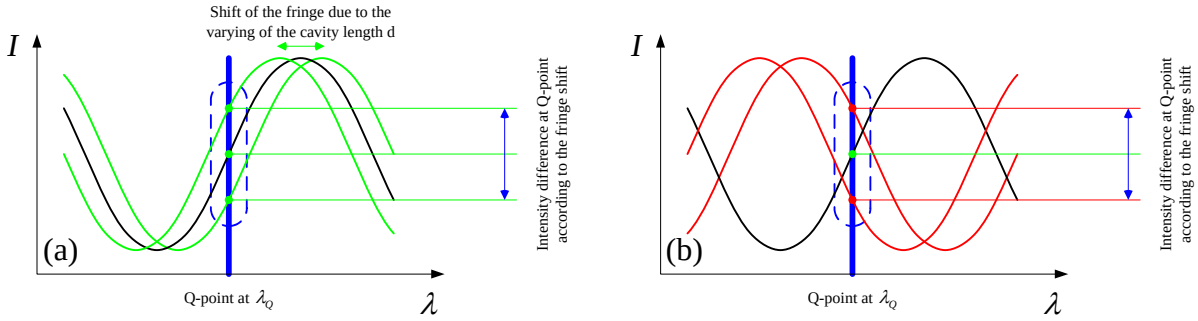

Figure 1.2: Principle of quadrature phase detection method

process. Additional information about the direction should be input to the system in order that correct results could be Obtained.

The principle of the quadrature phase detection method is shown in Fig.1.2(a). When this method is applied, the FP sensor is usually illuminated by a wide band light source. The fringe from a tunable filter is placed in front of the detector. The Q-point is located at the center of the linear region within one period of the fringe by tuning the center wavelength of filter λ_Q. The intensity of the light signal falling on the detector still has the same expression given in Eq.(1.1). By the linear approximation, Eq.(1.1) becomes:

$$I(d) \approx \pm \frac{4\pi I_m}{\lambda_Q} \Delta d + I_0, \tag{1.2}$$

where $\Delta d = d - d_0$, d_0 is the cavity length within the linear region where $\cos\left(\frac{4\pi d}{\lambda_Q} + \varphi_0\right) = 0$. It is obvious that the dynamic range of this method is limited to a small range determined by $-\left(\frac{1}{8} + \frac{\varphi_0}{4\pi}\right)\lambda_Q < d < \left(\frac{1}{8} - \frac{\varphi_0}{4\pi}\right)\lambda_Q$ and the slope of the linear region is $\frac{4\pi I_m}{\lambda_Q}$. Both the linear region and the slope are functions of the wavelength λ_Q. The measurand does not consider the dynamic range limitation and may cause the situation presented in Fig.1.2(b). At this time the intensity difference due to the cavity length varying caused by the fringe shift is the same value as the one in Fig.1.2(a). Under this circumstance ambiguity appears which could not be corrected within the system. To prevent the ambiguity from happening,

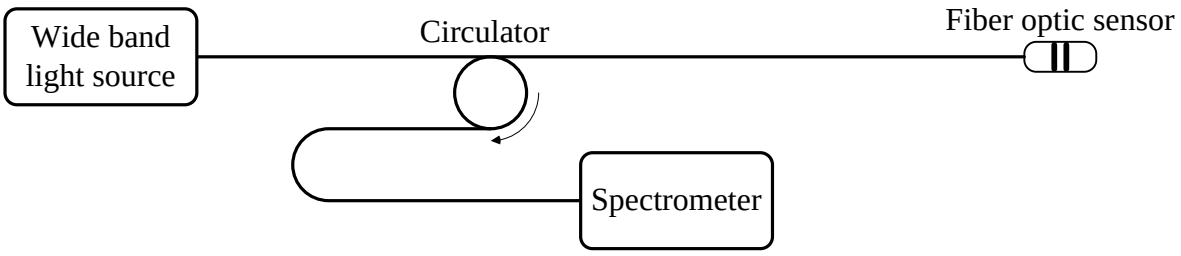

Figure 1.3: Block diagram of white light interferometry system

the sensitivity of the sensor needs to be reduced for the measurand with large dynamic range which on the other hand lowers the accuracy of the measurement. In addition, the approximation in Eq.(1.2) introduces distortion to the demodulation results. To reduce the distortion, the dynamic range should be limited to an even smaller region which further makes it difficult to solve the trade off between the accuracy and dynamic range. However the quadrature phase detection method is the only high speed demodulation method which could achieve up to several hundred *KHz* response before the development of the high speed fiber optic spectrometer (HSFOS). So it has been widely used in many applications where high speed demodulation is more important than large dynamic range and high accuracy.

The absolute demodulation method for fiber optic FP sensors is usually related to white light interferometry. In such a system, a wide band light source illuminates the sensor. One spectrometer is used to record the fringes from the sensor. For the ideal situation, the intensity is a function of both wavelength λ and the cavity length d, and can be expressed as:

$$I(d,\lambda) = I_m \cos\left(\frac{4\pi d}{\lambda} + \varphi_0\right) + I_0, \tag{1.3}$$

which is quite similar to Eq.(1.1). This result is derived based on two assumptions. First, the two reflection surfaces at both ends of the FP cavity are in perfect parallelism. Second, the light reflected from the two surfaces are plane waves. Then the absolute cavity length is

determined through tracing the position of one valley or peak in the sensor fringes:

$$d = \frac{\lambda_n}{2}\left(n - \frac{\varphi_0}{2\pi}\right) \tag{1.4}$$

or

$$d = \frac{\lambda_n}{4}\left(2n + 1 - \frac{\varphi_0}{\pi}\right), \tag{1.5}$$

where the λ_n is the wavelength of the valley or peak and the nonnegative integer n is the order number of the valley or peak which could be found through calibration before measurement or from other low accuracy results of d. The relative error of the peak tracing method is:

$$\left|\frac{\Delta d}{d}\right| = \left|\frac{1}{\lambda_n}\right| \Delta\lambda_n. \tag{1.6}$$

The absolute cavity length could also be obtained by measuring the wavelength of the two adjacent valleys or peaks, or one pair of adjacent valley and peak:

$$d = \frac{\lambda_n \lambda_k}{2(\lambda_n - \lambda_k)} \tag{1.7}$$

or

$$d = \frac{\lambda_n \lambda_k}{4(\lambda_n - \lambda_k)}, \tag{1.8}$$

where k is also a nonnegative integer which represents the order of the valley or peak; λ_n and λ_k are the wavelengths of the two adjacent valleys or peaks, or the valley-peak pair. The relative error for the method is:

$$\left|\frac{\Delta d}{d}\right| = \left|\frac{\sqrt{\lambda_n^4 + \lambda_k^4}}{(\lambda_n - \lambda_k)\lambda_n\lambda_k}\right| \Delta\lambda, \tag{1.9}$$

where $\Delta\lambda = \Delta\lambda_n = \Delta\lambda_k$. Due to the difference of the two wavelengths $\lambda_n - \lambda_k$ in the denominator of the coefficient $\left|\frac{\sqrt{\lambda_n^4+\lambda_k^4}}{(\lambda_n-\lambda_k)\lambda_n\lambda_k}\right|$ before $\Delta\lambda$ in Eq.(1.9), $\left|\frac{\sqrt{\lambda_n^4+\lambda_k^4}}{(\lambda_n-\lambda_k)\lambda_n\lambda_k}\right|$ is much larger than $\left|\frac{1}{\lambda_n}\right|$ in Eq.(1.6), especially when the FP cavity length is long which corresponds to small difference between λ_n and λ_k. So the two points interrogation method has larger errors than the valley/peak tracing method. In practice, the two methods are often combined

in which the two point interrogation method determines the rough cavity length of the FP sensor and further the order of one valley or peak in the fringe. Then the valley/peak tracing method provides the high accuracy cavity length values [4].

The value of φ_0 in both Eq.(1.4) and (1.5) has been found not to be a constant [5]. Moreover the results from Eq.(1.6) and (1.7) always have certain kind of errors. The reason behind the phenomena is the errors introduced by the assumption. The light out of a single mode fiber is no longer a plane wave. In addition, there is often a small angle between the two reflection surfaces which also contributes to the deflection of the results from the ideal ones. Some researchers did comprehensive investigations on this topic and one fitting method is made which could generate more accurate results than the above valley peak tracing methods. Owing to the absolute measurement nature, the white light interferometry has already been used as a high performance signal processing method for fiber optic sensors which provides both large dynamic range and high measurement accuracy. However, the speed is restricted by the low speed of the existing spectrometers or optical spectra analyzers (OSA).

For fiber optic FBG sensor signal processing, the structure of the signal demodulation system is the same as presented in Fig.1.3. The only difference is the data processing method. In a spectrum from FBG sensors, the reflection peak position is directly related to the measurand. Normally, through measuring the peak position with a spectrometer whose spectral resolution is high enough to resolve the peak, the measurand is determined. Existing spectrometers do have the capability to accurately measure the position of the FBG reflection peak. The only bottle neck of the system is also the speed.

In general, fiber optic sensors are widely used in industrial and medical applications. With the increasing applications, more demands on higher speed arise. Current signal demodulation systems could not achieve high speed, high accuracy and large dynamic range at the same time which limit the applications of those inherently high performance fiber optic sensors.

1.3 Scope of the dissertation

Although high performance sensors have been developed in the past decade. The old signal demodulation system with either high speed but small dynamic range and low accuracy or with large dynamic range and high accuracy but low speed could not meet the demand from many applications. The goal of this dissertation is to design and test the new HSFOS and the signal demodulation system based on it. The research work of the dissertation is focused on the following issues:

- Develop a novel operational principle and structure for the HSFOS.
- Conduct theoretical analysis of the proposed system
- Build a prototype and carry out preliminary experiments to prove the feasibility of the design and demonstrate the capability of the HSFOS

The remainder of the dissertation is organized as follows: Chapter 2 provides a brief review of optical spectrometers. In Chapter 3, the operational principle of the HSFOS is presented first. Then a mathematical model is derived and a few simulation results are given. Chapter 4 deals with the performance analysis of the HSFOS. The analysis is conducted comprehensively in four aspects including accuracy, resolution, speed and noise. In Chapter 5, the preliminary results from the prototype HSFOS are listed. The new spectrometer is configured for both FP and FBG sensors signal demodulation. Finally in Chapter 6, a summary of the dissertation and suggestions for future works are provided.

Chapter 2

A brief review of optical spectrometers

An optical spectrometer is an instrument which has long history and wide applications. It measures the light properties over certain region of electromagnetic spectrum. The independent variable during the measurement is the wavelength of the light or unit in direct proportion to the photon energy of the light, such as frequency, wavenumber or electron volts. Each of these units has a reciprocal relationship to the wavelength. The measurement results are usually the intensity of the light expressed as a function of the wavelength or frequency [6].

2.1 Different structures of spectrometers

From the perspective of operational principle, spectrometers could be grouped into two categories. One is based on monochromators or dispersive components; the other is based on wavelength dependent modulation devices. The simplified structures of both types are shown in Fig.2.1. For the first category, usually slits or masks with specially designed shape

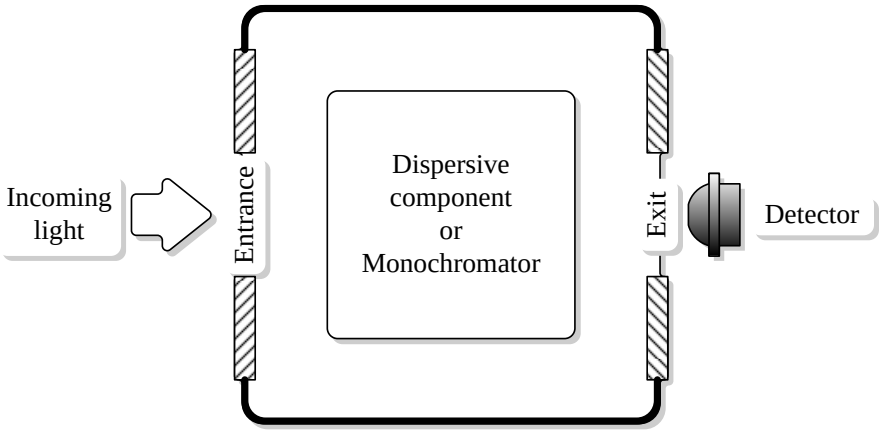

(a) Structure for dispersive component based spectrometer

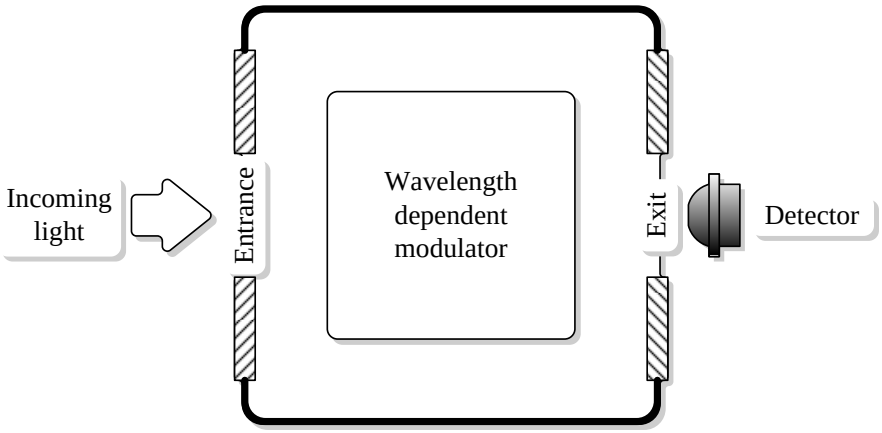

(b) Structure for wavelength dependent modulator based spectrometer

Figure 2.1: Simplified structures of optical spectrometers

or pattern is put at the entrance or exit or both places. If a dispersive component is used in the spectrometer, the incoming light is dispersed by that dispersive component and a spatially distributed pattern is generated at the exit. This pattern is the spectrum of the incoming light produced by the spectrometer or a group of coded signals which carry the information of the spectrum. For the former, by using a single detector to scan the pattern or by using an array detector to detect the pattern or a piece of film to record the pattern, the spectrum is acquired. For the latter, decoding is needed before or after the recording of the pattern in order to recover the spectrum. If a tunable monochromator is used, the output of the spectrometer is a narrow band light selected by the monochromator from the light that enters the spectrometer. A detector is placed at the exit of the spectrometer. By tuning the monochromator and at the same time recording the output signal of the detector, the spectrum of the incoming light is measured.

In the second category, a wavelength dependent modulator is put into the spectrometer. Usually it is an interferometer and the spectrometer is called a Fourier transform spectrometer. The type of the interferometer can be Michelson, Mach-Zehnder, or Fabry-Perot (FP). Incoming light from the entrance is first modulated by the interferometer to generate an interferogram. If the two beams which interfere with each other are parallel, by moving one mirror in the direction normal to the mirror, an interferogram is acquired point by point through one detector at the exit. If the two beams which interfere with each other are not parallel, a spatially distributed interferogram is generated at the exit. It can be scanned by a single detector point by point or recorded by an array detector which captures the whole pattern at one time. After the acquisition, computing the Fourier transform of the interferogram reveals the spectrum of the incoming light.

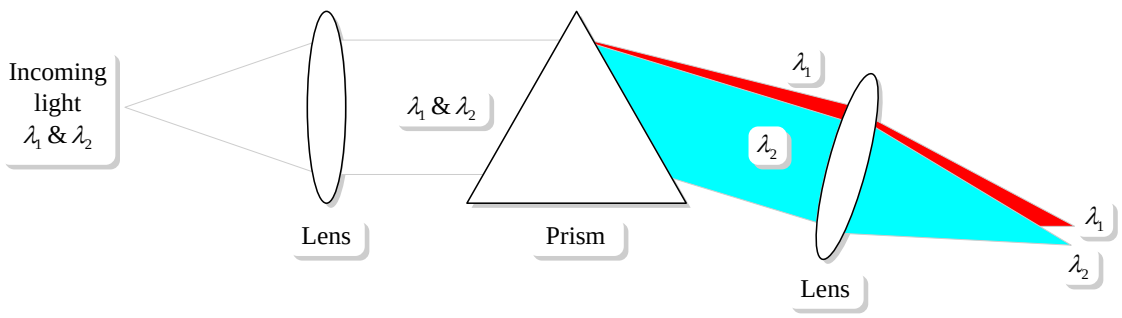

Figure 2.2: A prism as dispersing component [7]

2.2 Dispersive component based spectrometer

2.2.1 Spectrometer using prisms

The history of spectrometers using prisms as dispersive components can be traced back to the late seventeenth century when Newton realized that prisms have the capability to disperse visible light [7]. Until now, prism based spectrometers are still in use. When a prism is used as shown in Fig.2.2, the parallel light from the collimating lens reaches one of the surfaces of the prism with an angle. After the light goes through the prism, different wavelengths λ_1 and λ_2 are focused at different points by the second lens as shown in the figure.

The selection of material for making the prism is of great importance to this type of spectrometer. First, the material must be transparent to the light being analyzed otherwise no light inputs the detector thus no spectrum is generated. Second, the derivative of the refractive index n to the wavelength λ, $\frac{\mathrm{d}n}{\mathrm{d}\lambda}$, should be properly chosen, together with choices of the light incident angle, the size of the prism and the focal length of the lens behind the prism in order that the resolution requirement of the spectrometer can be fulfilled. For glass, the transparent wavelength can be as low as 400 nm; quartz, including both the crystalline and fused form, transmits visible and ultraviolet light and the transparent wavelength can be as low as 185 nm [7]. Both the glass and quartz prisms are transparent to the infrared and can

be applied in infrared spectrometers.

Prism based spectrometers have simple structure and low fabrication cost, but the tradeoff between resolution and the sensitivity limits their applications. The derivative of the refractive index, $\frac{dn}{d\lambda}$, increases rapidly when the wavelength λ approaches the material's absorption region in spectral domain. The transparent spectrum range of the material also limits applications of the prism. Moreover, the prism material in certain spectral ranges is hygroscopic and needs a moisture-free environment which causes inconvenience for applications [7]. Due to these reasons, they are replaced by grating based spectrometers.

2.2.2 Spectrometer using grating

In a grating based spectrometers, the component for generating the spatially dispersed light pattern is a grating. There are two types of gratings that can achieve the dispersion task, i.e. transmission type gratings and the reflection type gratings. Since the reflection type gratings introduce lower loss to the optical path of the spectrometers than the transmission type gratings and their operational spectrum range is less limited by material properties, they are the most common gratings used in spectrometers. In addition, the spectrometers in which transmission gratings are used often require a long optical path [7]. This enlarges the size of the spectrometers that is not preferred by some applications.

Rowland developed the theory for diffraction gratings around 1893 [7]. A reflection type grating is formed by many equally spaced parallel grooves. Their widths are comparable to the wavelength of the light to be dispersed. Fig.2.3 shows the cross section of a diffraction grating. In the figure, d is the distance between two adjacent grooves which is called the grating constant, θ is the blaze angle. By properly designing this angle, up to 90% of the light intensity can be concentrated to the selected diffraction order in the diffraction pattern. This property of the grating was first realized by Wood in 1910 [7]. It helps to largely improve the interferometer's sensitivity so that they can be applied in the situations where the incoming light intensity is very low. The planar shape is not the only shape for diffraction gratings.

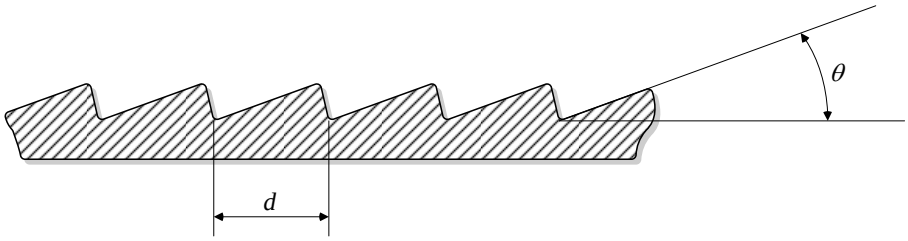

Figure 2.3: Cross section of a diffraction grating

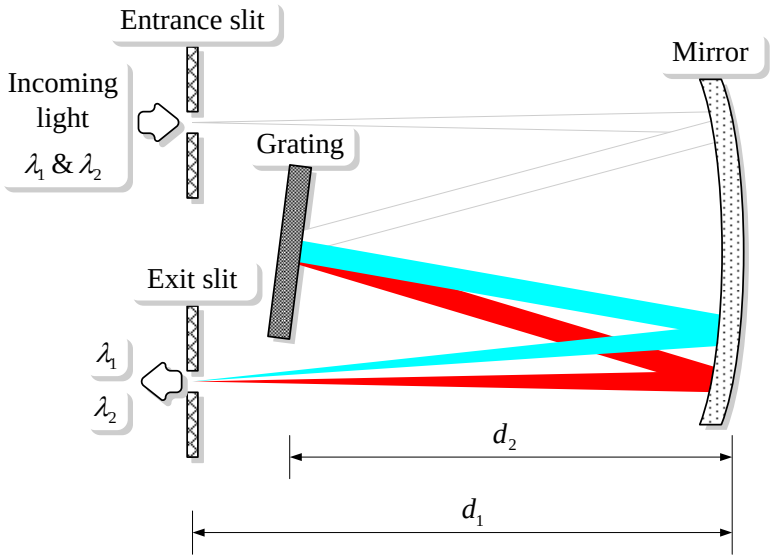

Figure 2.4: Structure of Ebert-Fastie type configuration [7]

Some researchers also use concave gratings in the spectrometer for the research in astronomy to improve the sensitivity of the spectrometer [16][17].

Two structures are usually used in grating based spectrometers. They are the Ebert-Fastie type and the Czerny-Turner type configuration which are shown by Fig.2.4 and Fig.2.5 respectively. Many spectrometers have been developed based on these two configurations since the 1950s [8]∼[15].

The Ebert-Fastie type configuration was first introduced by Ebert in 1889. In 1952, Fastie further improved it. As shown in Fig. 2.4, the entrance slit and exit slit are both placed at

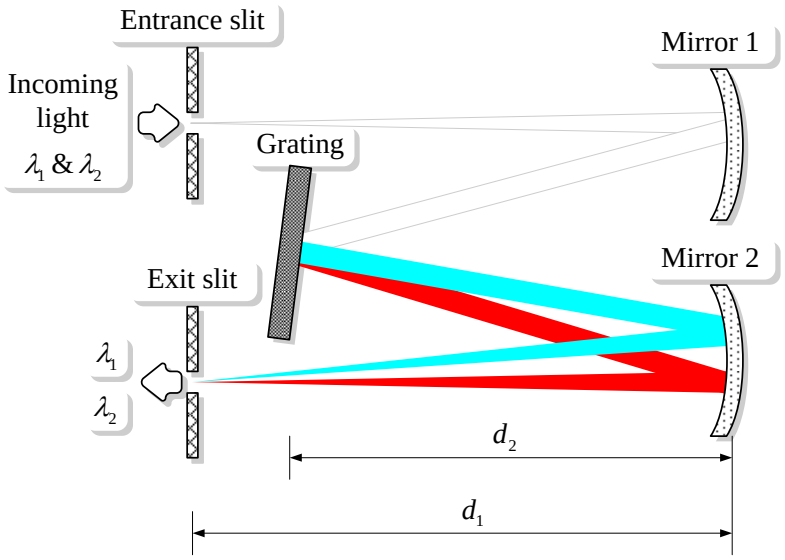

Figure 2.5: Structure of Czerny-Turner type configuration [7]

the position that has a distance, d_1, equals to the focal length of the concave mirror. The light from the light source with spectral components of different wavelengths goes through the entrance slit and reaches the concave mirror. Then the grating is illuminated by the parallel light beams from the concave mirror. At last, the concave mirror focuses the dispersed light beam from the grating to the exit slit for detection [7].

The Czerny-Turner type configuration could be seen as a variation of the Ebert-Fastie type. The structure was first described in 1930. As shown in Fig.2.5, the main difference between the Czerny-Turner type and the Ebert-Fastie type is that the single concave mirror in the latter is replaced by two separate mirrors in the first one. The two concave mirrors have the same focal length. The purpose of using two separate mirrors instead of one single mirror is to reduce optical aberrations so that the resolution of the spectrometer is limited only by grating imperfections [7].

The gratings used in the spectrometers are not restricted to those which are machined to special shape from raw materials. Sometimes researchers use the materials with inherent periodic structures, e.g. a crystal which has special crystal lattice, as grating. One example

is the spectrometer for the x-ray spectrum measurement, where a Bragg crystal is used as a grating to disperse the incoming x-ray radiation [18][19].

2.2.3 Spectrometer using interferometer

An interferometer could act as a dispersive component in a spectrometer [7][20]∼[22]. If a parallel beam of monochromatic light reaches an interferometer with incident angle θ, then an interference pattern similar to the diffraction pattern generated by grating is formed after the interferometer which consists of parallel lines. Whenever the condition $2 \cdot n \cdot d \cdot \cos\theta = m \cdot \lambda$ is met, one constructive interference line appears. In this equation, n is the refractive index of the material placed between the two mirrors of the interferometer, d is the physical distance between the two mirrors or their images, θ is the incident angle of the light beam to face of the mirror and m is the order of the interference lines in the pattern. If the wavelength range of the incoming light is narrower than the free spectral range of the interferometer, the pattern of each specific order forms the spectrum of the incoming light.

2.2.4 Resolution improvement

To improve the resolution of the prism and grating based spectrometers, a Littrow type configuration shown in Fig. 2.6 is often used by researchers [23][24]. This structure was originally utilized by Littrow in 1862 [7]. The idea is to allow the light to be dispersed to pass through the same dispersive component twice to obtain higher dispersion so that resolution is improved. As shown in Fig. 2.6, the incoming light from entrance slit first reaches the paraboloid mirror (mirror 1). Here the purpose of using paraboloid is to reduce optical aberrations. Then the beam is converted to a parallel beam and reflected onto the prism. The light from the prism goes to the planar mirror (mirror 2) and is reflected back to the prism. Once more the beam passes through the prism. At last the beam reflected by the paraboloid mirror and the planar mirror (mirror 3) and falls on the detector. Other structures

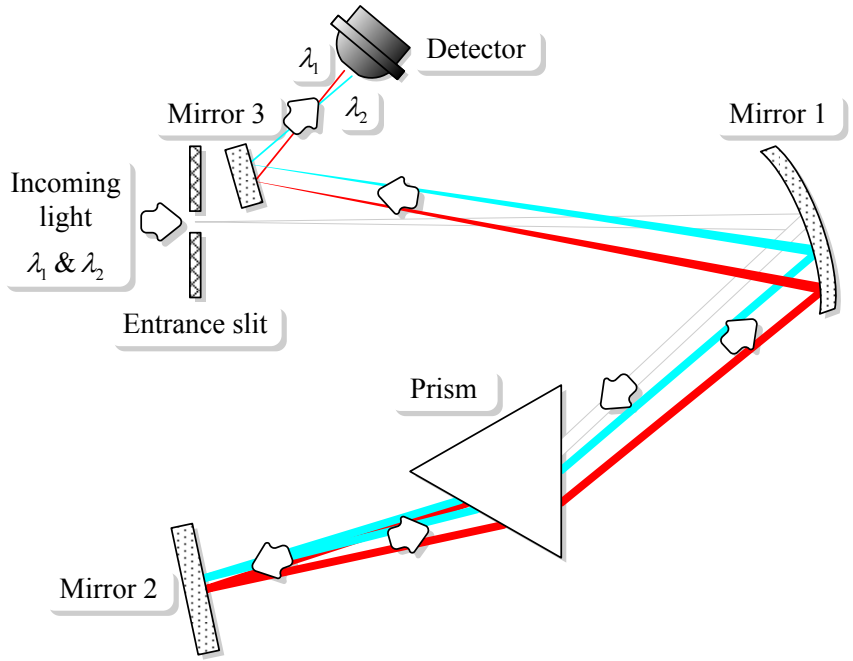

Figure 2.6: Littrow type configuration [7]

with the multiple pass ideas similar to the Littrow configuration have also been developed [25][26]. For grating based spectrometer (including transmission type and reflection type gratings), there is another method that can be used to improve the resolution, i.e. choosing the high order portion of diffraction pattern as the output of the spectrometer. Properly designed slits at entrance and exit are also important for getting high resolution [27].

2.2.5 Speed improvement

To improve the speed of the dispersion component based spectrometer, high speed detectors are needed. The fast developing semiconductor industry now is able to provide photodetectors with response speed up to several GHz (This is for single detectors. The speed of array detectors can hardly reach that level). The second step is reducing the time used during detection of the dispersed pattern or the spectrum. For those spectrometers which use a single detector, the problem is how to increase the scan speed i.e. how to increase the

relative movement speed between the dispersed pattern and the detector. Many structures have been proposed since the 1960s. The most popular method is using high speed rotating mirrors or vibration mirrors to projects the dispersed light to the detector [9]∼[12][28]∼[31]. This structure is able to achieve an acquisition speed up to 20,000 frames of spectra per second.

Before array detectors such as CCD and photo diode array appeared, there was a special component used in spectrometer: the television camera tube. This component gets the image that falls on the target in the front of the tube by scanning the target using an electron beam controlled by a high voltage saw-tooth signal. The spectrometer which equipped with this tube is called electronic scanning spectrometer [32][33]. Typically, this kind of spectrometers can reach a acquisition speed up to 1000∼10000 frames per second.

As soon as array detectors had been developed, they were applied in spectrometers to improve the speed. Most of them were made of silicon due to the semiconductor process and were suitable for the applications with wavelength shorter than 1100 nm. Their speeds are still being improved. Currently the typical acquisition speed of the spectrometer using an array detector is 100∼1000 frames per second.

2.2.6 Efficiency improvement and multiplex capability

In a real spectrometer, the detector generates noise whether a signal falls on it or not. This eventually limits the spectrometer's ability to detect weak incoming light. For those spectrometers which use dispersive components, the design of the slit at the entrance and exit determines the efficiency of the instrument. A wider slit lets more light energy reach the detector. However, this lowers the spectral resolution. To solve the tradeoff between efficiency and resolution, spectrometers with masks at the entrance or exit or both have been developed.

The Golay spectrometer was developed by Golay in the early 1950s [34]. The Grill spec-

trometer was developed by Girard, Stewart and Mertz in the early 1960s [34]. The former uses complementary mask groups at the entrance and exit and two detectors are placed behind the exit masks. The common mode signal from the two detectors is generated by those spectral components in the dispersive pattern not directly facing the exit masks. The differential mode signal is generated by the spectral components in the dispersive pattern directly facing the exit masks. By calculating the difference between the signals from the two detectors, the intensity of certain spectral components can be acquired.

The Grill spectrometer has special designed masks whose autocorrelation function have a peak at the origin and small value elsewhere [34]. Although all the wavelengths in the incoming light are modulated by the same mask, the differences in the spatial shifts between different wavelengths induced by the dispersion element results in only one wavelength being detected at each position after the autocorrelation. Several spectrometers based on this structure were developed since the 1960s due to its high efficiency [35][36].

In both the Golay spectrometer and the Grill spectrometer, each time only one wavelength is modulated. They only increase the energy falling on the detector, but do not have the ability of multiplexing. Mask spectrometers which have multiplexing capability are the Mock interferometer spectrometer and the Hadamard spectrometer. The Mock interferometer spectrometer built by Mertz during the 1960s using two circular disks called Ronchi grids each of which consists of alternate open and closed slits. These disks rotate synchronously around different centers. The slits on the two disks remain parallel during the rotation. Then the light with different wavelengths is chopped at different frequencies. Analysis of the signal spectrum from the detector provides the spectrum of the light [34].

It was realized independently by Ibbett *et al*, Decker and Harwit that the optical spectrometers based on Hadamard optical coding have the advantage of multiplexing [37]. The Hadamard spectrometer modulates the light of different wavelengths with different codes made from the rows of Hadamard matrix or S matrix. Through computing the scalar product of the group of modulated results with the corresponding matrices optically or by using

a computer, the spectrum of the light is acquired. The idea is similar to the code division multiple access (CDMA) technology applied in modern communication system which uses orthogonal codes to realize multiplexing. Because of their high efficiency and multiplexing advantage, Hadamard spectrometers are well developed and widely used since the 1960s [38]∼[44].

2.3 Monochromator based spectrometer

A monochromator has the capability to select part of narrow band radiation from a wide band incoming light signal. Spectrometers based on monochromators utilize this property to measure the light intensity of different wavelengths. By tuning the transmission or reflection band of the monochromator and at the same time recording the results, a spectrum of the incoming light is acquired. The wavelength selectivity of the monochromator determines the resolution of the spectrometer.

In this type of spectrometer, the monochromator can be either a tunable one or a group of fixed filters. If a single detector is used, the filter group or the detector is mounted on a moving part to achieve the scan in order to detect the spectrum. If an array detector is used, both the filter and the array detector are fixed. By means of electronic scan proceeded in the array detector, the spectrum is detected. Spectrometers with a monochromator array are usually for those applications where the spectral resolution is not of great importance but simple structure and low cost are preferred. For high resolution applications, an interferometer can be the monochromator.

The type of interferometer can be Michelson, Mach-Zehnder, Sagnac or Fabry-Perot. However considering the simplicity of the structure, compact size and rapid scan capability, researchers often use FP interferometer. The transmission wavelength is tuned by means of changing the optical path length (cavity length) between the two mirrors of the FP interferometer. Two methods are available for varying that optical path length. One is mechanically

changing the space between the two mirrors [45]; the other is changing the refractive index between the two mirrors [46][47]. The former is realized by thermal tuning or by attaching one or both mirrors on piezoceramics and applying different voltages to them. The latter is achieved based on the Kerr effect by putting one piece of electro-optic material between the two mirrors and applying different voltage on it.

2.4 Fourier transform spectrometer

The interferogram from an interferometer records the superimposed light signals of all the different wavelengths projected on a detector. The spectrum of the light is able to be recovered from the Fourier transform of the interferogram. This gives the interferometry the multiplex advantage when it is used in spectroscopy. P. B. Fellgett first pointed this out in his Ph.D. dissertation in 1952 [48]. The boom of Fourier transform spectrometers however arrived in the late 1960s, after two important achievements. One is the development of more powerful digital electronic computers; the other is the algorithm for fast computation of Fourier transform which is usually called FFT algorithm introduced by Cooley and Tukey. The type of interferometer used in Fourier transform spectrometer can be Michelson, Mach-Zehnder, Sagnac or FP.

In their early stages of development, Fourier transform spectrometers were built mostly based on Michelson interferometer to generate a time varying interferogram. In the spectrometers, the two mirrors which form the interferometer or their images are kept parallel which is critical to the accuracy of the results. The position of one mirror is fixed. The other mirror is mechanically moved along the normal direction of the mirror to achieve the scan thus a time-varying interferogram is produced. A single detector is used to record the interferogram produced during the scan [49]$\sim$[54]. In reality, these Fourier transform spectrometers can hardly keep the two mirrors or their images parallel during a long distance scan. As a result, only a limited scan range for the mirror can be achieved which ultimately put a limitation

on the spectrum measurement range and spectral resolution of the spectrometers. Some researchers use a cat's eye reflector to improve the performance [55]. But this method can not completely solve the problem. Mechanical scanning also has other problems. First, the structure is complex which increases the cost but may not improve the performance; second, the scan speed is low which reduces the speed of the spectrometer; third, the size of the spectrometer is large which is not preferred in certain applications. As a solution to the problems, some researchers developed so called static Fourier transform spectrometers.

There are two different ways to build a static Fourier transform spectrometer. The first one still uses an interferometer with two mirrors, but the two mirrors or their images are no longer parallel. Instead, one mirror is tilted such that there is a small angle between the two mirrors or their images. Then a spatial distributed interferogram is generated [56][57]. The second one uses birefringence components, e.g. the Wollaston prism, to generate the spatial distributed interferogram [58]∼[61]. Then an array detector records the spatial distributed interferogram. Here the use of an array detector, e.g. a CCD, also helps to improve the speed of the spectrometer. Interferometer and birefringence components are not the only device used to get interferogram in Fourier transform spectrometer. Diffraction gratings can also be put into Fourier transform spectrometer to achieve the same function [62].

2.5 Other types of spectrometers

2.5.1 Time-resolved spectrometer

Time-resolved spectrometer is a new type of spectrometers which have been developed since the 1980s [63]. It is capable of recording a varying spectrum over a time interval span from several minutes to a few picoseconds or even several femtoseconds. The spectrometers are widely used to study transient phenomena such as plasma, chemical and biochemical reactions. For those applications that require only low time resolution down to 1 ms, spectrome-

ters with traditional structures such as rapid scanning or ultra-rapid scanning spectrometers are used. When higher spectral resolution is needed while the time resolution requirement kept the same, the rapid scanning or ultra-rapid scanning Fourier transform spectrometers are chosen.

When higher time resolution is required, the step-scanning spectrometer or the stroboscopic sampling spectrometer, each of which is a variation of the Fourier transform spectrometer, are used. In each scan, these spectrometers only sample part of the interferogram. The signal sampling during the scans are arranged in a certain order. For the step-scanning spectrometer, the movement of the scanning mirror is divided into equal spaced steps. At each step, the scanning mirror stops for short interval, during which the event is repeated and the interference optical signal is converted to electric signal and sampled by high speed analog-to-digital converter (ADC) [63][64]. For the stroboscopic sampling spectrometer, the mirror continuously scans, at the same time high speed ADC samples the signals. The data sampling procedure is synchronized with the scan. There is a different time delay between the beginning of the repeatable event and the starting of scan each time when a new scan starts. A whole interferogram is recovered by reorganizing the data after multiple repeated scans. The time resolution of both spectrometers highly depend on the speed of the ADC [63]. To further improve the time resolution, the pulsed-asynchronous sampling spectrometer can be used. In this kind of spectrometers, the sampling is no longer synchronized to the scan of the mirror. Instead, the interferogram for each time point within the time span of the event is continuously sampled until the whole interferogram is digitized by the ADC controlled by the synchronization signal from the interferometer. Then the interferogram is replaced by that of the next time point. This largely reduces the speed requirement to the ADC. However, the acquisition time of one interferogram is much longer than step-scanning and stroboscopic sampling spectrometers. For this reason, a multi-channel structure was developed for this kind of spectrometer to improve the acquisition speed [63][65].

If a structure other than the Fourier transform spectrometer is used, for example a structure with a dispersive component, an optoelectronic streak camera can be put into the

time-resolved spectrometer to reach a time resolution similar to the asynchronous sampling spectrometer. The basic principle of the optoelectronic streak camera is described as follows. The photons of the light with certain wavelength in the instantaneous spectrum are first converted to electrons at the target in the front of a cathode ray tube (CRT). Then these electrons pass through a time dependent electric field normally formed by high voltage saw-tooth signal, which deflects these electrons in the CRT to form a spatial distributed pattern on a phosphor screen located on the other side of the CRT. The electrons corresponding to the photons arriving at the streak camera at different time point have different position in that pattern. At last the pattern corresponding to the time varying signal is recorded by an array detector. Thus by the photon-to-electron conversion and the time varying deflection of the electrons, fast time varying light signal of certain wavelength is measured [66].

There is an assumption when operating the time-resolved spectrometer with structures other than the traditional rapid scanning or ultra-rapid scanning spectrometers, that is the spectrum or the event to be analyzed is able to be repeated and each time the result is identical. Although those spectrometers have very high time resolution, they do not have the capabilities to catch and analyze the events that only happen once or the events can not be well controlled and repeated e.g. the fast varying fringes from a FP pressure sensor which is put into a jet engine to measure the dynamic pressure. In short, they are not suitable for non-repeatable phenomena analysis.

2.5.2 Heterodyne spectrometer

The heterodyne spectrometer is a powerful tool to analyze and characterize the spectrum with extremely narrow spectral width [67]∼[70]. The structure and the operational principle of a heterodyne spectrometer is similar to a electronic spectra analyzer. One tunable light source usually a tunable laser is used as a local oscillator. The incoming light meets the light from the local oscillator at the detector. Due to the nature of the existing electronic photodetector, only the intensity of the light signal is converted to an electric signal which

is intrinsically a nonlinear procedure. Thus the two light signals are mixed or beaten at the detector. Results from the narrow bandwidth of the electronic devices compared to the light frequency, only the low frequency part in the beat signal, i.e. the signal with frequency differences between the two light signal is received and amplified for further analysis. At last, through the spectrum analysis of the electric signal by using electronic spectra analyzer or by using FFT, the detailed structure of the light spectrum is recovered. The spectral resolution of the spectrometer could be several orders higher than all other spectrometers. However it is not suitable for fiber optic sensor signal processing because the measurement range is narrow and the speed is low.

2.5.3 Correlation spectrometer

The correlation spectrometer is based on calculating the correlation between the spectrum to be analyzed and the reference one already known. It is good for those applications when species or chemical material need to be quickly identified. There are two types of correlation spectrometers. One uses a target material contained in a cell to make the reference spectrum; the other uses a diffraction grating to generate the reference spectrum. To improve the flexibility, some new technologies have been introduced to the correlation spectrometer. The most useful one is the variable-element grating in which by apply different voltage to different elements in the grating, the properties of the grating can be modified such that different diffraction pattern is generated which represents the spectrum of different target material [71].

2.6 Summary

As one kind of optical instruments used for light properties measurement, spectrometers can be roughly divided into two types from the perspective of structure. One is based on a dispersive element to form a spatially distributed pattern which represents the spectrum of the light, or a monochromator which is used to filter the incoming light according to wavelength; the other is Fourier transform spectrometer which acquires spectrum by calculating the Fourier transform of the interferogram. To improve the performance of the first type in the aspects of spectral resolution, efficiency and multiplexing capability, different methods have been developed. To improve the speed, different spectrum detection mechanisms have been used. Fourier transform spectrometers have high spectral resolution and can achieve high time resolution when certain sampling sequences are used. However their speed is usually low. The most promising way of speed improvement for both type spectrometers is using an array detector, e.g. a CCD, to record the spectrum or the interferogram. But, due to the semiconductor fabrication process and the availability of the semiconductor materials, the operational wavelengths of these devices are usually shorter than 1100 nm. Thus normally the spectrometers with an array detector are not suitable for high speed signal demodulation of the fiber optic sensor operated at 1310 nm and 1550 nm.

Chapter 3

Operation Principle

In this chapter, the structure of a new high speed fiber optic spectrometer (HSFOS) is presented first. The operation principle of the spectrometer and the functions of different components in the spectrometer are described in detail. Then a mathematical model for the proposed spectrometer is developed. In addition, an approximate model is given for reducing the computation task in numerical simulations.

3.1 Structure of the HSFOS

As mentioned in the previous chapter, during the past decades, several spectrometry technologies have been developed and different types of spectrometers have been built for various applications. For those transient spectra which can be produced from repeatable experiments, time-resolved spectrometers can achieve an extremely high time resolution down to femtoseconds. The experiment are repeated thousands of times or even more. Each time only a small part of the information of one single frame spectrum is acquired. Moreover, each of the experiment lasts a long time, e.g. several milliseconds. Thus to complete the acquisition of one frame spectrum takes a very long time. For the circumstances such as fiber

optic sensor signal demodulation, their performance can hardly meet the ever-increasing requirements. Spectrometers equipped with an array detector may be suitable for high speed applications at wavelengths shorter than 1100 nm. However they can hardly record the signal from fiber optic sensors operated at 1310 nm or 1550 nm. New high speed spectrometers for fiber sensor signal processing with are pursued.

With the results from comprehensive research on optical fiber dispersion, high speed optical modulators and detectors, and ultra high speed analog to digital converters (ADC), building a new type high speed spectrometer using time-domain dispersion instead of spatial dispersion becomes feasible. Some researchers have experimentally demonstrated the possibility of recording optical spectrum using dispersive fiber [72][73]. Others have used the same method to measure the absorption spectra of chemicals with better results by using supercontinuum which might be the best high power wide band light source currently available [74]∼[78]. In addition, high speed optical modulators and detectors with speeds of 40 Gb/s are now commercially available. Ultra high speed ADCs with speeds of greater than 100 GS/s are reported [79]∼[83] and 60 GS/s high speed ADCs are commercially available. The HSFOS developed for fiber optic sensor signal processing combines high speed time domain sampling of light signal based on high speed modulation, time domain light signal dispersion, high speed light signal detection and high speed data acquisition. Theoretically, it can achieve an acquisition speed of at least 1 million frames of spectra per second.

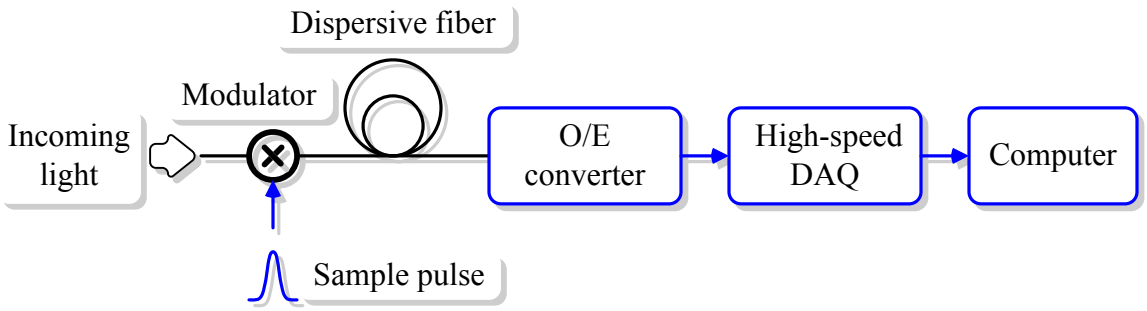

Figure 3.1: Operation principle of the HSFOS [84]

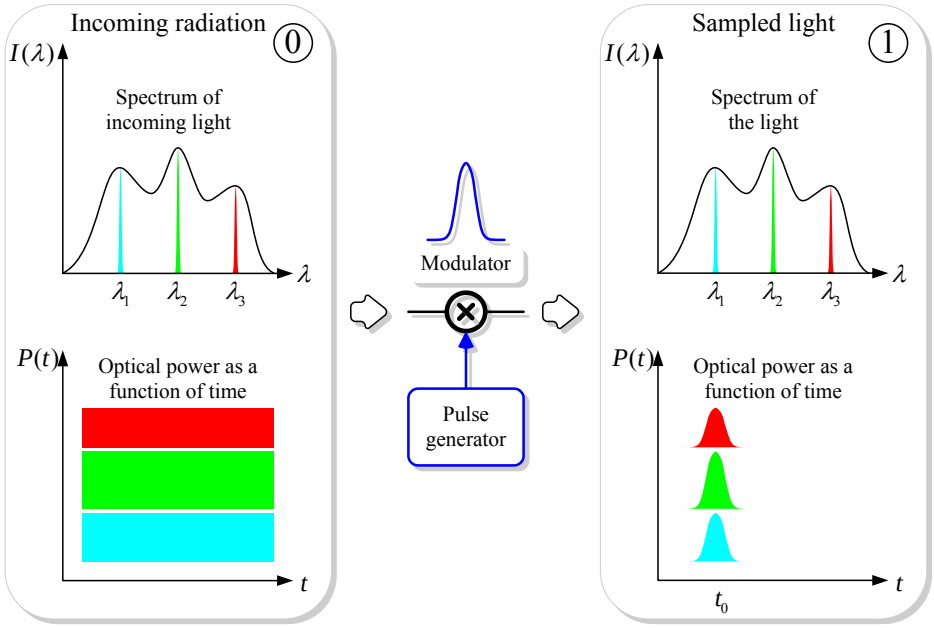

Figure 3.2: The first operation step: time domain sample

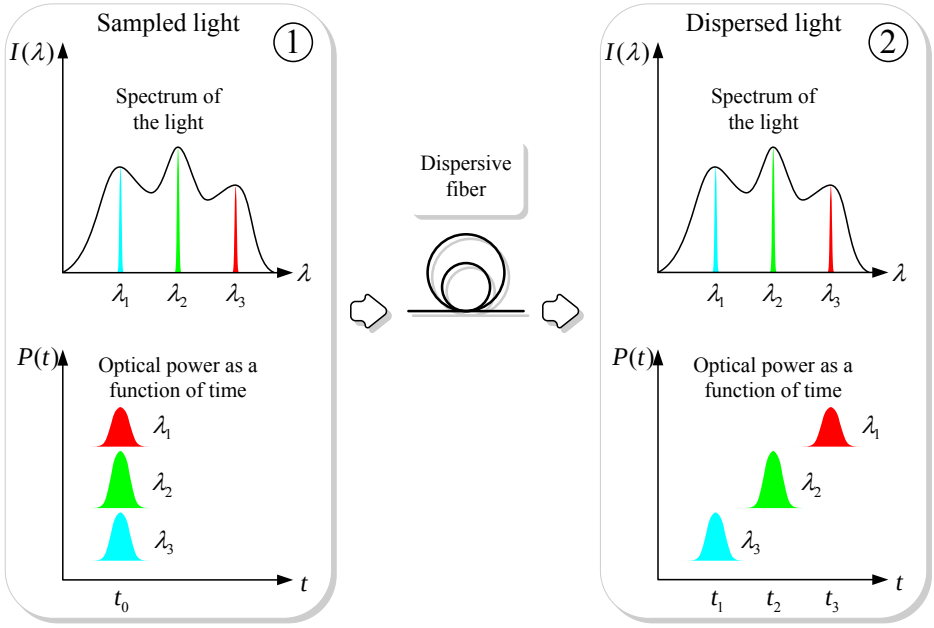

Figure 3.3: The second operation step: time domain dispersion

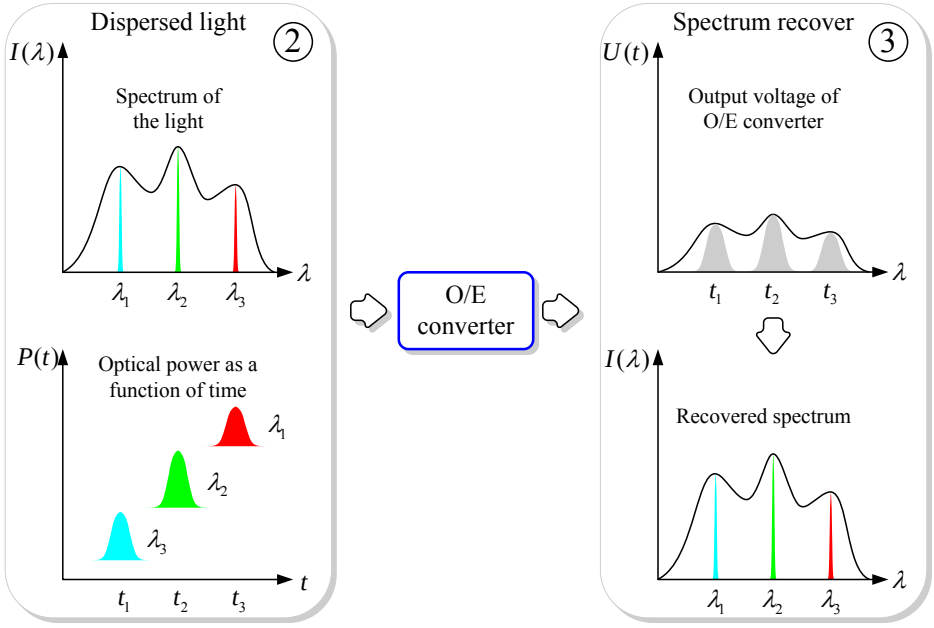

Figure 3.4: The third operation step: spectrum recover

The operation principle of the HSFOS is illustrated in Fig.3.1. In all the block diagrams presented in this dissertation, for clarity, the optical paths are drawn using black lines and the electric paths are drawn using blue lines. The incoming light to the HSFOS is first modulated by a series of narrow pulses with a fixed pulse width and repetition rate from the pulse generator through the modulator to form the time domain samples of the light, each of which will finally form one frame of spectrum. These samples go through a span of dispersive fiber to achieve the time domain dispersion. Each dispersed light pulse signal has a profile representing the spectrum of the incoming light. Then the optical to electric (O/E) converter turns the dispersed light signals into electric signals and the high speed data acquisition device (DAQ) samples and digitizes the signals and sends the data to a computer for spectrum construction [84]. The details of the three operation steps are presented in Fig.3.2∼Fig.3.4 respectively. The dispersive fiber in Fig.3.3 is assumed to have a positive dispersion. For clarity, in all the three figures, the light signals at each operation step are shown in two types of plots. One is for presenting the spectrum of the signals; the other is

for providing the time domain information of the signals.

3.2 Mathematical model

Ignoring the fiber nonlinearity, the whole process presented in the previous section can be mathematically modeled as follows. The field $E(0,t)$ and the intensity $I(0,t)$ of the incoming light are described as

$$E(0,t) = A(t)\exp\left(j\omega_0 t\right) \tag{3.1}$$

and

$$I(0,t) = |E(0,t)|^2 = E(0,t)E^*(0,t), \tag{3.2}$$

where $A(t)$ is the complex amplitude which determines the spectral profile of the incoming light, and " $*$ " denotes complex conjugate. The complex amplitude, $A(t)$, is assumed to be a stationary random process. So we have the temporal autocorrelation function of $A(t)$ as

$$R(t-t') = \langle A(t)A^*(t')\rangle\,, \tag{3.3}$$

in which the angle brackets "$\langle\rangle$" indicate the ensemble average. The spectrum of the field is

$$F(0,\omega) = \frac{1}{2\pi}\int_{-\infty}^{+\infty} E(0,t)\exp(-j\omega t)\mathrm{d}t, \tag{3.4}$$

and the spectral density function $P(0,\omega)$ is then expressed as

$$\begin{aligned} P(0,\omega) &= F(0,\omega)F^*(0,\omega) \\ &= \frac{1}{(2\pi)^2}\int_{-\infty}^{+\infty}\int_{-\infty}^{+\infty} E(0,t)E^*(0,t')\exp[-j\omega(t-t')]\mathrm{d}t\mathrm{d}t'. \end{aligned} \tag{3.5}$$

Substititing Eq.(3.1) into Eq.(3.5), using Eq.(3.3) and defining $u = t - t'$, the power density function now becomes

$$P(0,\omega) = \frac{1}{2\pi}\int_{-\infty}^{+\infty} R(u)\exp(-j(\omega-\omega_0)u)\mathrm{d}u. \tag{3.6}$$

For intensity modulators, define $M_0(t)$ as the intensity modulation signal, and $m_0(t)$ is the square root of the modulation signal; for amplitude modulators, define $m_0(t)$ as the

modulation signal. The modulated electric field of the incoming light $E_m(0,t)$ and the spectrum of the field $F_m(0,\omega)$ are

$$E_m(0,t) = m_0(t)E(0,t) \tag{3.7}$$

and

$$\begin{aligned} F_m(0,\omega) &= \frac{1}{2\pi}\int_{-\infty}^{+\infty} m_0(t)E(0,t)\exp(-j\omega t)\mathrm{d}t \\ &= \int_{-\infty}^{+\infty} F(0,\omega')f_0(\omega-\omega')\mathrm{d}\omega' \end{aligned} \tag{3.8}$$

respectively, with spectrum of the modulation signal

$$f_0(\omega) = \frac{1}{2\pi}\int_{-\infty}^{+\infty} m_0(t)\exp(-j\omega t)\mathrm{d}t. \tag{3.9}$$

The electric field after propagating through a distance L in the dispersive fiber with propagation constant β can be expressed as

$$E_m(L,t) = \int_{-\infty}^{+\infty} F_m(L,\omega)\exp(j\omega t)\mathrm{d}\omega = \int_{-\infty}^{+\infty} F_m(0,\omega)\exp(j(\omega t-\beta L))\mathrm{d}\omega. \tag{3.10}$$

Therefore, the profile of the dispersed light signal is

$$\begin{aligned} s(t) &= \langle E_m(L,t)E_m^*(L,t)\rangle \\ &= \int_{-\infty}^{+\infty}\int_{-\infty}^{+\infty}\langle F_m(0,\omega)F_m^*(0,\omega')\rangle \\ &\quad \times\exp\left\{j\left[(\omega-\omega')t-(\beta-\beta')L\right]\right\}\mathrm{d}\omega\mathrm{d}\omega' \end{aligned} \tag{3.11}$$

which is expressed in terms of the autocorrelation function of the dispersed electric field. Following Marcuse's previous work [85]$\sim$[87], and using the relation

$$\langle F(0,\omega)F^*(0,\omega')\rangle = P(0,\omega)\delta(\omega-\omega'), \tag{3.12}$$

together with Eq.(3.8), the autocorrelation function term in Eq.(3.11) can be rewritten in the following form

$$\langle F_m(0,\omega)F_m^*(0,\omega')\rangle = \int_{-\infty}^{+\infty} P(0,\omega'')f_0(\omega-\omega'')f_0^*(\omega'-\omega'')\mathrm{d}\omega''. \tag{3.13}$$

Thus the profile of the light signal, $s(t)$, after propagation through the dispersive fiber is given by

$$s(t) = \int_{-\infty}^{+\infty} P(0,\omega') \left| \int_{-\infty}^{+\infty} f_0(\omega-\omega') \exp\left\{ j\left[(\omega-\omega')t - (\beta-\beta')L \right] \right\} \mathrm{d}\omega \right|^2 \mathrm{d}\omega'. \tag{3.14}$$

The propagation constant $\beta(\omega)$ in the above equation could be expanded in a Taylor series about the circular frequency ω'

$$\beta(\omega) = \sum_{m=0}^{\infty} \frac{\beta_m(\omega')}{m!} (\omega-\omega')^m \tag{3.15}$$

where

$$\beta_m = \frac{\mathrm{d}^m \beta}{\mathrm{d}\omega^m} \quad (m = 0, 1, 2, 3, \ldots). \tag{3.16}$$

In the previous work, the propagation constant is usually expanded around the circular frequency ω_0 which is the center circular frequency of the chromatic light pulse, which means the whole chromatic pulse is treated as one package. This results in a complicated mathematical expression for the light signal profile $s(t)$ and makes the numerical simulation more difficult under the conditions when the spectrum does not have a Gaussian profile, or the pulse is not a Gaussian pulse. The advantages of using the center circular frequency of each monochromatic light pulse, ω', instead of ω_0 is that, as shown later in this section, a clearer picture of how the chromatic light pulse dispersion in the dispersive fiber can be formed and a more concise expression can be acquired that facilitates both the analytic and numerical analysis. From Eq.(3.15) we have

$$\beta(\omega) - \beta(\omega') = (\omega-\omega')\beta_1(\omega') + \gamma(\omega,\omega') \tag{3.17}$$

where

$$\gamma(\omega,\omega') = \sum_{m=2}^{\infty} \frac{\beta_m(\omega')}{m!} (\omega-\omega')^m. \tag{3.18}$$

In Eq.(3.17), $\beta_1(\omega')$ is related to the group velocity of the monochromatic light at ω'. Substituting Eq.(3.17) into Eq.(3.14), we obtain

$$\begin{aligned} s(t) \;=\; & \int_{-\infty}^{+\infty} P(0,\omega') \left| \int_{-\infty}^{+\infty} f_0(\omega-\omega') \right. \\ & \left. \times \exp\left\{ j\left[(\omega-\omega')\left(t - \beta_1(\omega')L\right) - \gamma(\omega,\omega')L \right] \right\} \mathrm{d}\omega \right|^2 \mathrm{d}\omega'. \end{aligned} \tag{3.19}$$

Let $\omega'' = \omega - \omega'$, then

$$\gamma(\omega, \omega') = \Gamma(\omega'', \omega') = \sum_{m=2}^{\infty} \frac{\beta_m(\omega')}{m!} \omega''^m. \tag{3.20}$$

Define

$$f(L, \omega'', \omega') = f_0(\omega'') \exp(-j\Gamma(\omega'', \omega')L), \tag{3.21}$$

$$t_d(\omega') = \beta_1(\omega')L. \tag{3.22}$$

Eq.(3.19) now becomes

$$s(t) = \int_{-\infty}^{+\infty} P(0, \omega') \left| \int_{-\infty}^{+\infty} f(L, \omega'', \omega') \exp\left\{ j\omega'' \left(t - t_d(\omega') \right) \right\} \mathrm{d}\omega'' \right|^2 \mathrm{d}\omega'. \tag{3.23}$$

It should be noticed that $f(L, \omega'', \omega')$ in Eq.(3.23) is the spectrum of a monochromatic light modulated by pulse signal $m_0(t)$ and then dispersed by the dispersive fiber. The term t_d in Eq.(3.23) is the group delay of this broadened light pulse and is a function of circular frequency ω' which is the center circular frequency of the light pulse. With the following relations

$$\omega'(t_d) = t_d^{-1}(\omega'), \tag{3.24}$$

$$\mathrm{d}\omega' = \frac{\mathrm{d}t_d}{\dot{t}_d(\omega')} = \frac{\mathrm{d}t_d}{\beta_2(\omega')L}, \tag{3.25}$$

where $t_d^{-1}(\omega')$ represents the inverse function of the function $t_d(\omega')$ and the dot over t_d in Eq.(3.25) represents derivative. Defining

$$m(L, t, t_d) = \int_{-\infty}^{+\infty} f_t(L, \omega'', t_d) \exp\left\{ j\omega'' \left(t - t_d \right) \right\} \mathrm{d}\omega'', \tag{3.26}$$

$$M(L, t, t_d) = \left| m(L, t, t_d) \right|^2, \tag{3.27}$$

where $f_t(L, \omega'', t_d) = f(L, \omega'', \omega')$, Eq.(14) becomes

$$s(t) = \int_{-\infty}^{+\infty} \frac{P_t(0, t_d)}{\beta_{2t}(t_d)L} M(L, t, t_d) \mathrm{d}t_d \tag{3.28}$$

with $\beta_{2t}(t_d) = \beta_2(\omega')$, and $P_t(0, t_d) = P(0, \omega')$. Setting

$$P_n(0, t_d) = \frac{P_t(0, t_d)}{\beta_{2t}(t_d)L} = \frac{P(0, \omega')}{\beta_2(\omega')L}, \tag{3.29}$$

Eq.(3.28) could be rewritten as

$$s(t) = \int_{-\infty}^{+\infty} P_n(0, t_d) M(L, t, t_d) \mathrm{d}t_d. \tag{3.30}$$

Till now, no truncation for the Taylor's series of the propagation constant has been made which is another difference between the new model and the results from the previous work. This improves the accuracy of the model. In the past work, only the terms with an order not higher than 3 or 4 in the Taylor's series were kept. In the above equation, $s(t)$ is given as an output corresponding to the input $P_n(0, t_d)$ from a linear time variant (LTV) system whose impulse response is described by $M(L, t, t_d)$. The input signal $P_n(0, t_d)$ is directly related to the light spectrum to be measured through Eq.(3.29). The function $M(L, t, t_d)$, which represents the shape of the monochromatic light pulse broadened by the dispersive fiber and is a function of t_d, shows that at different time points t_d or equivalently at different circular frequencies or wavelengths, the broadening of the monochromatic light pulse could be different. Moreover the $\Gamma(\omega'', \omega')$ term defined in Eq.(3.20) determines the broadening of the pulses according to the circular frequency ω'. The group delay for each monochromatic light pulse t_d defined in Eq.(3.22) is also related to the circular frequency ω'. Thus the output of the spectrometer $s(t)$ could be treated as the superposition of all the frequency-dependent broadened and delayed monochromatic light pulses whose wavelength before modulation is in the spectral range that the spectrometer handles. Under ideal conditions, the spectrometer has unlimited spectral range then the output becomes the superposition of all the frequency-dependent broadened and delayed monochromatic light pulses centered within the spectral width of the chromatic incoming light.

If all the $\beta_m(\omega')$ terms in Eq.(3.18) are substituted with $\beta_m(\omega_0)$ where ω_0 is the center circular frequency of the chromatic light pulse, that is using the shape of the broadened monochromatic light pulse centered at circular frequency ω_0 to approximate the shapes of all broadened monochromatic pulses centered at different frequencies, Eqs.(3.20), (3.21), (3.26) and (3.27) become

$$\Gamma_{\omega_0}(\omega'') = \sum_{m=2}^{\infty} \frac{\beta_m(\omega_0)}{m!} \omega''^m, \tag{3.31}$$

$$f'(L,\omega'') = f_0(\omega'')\exp(-j\Gamma_{\omega_0}(\omega'')L), \tag{3.32}$$

$$m'(L,t-t_d) = \int_{-\infty}^{+\infty} f'(L,\omega'')\exp(j\omega''(t-t_d))\mathrm{d}\omega'', \tag{3.33}$$

and

$$M'(L,t-t_d) = |m'(L,t-t_d)|^2 \tag{3.34}$$

respectively, and Eq.(3.30) thus becomes

$$s'(t) = \int_{-\infty}^{+\infty} P_n(0,t_d)M'(L,t-t_d)\mathrm{d}t_d, \tag{3.35}$$

which is a convolution of $P_n(0,t_d)$ and $M'(L,t)$, i.e.

$$s'(t) = P_n(0,t) * M'(L,t). \tag{3.36}$$

Now the system described in Eq.(3.36) is a linear time invariant (LTI) system and $M'(L,t)$ is the impulse response of the system. This approximation provides a simpler way to explain the operation principle of the spectrometer. Further, this model largely reduces the amount of computation task when the numerical simulation for spectrum and modulation with complex shape or profile is required.

Since for a specific dispersive fiber, time t and wavelength λ are related by

$$t = \beta_1(\frac{2\pi c}{\lambda})L, \tag{3.37}$$

the profile of the dispersed chromatic light pulse $s(t)$ in Eq.(3.30) and $s'(t)$ in Eq.(3.36) can also be expressed as functions of wavelength

$$s_\lambda(\lambda) = \int_{-\infty}^{+\infty} P_n(0,t_d)M_\lambda(L,\lambda,t_d)\mathrm{d}t_d, \tag{3.38}$$

$$s'_\lambda(\lambda) = P_{n\lambda}(0,\lambda) * M'_\lambda(L,\lambda), \tag{3.39}$$

where $M_\lambda(L,\lambda,t_d) = M(L,t,t_d)$, $M'_\lambda(L,\lambda) = M'(L,t)$, and $P_{n\lambda}(0,\lambda) = P_n(0,t)$.

The output $s_\lambda(\lambda)$ in Eq.(3.38) is the spectral density function of the incoming light acquired by the spectrometer. Thus by acquiring the output $s(t)$, the spectrum can be determined.

In the remainder of this section, a few numerical simulation results based on the accurate model are presented. In these simulations, the dispersion property of the fiber is similar to standard SMF-28 single mode fiber and the highest order of propagation constant derivative β_m is set to 3. The results are acquired by using two types of pulses with different shapes, including the Gaussian and rectangular shape, as the modulation pulses. In Fig.3.5(a) and (b), the shapes of the original and dispersed pulses are plotted. In Fig.3.5(c) the fiber dispersion property in the wavelength range from 1260 nm to 1660 nm is shown. Both the Gaussian and rectangular modulation pulses have a pulse width of 0.1 ns measured at the $\frac{1}{e}$ intensity position. Fig.3.6 illustrates the results when a Gaussian pulse is used. In Fig.3.6(a) and (b), the light spectrum to be measured $P_\lambda(0, \lambda)$ is a calculated FP cavity fringe resulted from a cavity length of 73 μm. In Fig.3.6(c) and (d), the light spectrum to be measured consists of two Gaussian spectra. One has a spectral width of 3 nm centered at 1536 nm; the other has a spectral width of 6 nm centered at 1560 nm. In Fig.3.6(e) and (f), the spectrum to be measured has two spectral lines that are located at 1536 nm and 1560 nm respectively. Fig.3.7 shows the corresponding results when rectangular modulation pulse is used. The three spectra of the incoming light are the same as used in previous simulations.

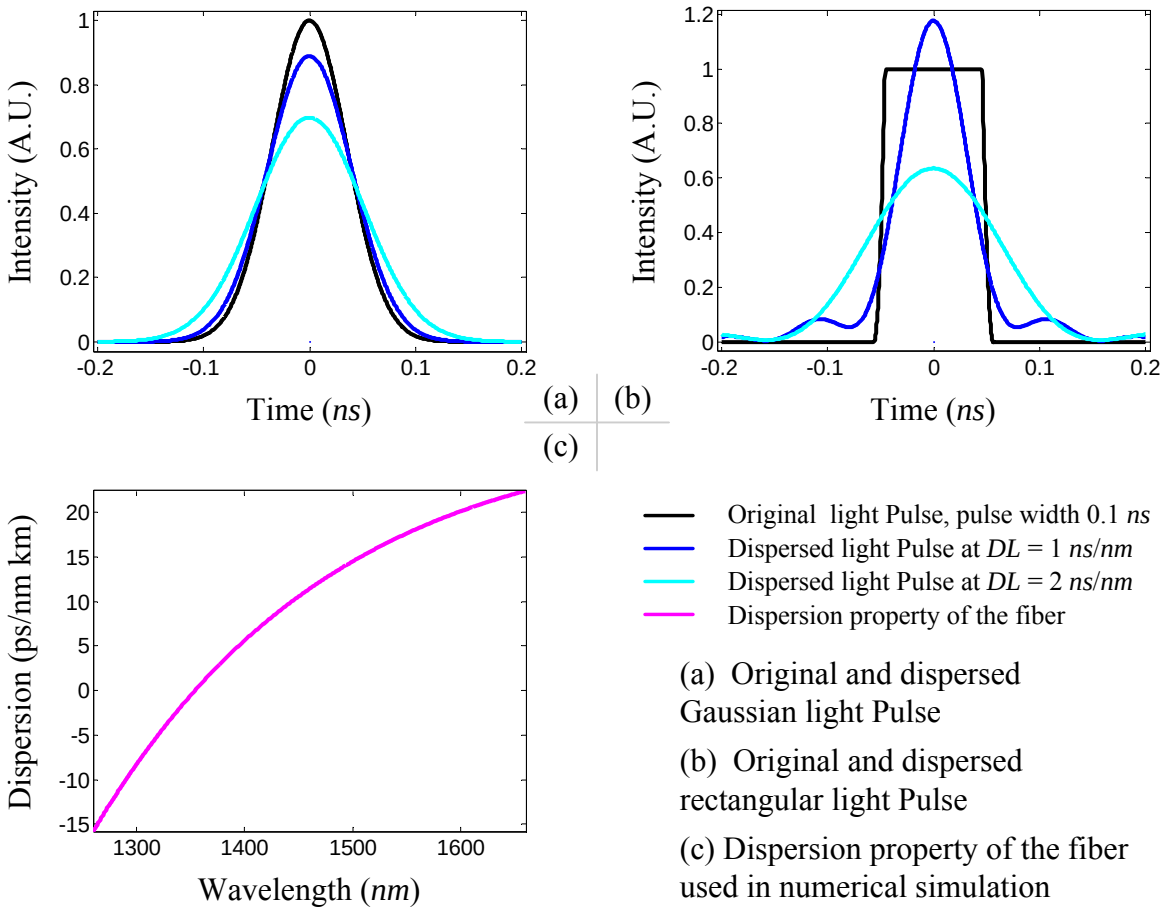

Figure 3.5: Modulation pulse shape and dispersion property of the fiber

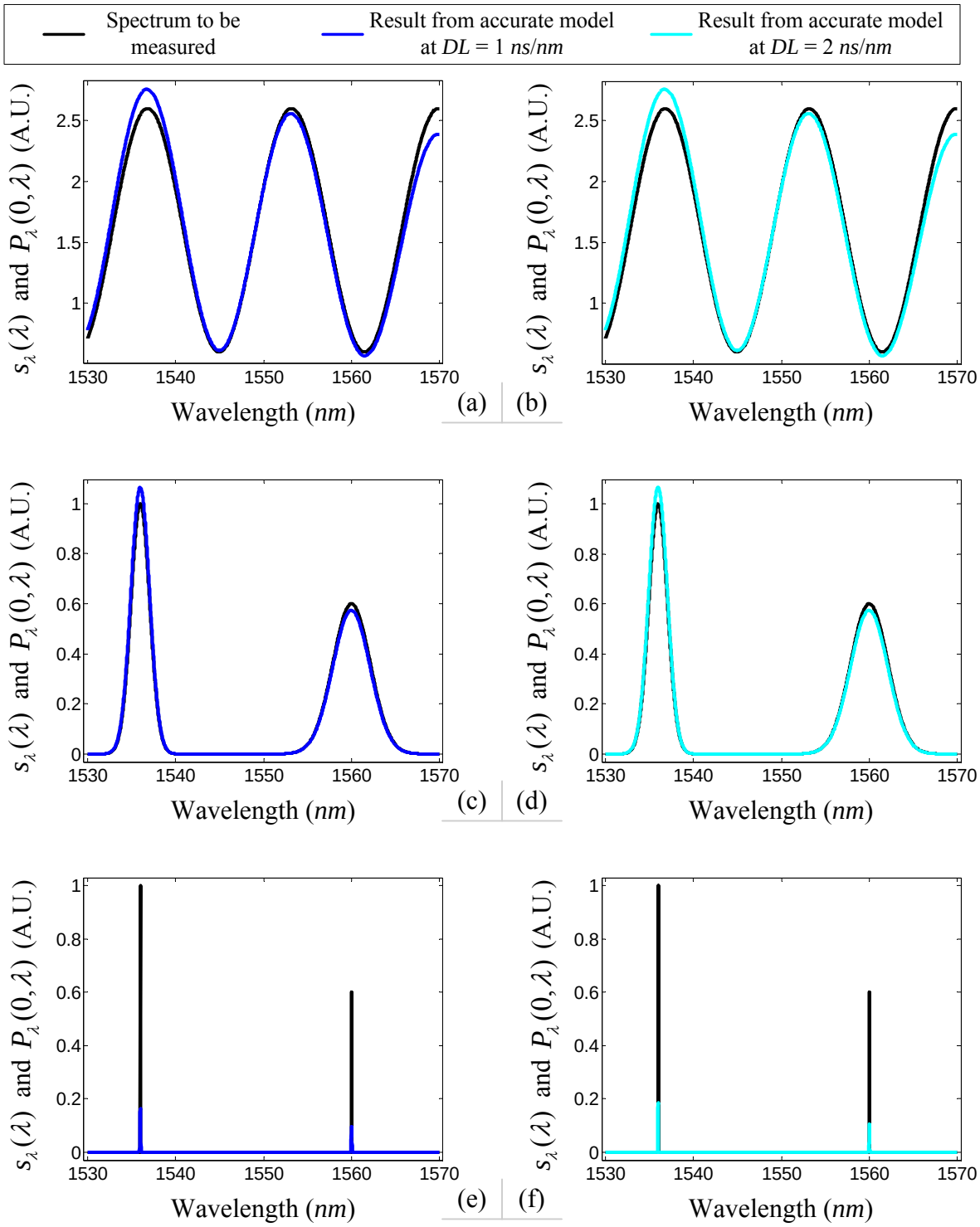

Figure 3.6: Simulation results using a Gaussian pulse

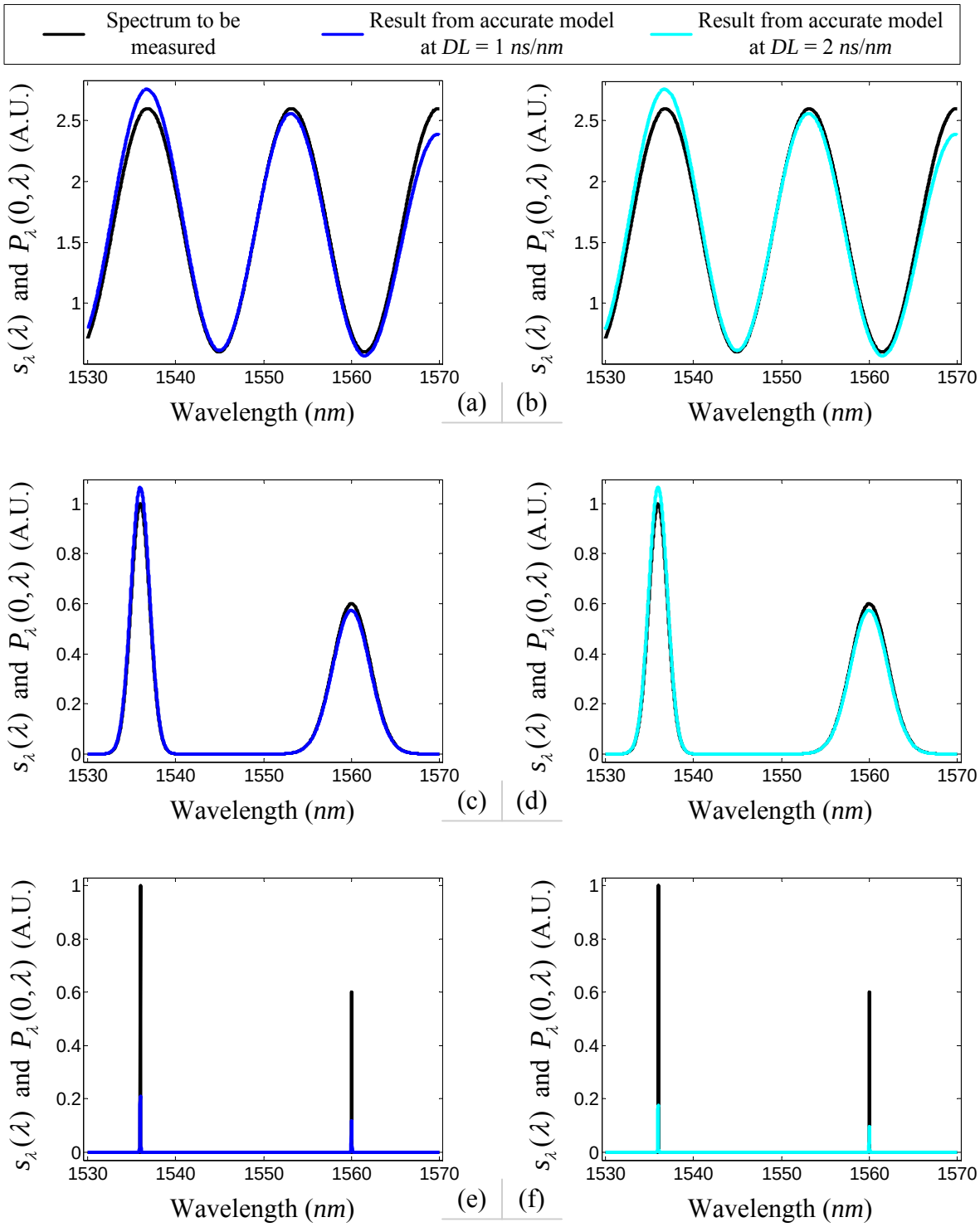

Figure 3.7: Simulation results using a rectangular pulse

3.3 Summary

In this chapter, the operation principle of the HSFOS is presented and an accurate mathematical model is developed. Under two assumptions, i.e. ignoring fiber nonlinearity and assuming that the complex amplitude of the light field is a stationary random process, it precisely describes the relationship between the optical spectrum of the incoming light and the profile of the dispersed time-domain signal. In the derivation, the propagation constant is expanded at the center circular frequency of each monochromatic light pulse and no truncation is made for the Taylor's series of the propagation constant. These are the two major differences from the previous work by Marcuse. This model and the conclusions derived from the analysis help to develop a clear picture of both the operation principle of the HSFOS and the profile evolution of the chromatic light pulse in dispersive fiber. Further, it provides an easier and more accurate way to achieve numerical simulation when the incoming light has a complex spectrum shape other than Gaussian type and the pulse has a shape different from Gaussian. The output of the spectrometer can be treated as the superposition of all the frequency-dependent broadened and delayed monochromatic light pulses whose wavelength before pulse modulation is in the spectral range that the spectrometer handles. The spectrum of the incoming light can be recovered through experimentally acquiring the output of the O/E converter which is in proportion to the profile of the dispersed light signal $s(t)$. In addition to the accurate model, an approximate model is also developed which provides an even simpler way to understand the underlying principle of the proposed spectrometer and reduces the computation task when numerical simulations need to be conducted. At the end of the chapter, a few simulation results based on the accurate model are presented. These examples demonstrate the capabilities of the developed model.

Chapter 4

Performance Analysis

This chapter presents the performance analysis for the HSFOS. The analysis is conducted in four different aspects. They are accuracy, resolution, speed and noise. The accuracy analysis and most of the resolution analysis are carried out through numerical simulation. In the simulations, three fibers with arbitrarily selected dispersion properties are used. For all the fibers, the derivatives of the propagation constant β with orders higher than 3 are ignored. The value of the group velocity dispersion (GVD), the second order dispersion β_3, the dispersion parameter D and the dispersion slope S at 1550 nm are listed in Table 4.1. D and S are defined by:

$$D = -\frac{2\pi c}{\lambda^2}\beta_2 \tag{4.1}$$

and

$$S = \frac{\mathrm{d}D}{\mathrm{d}\lambda} \tag{4.2}$$

respectively. The first fiber has very large β_3; the second fiber has a dispersion property similar to standard single mode fiber; the third fiber has constant GVD. The pulses used in the simulations are Gaussian pulses and rectangular pulses with pulse widths from 0.03 ns to 10 ns measured at $1/e$ intensity point. The reason for choosing these two pulses is that Gaussian pulses are the most common pulses used in theoretical analysis whereas the rectangular pulses have a pulse shape similar to the pulses from the pulse generator used in

Table 4.1: Fiber dispersion properties used in simulation

Fiber index No.	β_2 $(ps^2/rad \cdot Km)$	β_3 $(ps^3/rad^2 \cdot Km)$	D $(ps/nm \cdot Km)$	S $(ps/nm^2 \cdot Km)$
1	-595	25.5	466	15.1
2	-22.5	0.128	17.6	0.0559
3	-12.8	0	10.0	0.0133

our experiment. Using Gaussian pulses often leads to a simple analytical result which will be helpful to understand the underlying principles of the phenomena. Choosing rectangular pulses will connect the theoretical analysis with results from our experiments. Moreover, comparing the simulation results using both types of pulses will result in a more comprehensive understanding of the operational principles of the spectrometer and the relationship between the important parameters of the spectrometer such as the initial light pulse width, the spectral resolution and the speed. Further, comparing the results from different pulse types can reveal the effects of pulse shapes on the performances. To facilitate the analysis in the simulations, a calculated FP interferometric sensor spectrum with cavity length of 73 μm (shown in Fig.4.1(a)) and a calculated Gaussian spectrum with spectral width of 10 nm centered at 1550 (shown in Fig.4.1(b)) are used as the spectra to be measured.

Before starting the analysis, one important point should be made clear: the definition of the pulse width. There are two types of pulse widths often used in scientific research works. One is the full width at half maximum (FWHM) of the pulse, T_{FWHM}; the other is measured at the $1/e$ maximum of the pulse, $2T_0$. Fig.4.2 illustrates the shapes of the modulation pulses and the corresponding light pulse and different pulse width definitions for Gaussian and rectangular pulse. In the figure, T_{A0} is the FWHM width of the modulation pulse width. For Gaussian light pulse the two can be related by:

$$T_{FWHM} = 2\sqrt{\ln(2)}T_0. \tag{4.3}$$

For a rectangular modulation pulse and its corresponding light pulse, the relation between

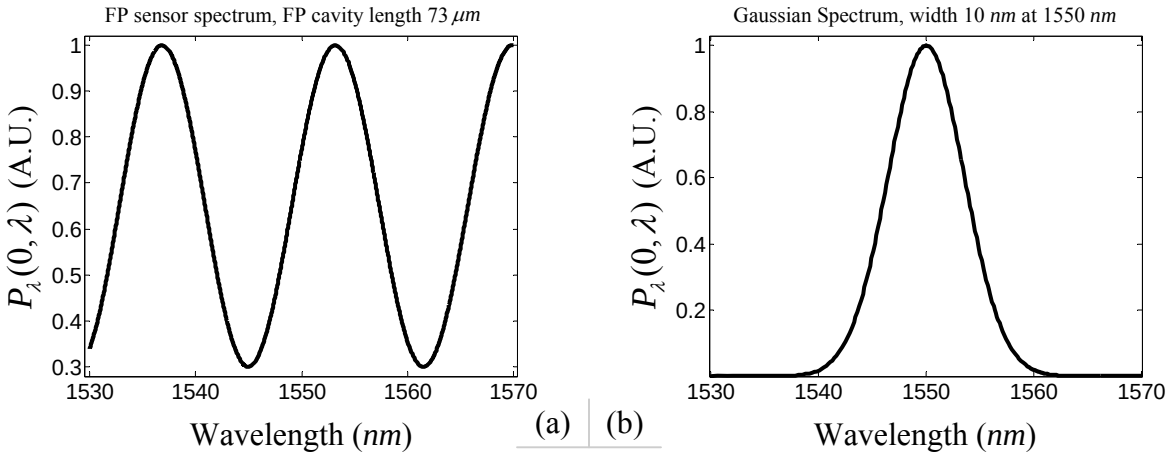

Figure 4.1: Calculated spectra used in performance analysis

T_{A0}, T_0 and T_{FWHM} could be expressed as:

$$T_{FWHM} = T_{A0}\left(1 + (\frac{1}{2} - \sqrt{\frac{1}{e}})(C_L + C_R)\right), \tag{4.4}$$

$$T_0 = \frac{T_{A0}\left(1 + (\frac{1}{2} - \sqrt{\frac{1}{e}})(C_L + C_R)\right)}{2}, \tag{4.5}$$

$$T_{FWHM} = \frac{2T_0\left(1 + (\frac{1}{2} - \sqrt{\frac{1}{2}})(C_L + C_R)\right)}{\left(1 + (\frac{1}{2} - \sqrt{\frac{1}{e}})(C_L + C_R)\right)}, \tag{4.6}$$

where $C_L = \frac{T_1}{T_L}$, $C_R = \frac{T_2}{T_R}$, and $T_{A0} = 2T_L = 2T_R$.

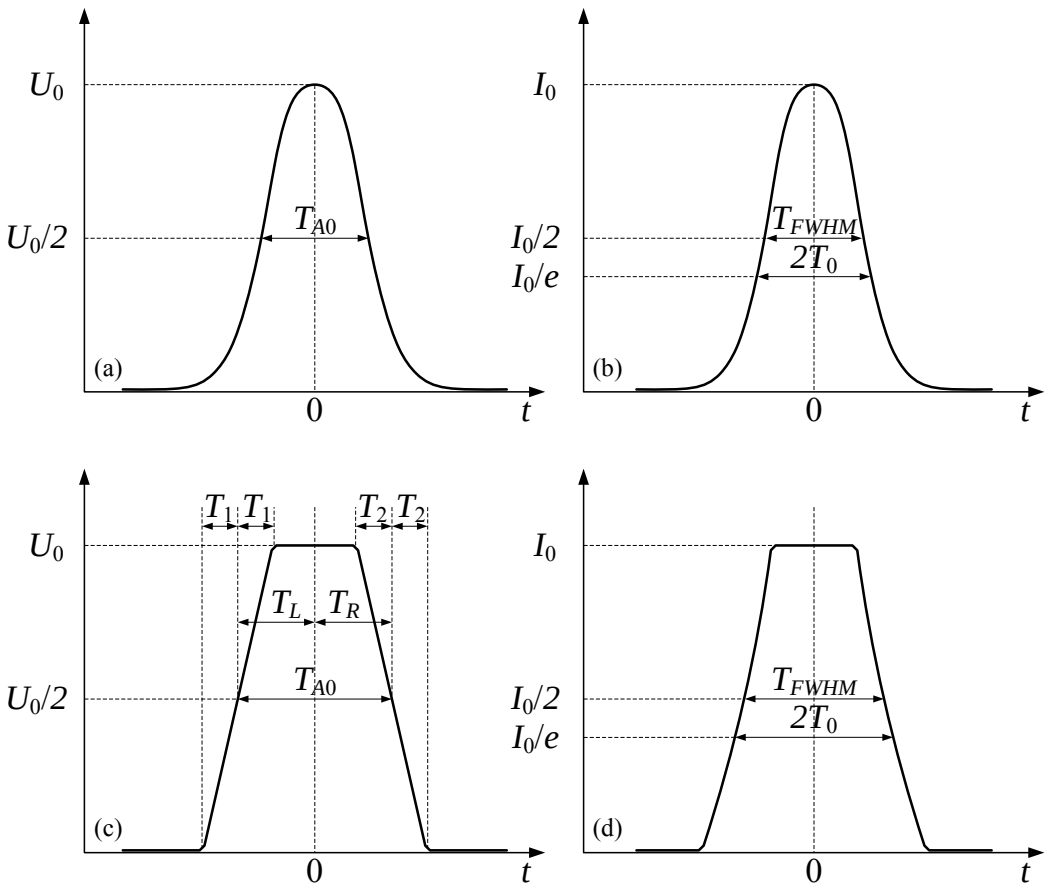

Figure 4.2: Different definition of pulse width

4.1 Accuracy

In the following analysis, two types of errors are investigated. The first one is the inherent error. This error is caused by the operating principle of the spectrometer itself and it determines the accuracy of the spectrometer. The second one is the model error. This error is generated during the approximation from the accurate model described by Eq.(3.30) to the approximate model presented in Eq.(3.36) and it affects the accuracy of the analysis based on the approximate model.

4.1.1 Inherent error

The inherent error Δ_1 is defined as the difference between the normalized result from the spectrometer expressed in Eq.(3.38) and the true spectral density function $P_\lambda(0,\lambda)$:

$$\Delta_1 = \left(\int_{-\infty}^{+\infty} P_n(0,t_d) M_\lambda(L,\lambda,t_d) \mathrm{d}t_d \right)_{normalized} - P_\lambda(0,\lambda) \tag{4.7}$$

where $P_\lambda(0,\lambda) = P(0,\omega)$.

Two reasons cause this error. The first one is from the frequency dependent modulation of spectrum $P_0(0,\omega')$ by $(\beta_2(\omega')L)^{-1}$ expressed in Eq.(3.29). This can be explained as the non-uniform distribution of the pulses resulting from the nonlinearity of $\beta_1(\omega')$. As discussed in the mathematical model, the output of the spectrometer $s(t)$ or $s_\lambda(\lambda)$ could be described as the superposition of all the non-uniformly broadened and delayed monochromatic light pulses whose corresponding wavelengths before the pulse modulation are in the spectrometer's spectral range it handles. The location of each dispersed monochromatic light pulse in the time domain is determined by its group delay $\beta_1(\omega')L$. Therefore $s(t)$ or $s_\lambda(\lambda)$ has a relatively larger value where the density of the pulses is higher. In Fig.4.3 the simulated outputs $s_\lambda(\lambda)$ with three fibers for an incoming light with a flat spectrum which has a constant spectral density function are presented. The figure indicates that even for a flat spectrum, the output of the spectrometer may not be constant at different time or wavelength points. The shape

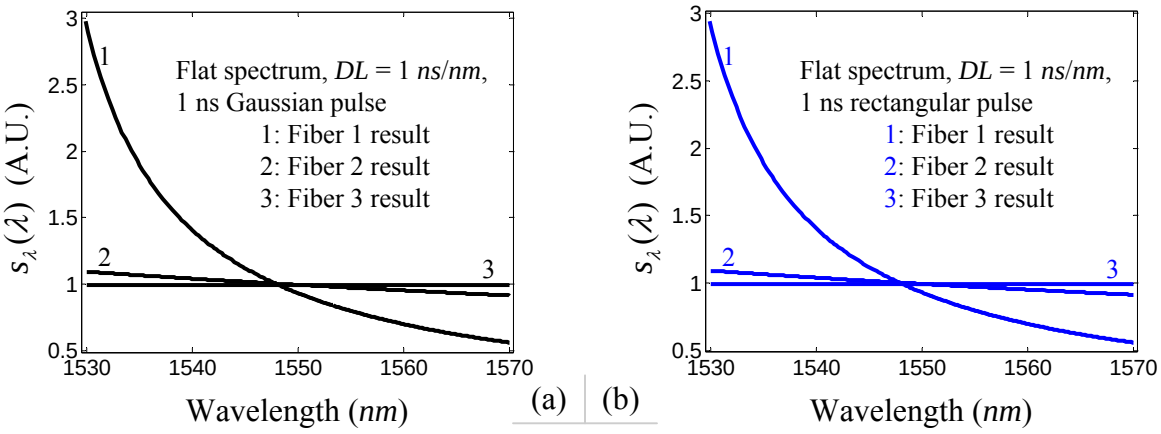

Figure 4.3: Spectrometer output $s_\lambda(\lambda)$ corresponding to a spectrum with constant spectral density

of the curve is mainly affected by the dispersion property of the fiber. This part of the error in Δ_1 caused by this reason can be partially corrected through amplitude normalization. The correction will have better results where the higher order dispersion parameters are smaller and the width of the broadened monochromatic light pulse is narrower. The second cause of the inherent error is directly related to the broadened pulse width. Each of the broadened pulses has a finite pulse width which causes blur in the output by the superposition of the pulses due to the convolution nature of the output from the spectrometer. This part of error can not be corrected by normalization.

All the above analysis is confirmed by the numerical simulation results presented in Fig.4.4$\sim$ Fig.4.7 and Appendix A. The error Δ_1 in the normalized simulation results (normalized results of Eq.(3.38)) using the accurate model are presented in those figures. They indicate that Δ_1 could not be completely canceled out through normalization. The error is larger when the fiber has larger higher order dispersion. This phenomenon is due to the first part of the error. In addition, when the broadened pulse has a narrower pulse width in the time domain, less error is introduced to the results. This is the effect of the second part of the error. When a 1ns pulse is used (the situation in Fig.4.4(a)(c)(e)$\sim$Fig.4.7(a)(c)(e)), the

corresponding broadened pulse width is 1ns; when a 0.1ns pulse is used (the situation in Fig.4.4(b)(d)(f)∼Fig.4.7(b)(d)(f)), the corresponding broadened pulse width is 0.11ns. The errors in the results shown in Fig.4.4(b)(d)(f)∼Fig.4.7(b)(d)(f) are smaller than the corresponding ones in Fig.4.4(a)(c)(e)∼Fig.4.7(a)(c)(e). Moreover, for each simulation result, Δ_1 will have relatively higher value where the spectrum to be measured has a dramatical change. This phenomenon also results from the second part of the error. More results by using different pulse widths provided in Appendix A also give similar results which prove the conclusion made above. All these can be seen clearly in a generalization plot of errors provided in Fig.4.12. All the simulation results also indicate that the pulse shape does not have a large contribution to Δ_1 and its effects should be categorized to effects of the second part of Δ_1, the pulse width induced error.

In addition to the above analysis, the GVD of the fiber used in the system should not have different signs in the measurement range i.e. the β_1 of the fiber is monotonously increasing or decreasing in order that lights with different wavelengths are delayed according with the increase or decrease of light frequency or wavelength, and the modulation pulses should have a spectral width not comparable to the frequency of the light so that the shape of the light pulses are not severely distorted or destructed after broadening. Only under these conditions, the measurement results, $s_\lambda(\lambda)$ from the spectrometer can truly represent the spectrum of the incoming light.

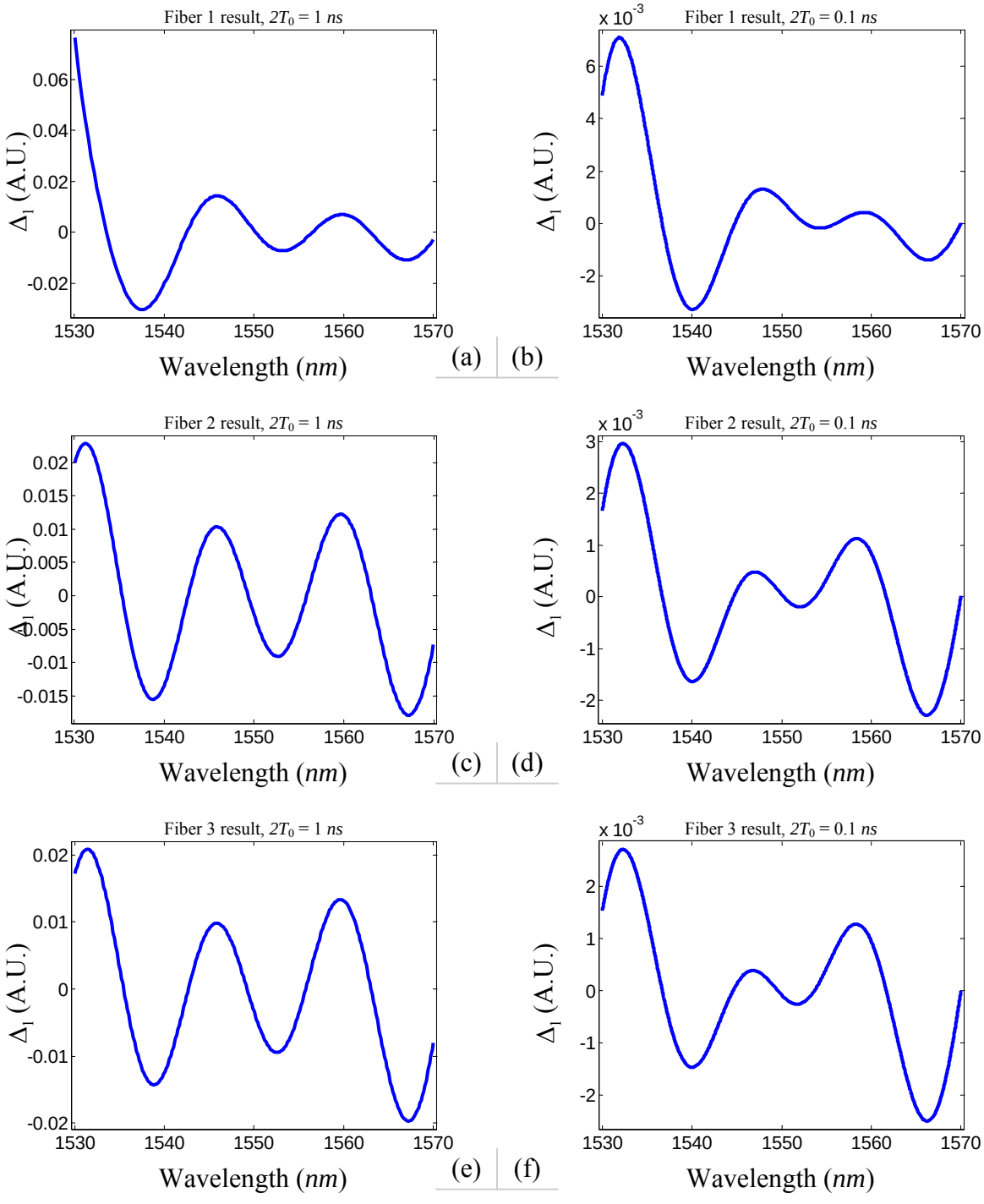

Figure 4.4: Simulation results of the inherent error Δ_1 (Gaussian pulse, FP spectrum, $DL = 1ns/mn$)

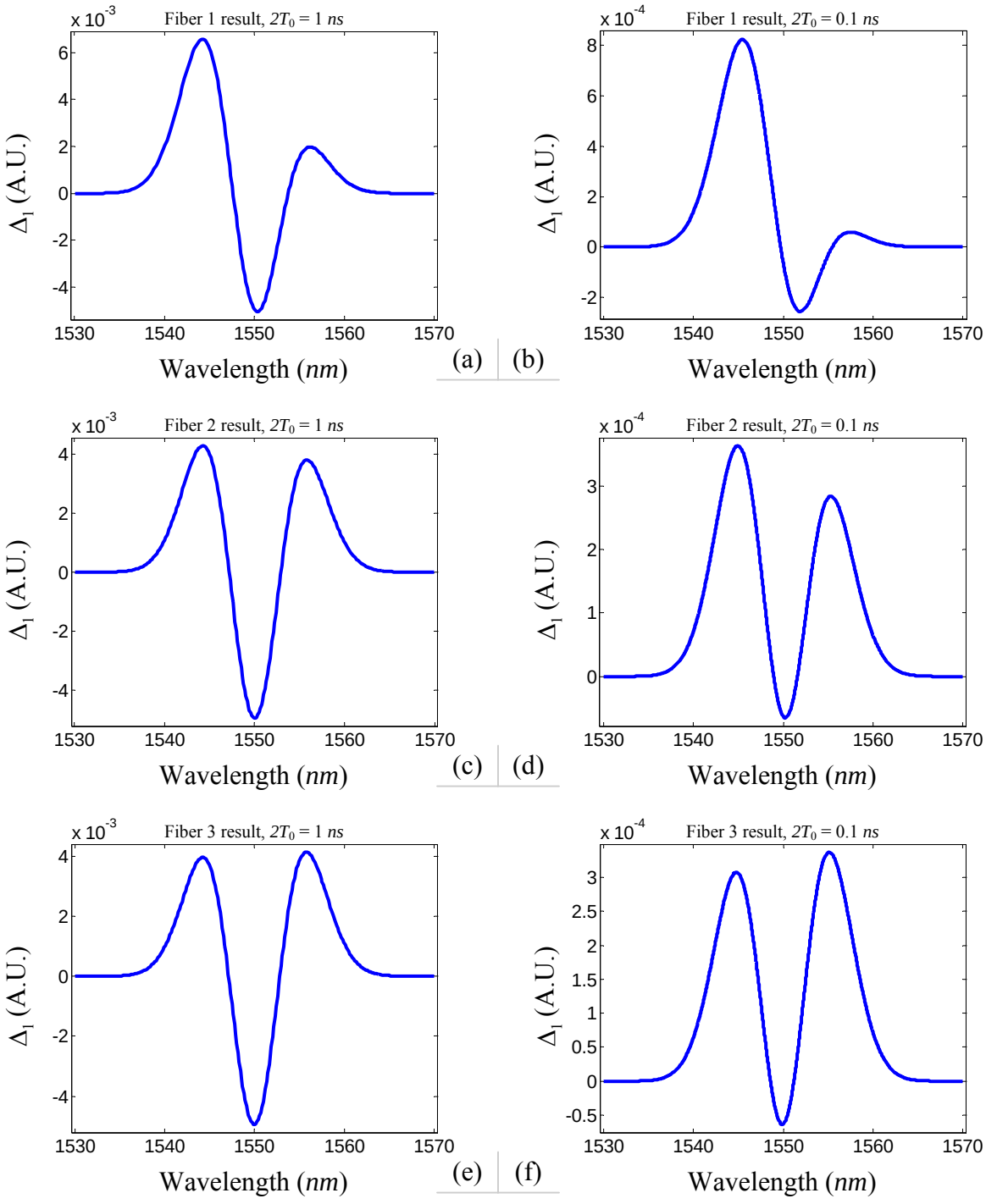

Figure 4.5: Simulation results of the inherent error Δ_1 (Gaussian pulse, Gaussian spectrum, $DL = 1ns/mn$)

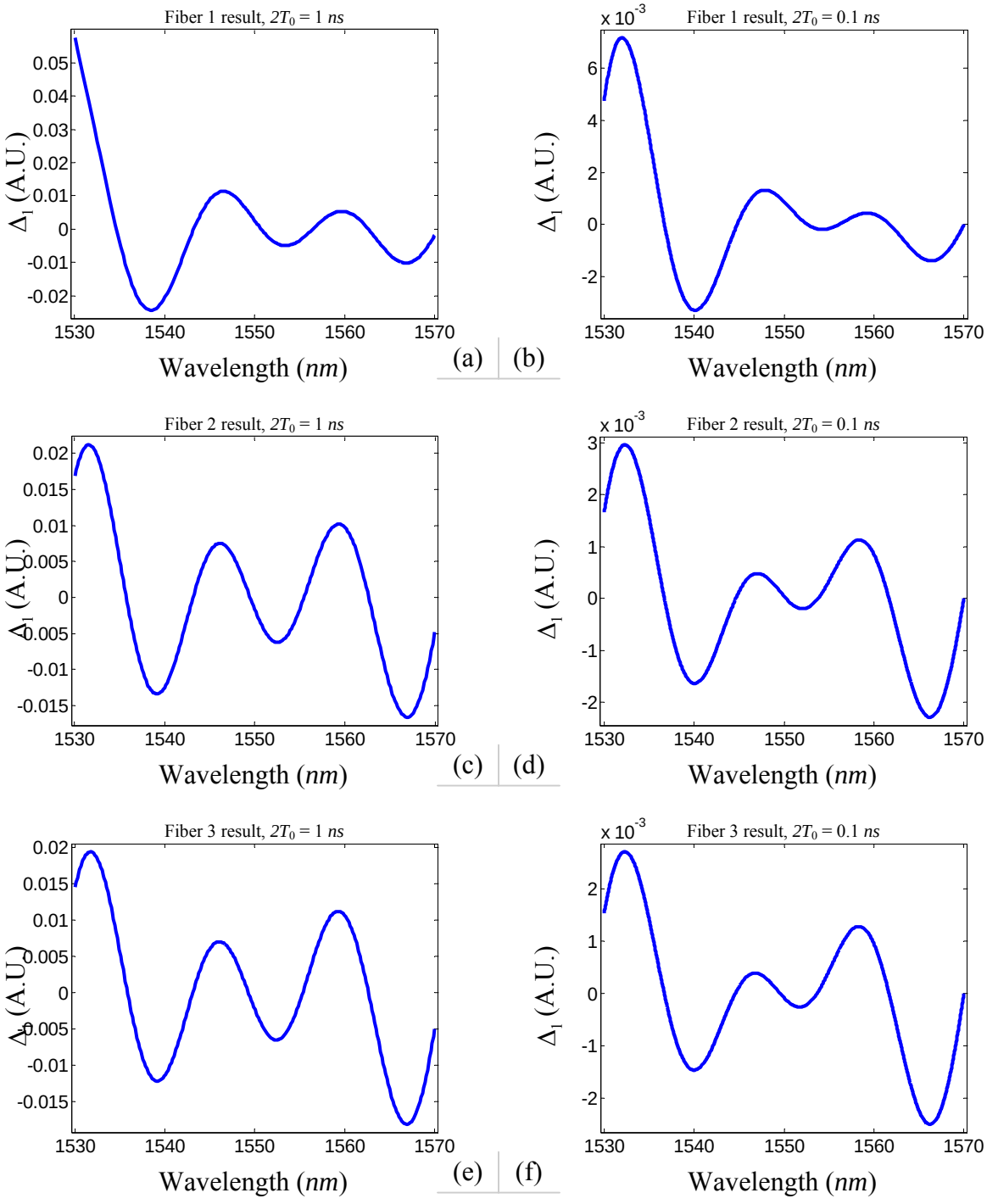

Figure 4.6: Simulation results of the inherent error Δ_1 (rectangular pulse, FP spectrum, $DL = 1ns/mn$)

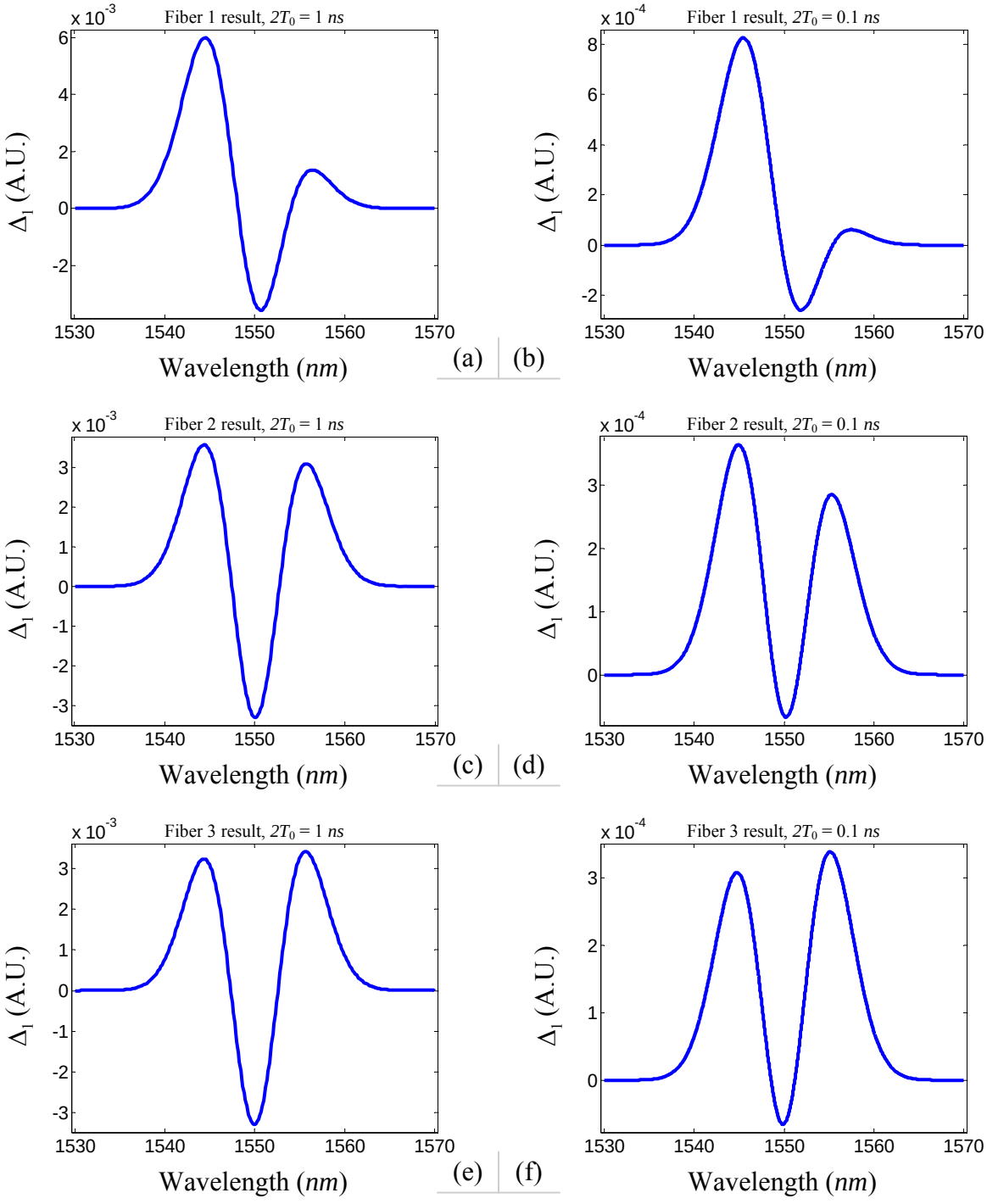

Figure 4.7: Simulation results of the inherent error Δ_1 (rectangular pulse, Gaussian spectrum, $DL = 1ns/mn$)

4.1.2 Model error

The model error Δ_2 is generated during the derivation of the approximate model as presented in Eqs.(3.32)$\sim$(3.36). The error is defined as the difference between the normalized results from Eqs.(3.39) and (3.38):

$$\Delta_2 = (P_{n\lambda}(0,\lambda) * M_\lambda(L,\lambda))_{normalized} - \left(\int_{-\infty}^{+\infty} P_n(0,t_d) M_\lambda(L,\lambda,t_d)\mathrm{d}t_d\right)_{normalized}. \quad (4.8)$$

This error is caused by using the broadened pulse centered at circular frequency ω_0 to approximate all other broadened pulse centered at circular frequencies other than ω_0 as described in Eq.(3.32). Δ_2 from the approximate model (normalized results of Eq.(3.39)) are presented in Fig.4.8$\sim$Fig.4.11. They indicate that results from the approximate model are closer to the results from the accurate model when the broadening of the pulse or the higher order dispersion is small. Especially when GVD is constant, the approximated model becomes the accurate model and the error Δ_2 reduces to 0 (The situation when fiber 3 is used). In addition, the convolution nature also makes Δ_2 relatively higher value where the spectrum has a dramatic change. Moreover, in all the simulation results presented in Fig.4.8$\sim$Fig.4.11, the errors from the approximation Δ_2 are much less than the corresponding errors Δ_1. This could be explained as follows. The pulses used in the simulation have a negligible spectral width comparing to the light frequency. The pulse broadening is then less determined by those higher order dispersions parameters. So in the spectral range that the spectrometer handles, the monochromatic light pulses with different wavelengths can be treated as uniformly broadened. When narrower pulses are used, Δ_2 may become equal or larger than Δ_1. This can be seen in additional simulation results provided in Appendix A and in the generalized plot of the errors shown in Fig.4.12. All the simulation results also indicate that the pulse shape does not have a large contribution to Δ_2. Its effects should be categorized to effects of pulse width too.

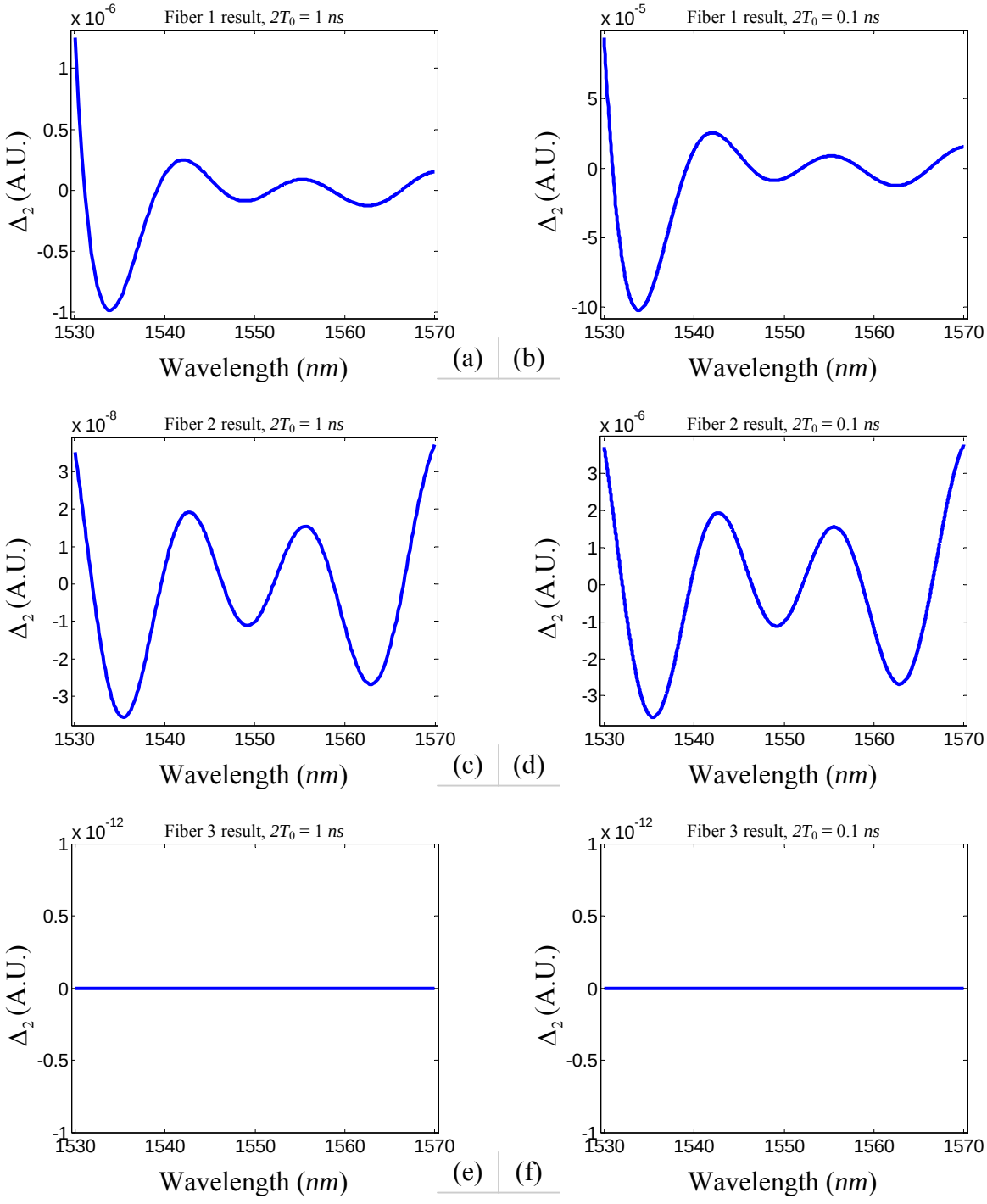

Figure 4.8: Simulation results of the model error Δ_2 (Gaussian pulse, FP spectrum, $DL = 1ns/mn$)

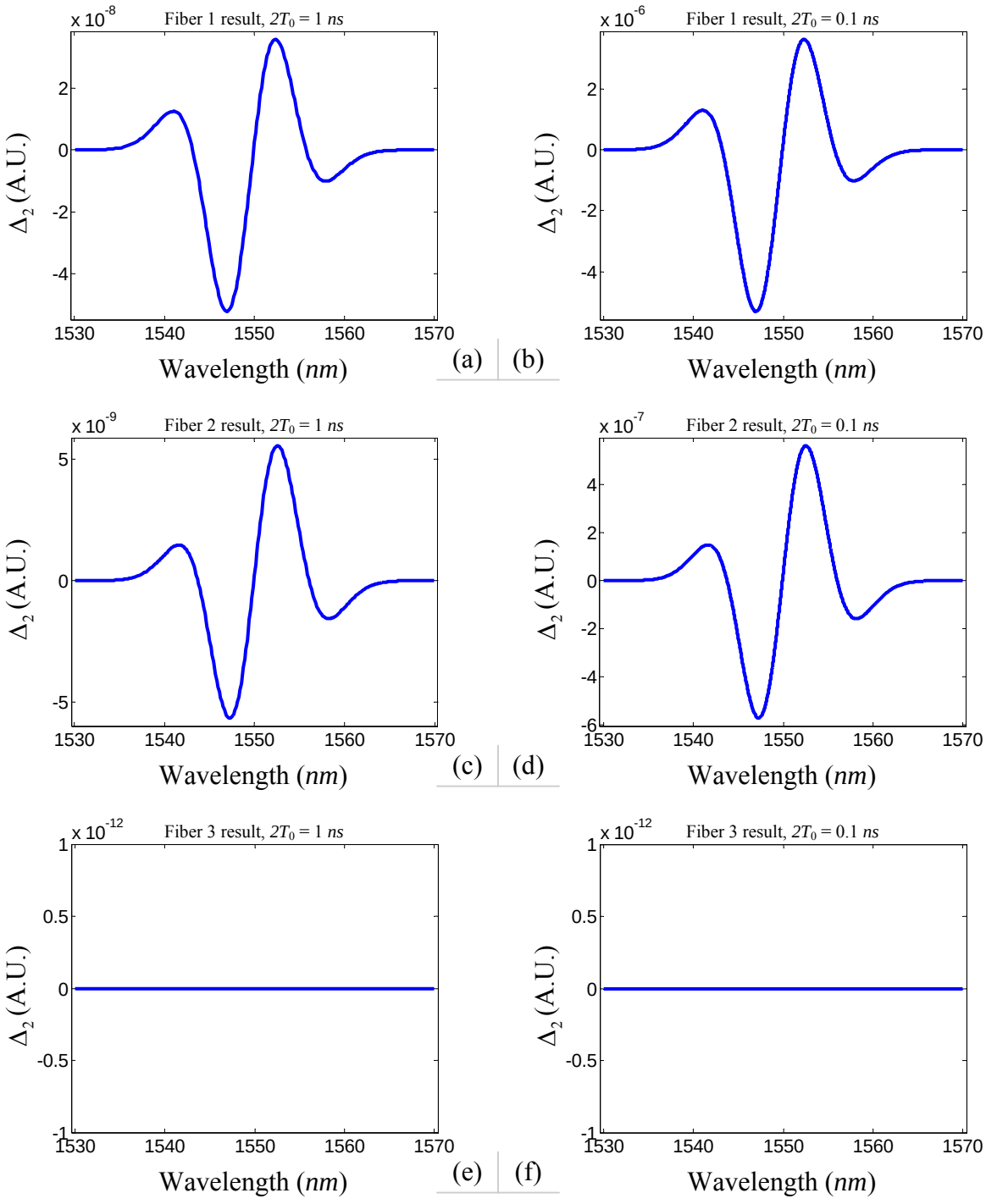

Figure 4.9: Simulation results of the model error Δ_2 (Gaussian pulse, Gaussian spectrum, $DL = 1ns/mn$)

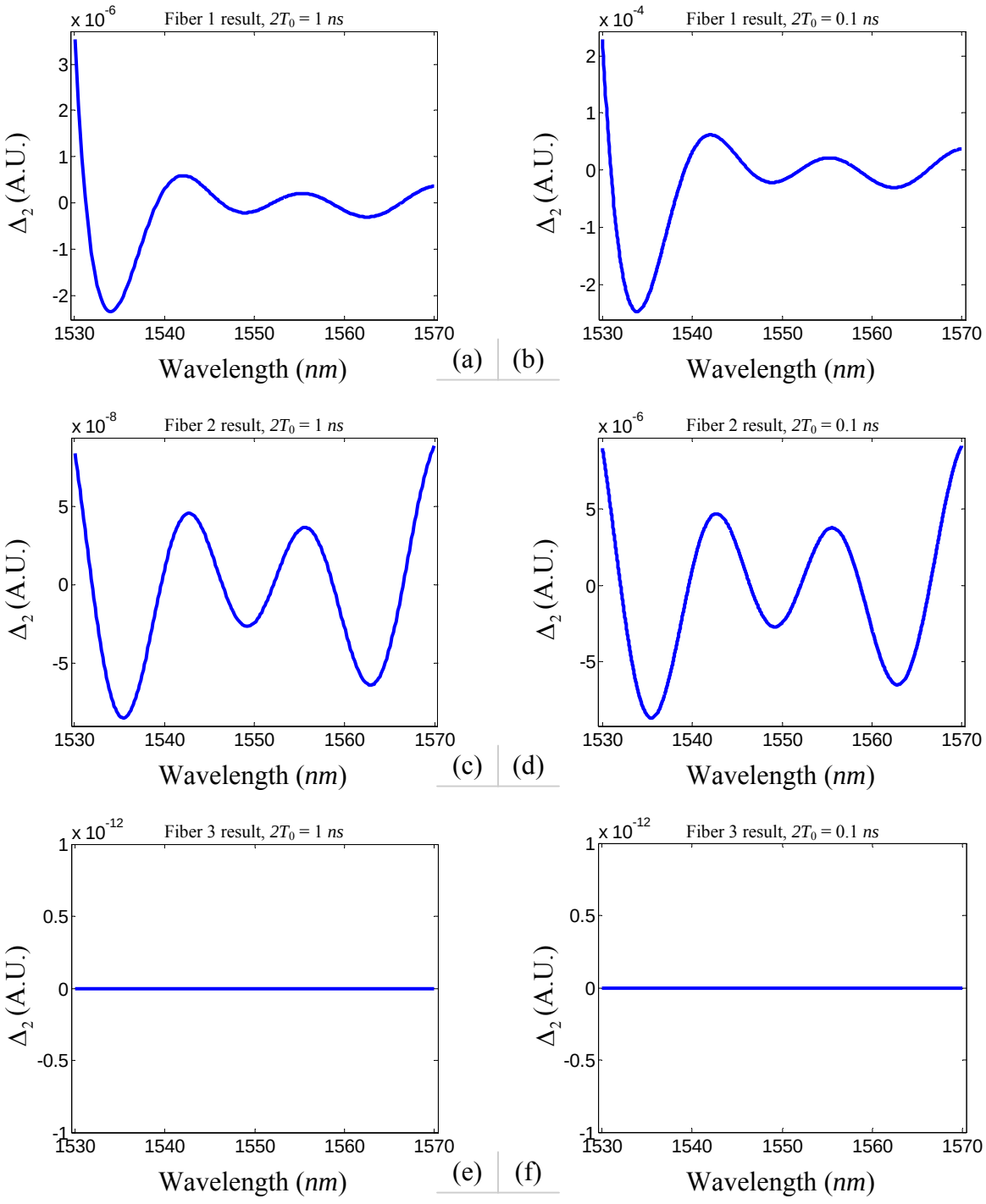

Figure 4.10: Simulation results of the model error Δ_2 (rectangular pulse, FP spectrum, $DL = 1ns/mn$)

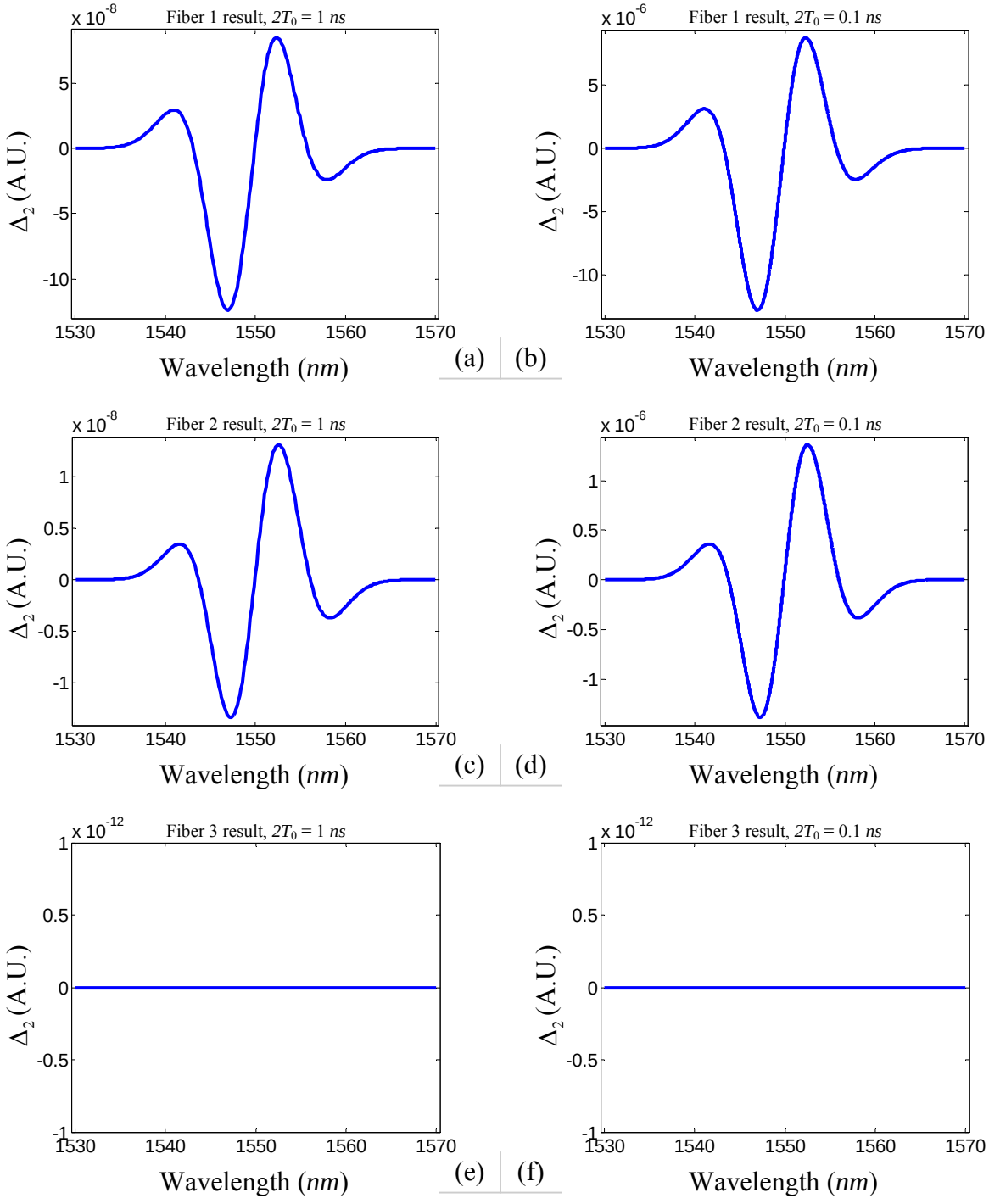

Figure 4.11: Simulation results of the model error Δ_2 (rectangular pulse, Gaussian spectrum, $DL = 1ns/mn$)

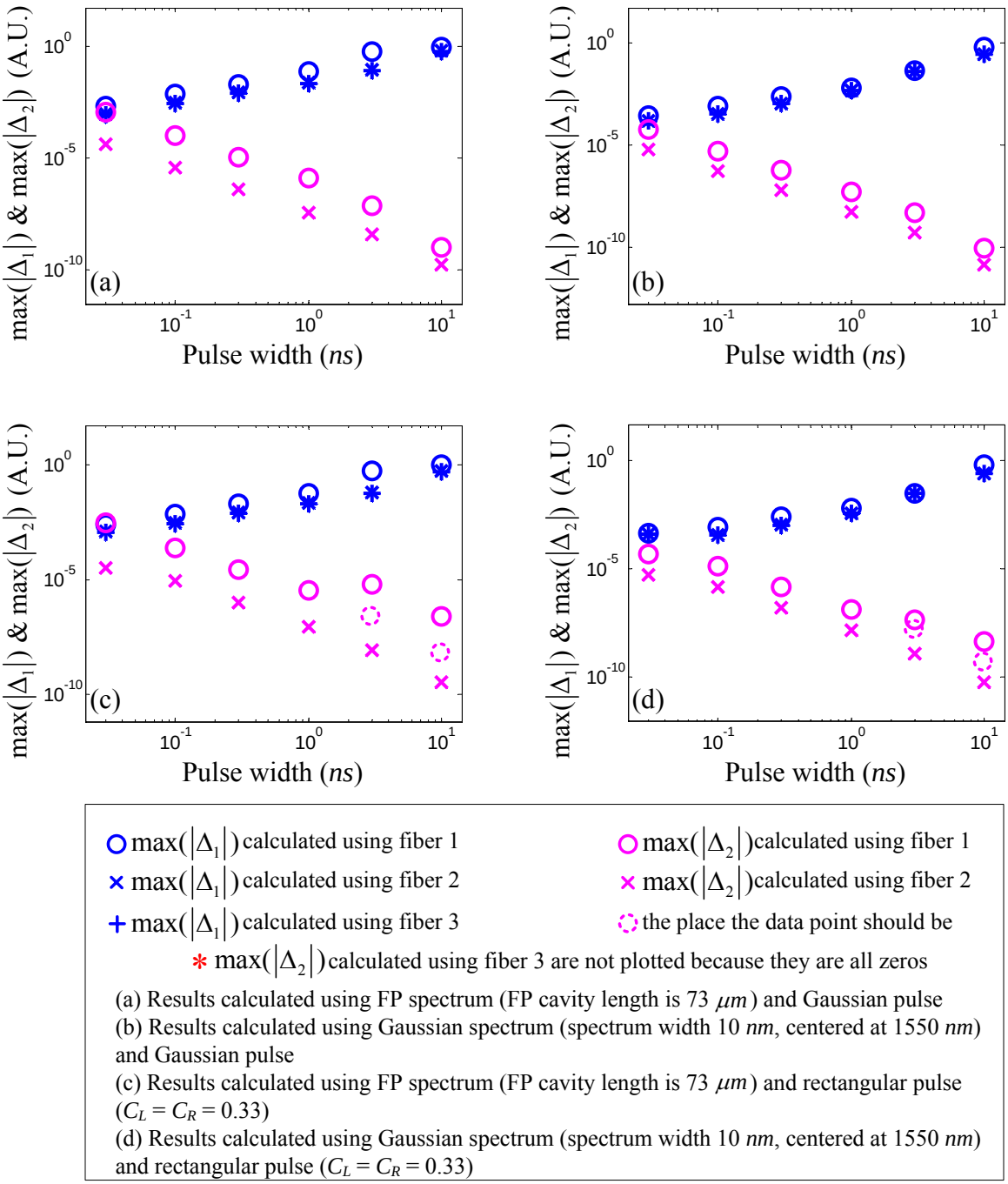

Figure 4.12: Relationship between the maximum of $|\Delta_1|$ and $|\Delta_2|$ in each error curve, fiber type, pulse width and pulse shape

4.2 Resolution

In this section, one analytical results of spectral resolution is first provided with the Gaussian modulation pulses and under the condition of neglecting the higher order dispersion. The effects of different parameters such as the pulse width and the amount of dispersion on the spectral resolution are discussed. Then the results from numerical simulation are presented and the results from both the methods are compared. Further, the effect of pulse shape is investigated.

4.2.1 Analytical results

The spectral resolution of a spectrometer is usually defined by the minimum wavelength difference between two adjacent peaks with the same intensity in one spectrum, which can be separated by the spectrometer. As shown in Fig.4.13, two spectral components with different wavelengths located at λ_1 and λ_2 respectively. The spectrum of the light with the two components is the superposition of the two single spectra. In the following analysis, the pulses are first assumed to be Gaussian type in order to derive an analytical result. The spectral resolution limit is defined by the wavelength difference between the two pulses when their $1/e$ intensity points are overlapped.

The analytical estimation of the spectral resolution can be conducted as follows. The modulation signal $m_0(t)$ is a Gaussian pulse with a width of $2T_0$ measured at $1/e$ intensity point:

$$m_0(t) = \exp\left(-\frac{t^2}{2T_0^2}\right). \tag{4.9}$$

The origin of the time axis is located at the center of the pulse. From Eq.(3.9), the spectrum of the modulation signal is

$$f_0(\omega) = \frac{T_0}{\sqrt{2\pi}} \exp\left(-\frac{\omega^2 T_0^2}{2}\right). \tag{4.10}$$

For the purpose of simplicity, ignoring the derivatives of the propagation constant β with orders higher than 2, the spectrum of the dispersed light pulse can be derived from Eq.(3.21).

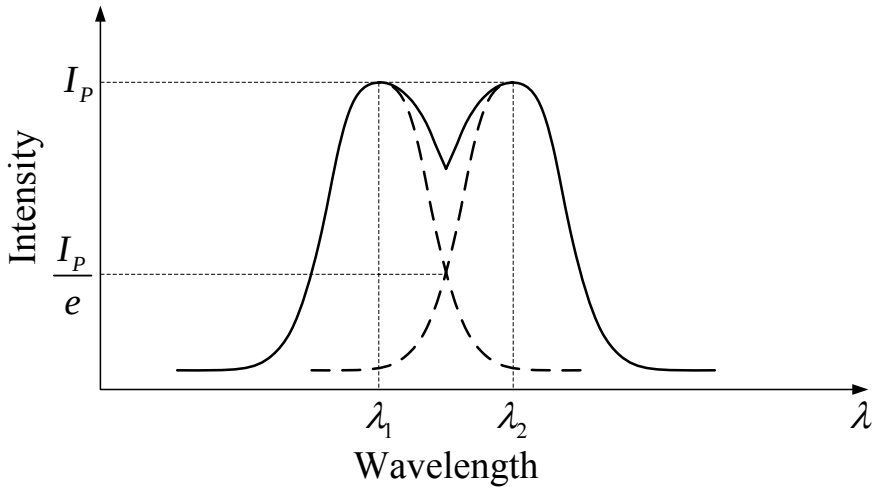

Figure 4.13: Definition of spectral resolution

Here we should notice that, since β_2 becomes constant, $f(L, \omega'', \omega')$ is no longer a function of ω' and it becomes $f'(L, \omega'')$:

$$f'(L, \omega'') = \frac{t_0}{\sqrt{2\pi}} \exp\left(\frac{-\omega''^2(j\beta(\omega_0)L + T_0^2)}{2}\right) \tag{4.11}$$

where ω_0 is the center frequency of the light pulse and $\beta_2(\omega_0) = \beta_2(\omega')$. Then the field of the broadened monochromatic light pulse is expressed as:

$$m'(L, t) = \frac{1}{\sqrt{1 + \frac{j\beta_2(\omega_0)L}{T_0^2}}} \exp\left(-\frac{t^2}{2T_0^2\left(1 + \frac{j\beta_2(\omega_0)L}{T_0^2}\right)}\right) \tag{4.12}$$

and the shape of the broadened pulse is:

$$M'(L, t) = \frac{1}{\sqrt{1 + \left(\frac{\beta_2(\omega_0)L}{T_0^2}\right)^2}} \exp\left(-\frac{t^2}{T_0^2\left(1 + \left(\frac{\beta_2(\omega_0)L}{T_0^2}\right)^2\right)}\right). \tag{4.13}$$

In Eq.(4.13), the origin of the time axis is also located at the center of the pulse. The half width of the broadened pulse is expressed as:

$$T_0' = T_0\sqrt{1 + \left(\frac{\beta_2(\omega_0)L}{T_0^2}\right)^2}. \tag{4.14}$$

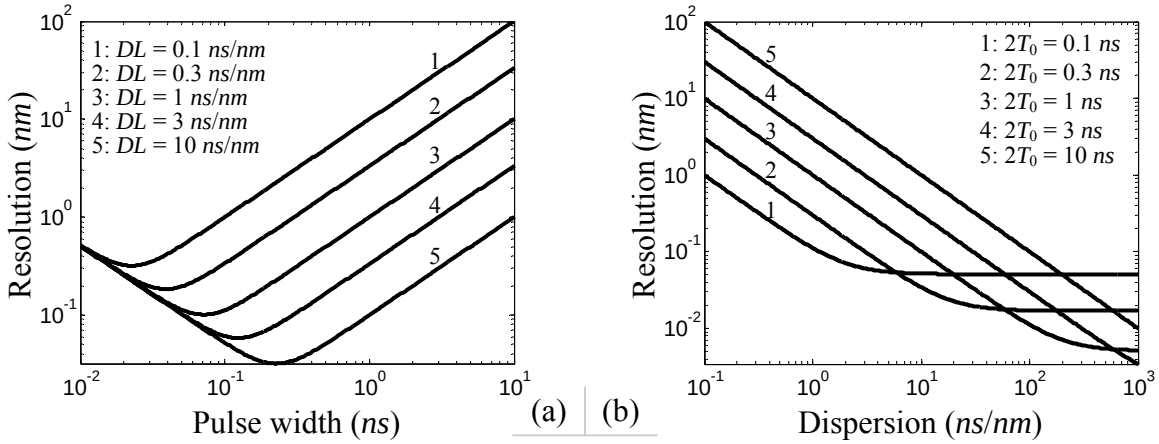

Figure 4.14: Relationship between spectral resolution, pulse width and dispersion DL

According to the spectral resolution criterion mentioned above, the spectral resolution of the spectrometer at wavelength λ_0 can be estimated by

$$r_\lambda = \frac{2T_0'}{D_L(\lambda_0)} = 2\sqrt{\left(\frac{T_0}{D_L(\lambda_0)}\right)^2 + \left(\frac{\lambda_0^2}{2\pi c T_0}\right)^2} \tag{4.15}$$

where

$$D(\lambda_0) = -\frac{2\pi c}{\lambda_0^2}\beta_2(\omega_0) \tag{4.16}$$

and

$$D_L(\lambda_0) = D(\lambda_0)L \tag{4.17}$$

are the dispersion parameter of the fiber at wavelength λ_0 and the total amount of dispersion introduced by the dispersive fiber, respectively. In the above equations, c is the speed of light in vacuum. The spectral resolution r_λ in Eq.(4.15) has its minimum:

$$r_{\lambda m} = 2\sqrt{\frac{\lambda_0^2}{\pi c|D_L(\lambda_0)|}} \tag{4.18}$$

at

$$T_0 = \sqrt{\frac{\lambda_0^2}{2\pi c}|D_L(\lambda_0)|}. \tag{4.19}$$

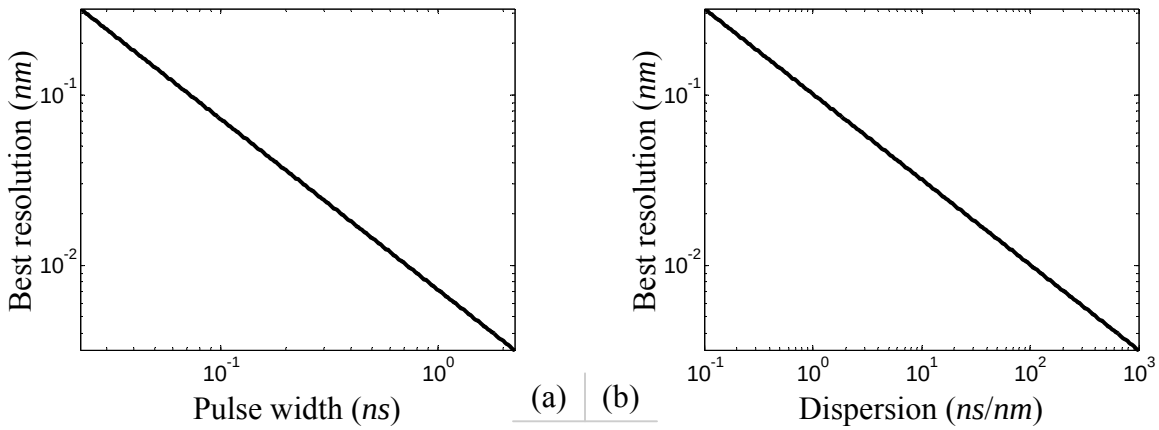

Figure 4.15: Relationship between the best spectral resolution, pulse width and dispersion DL

The above analysis indicates that for a specific wavelength λ_0 the spectral resolution is determined by the total amount of dispersion $D_L(\lambda_0)$ of the dispersive fiber and the initial width $2T_0$ of the light pulse. When the amount of dispersion is fixed, there exists an optimal pulse width at which the best spectrum measurement resolution is achieved as shown by Fig.4.14(a). This is so because the output pulse broadening caused by the inherent bandwidth of the modulation pulse and the GVD of the dispersion element is dominant when the pulse is sufficiently narrow. Whereas the broadened pulse width due to the initial pulse width is dominant when the pulse width is larger. Fig.4.14(b) shows the relationship between the spectral resolution and the total dispersion of the fiber for different pulse widths. It is indicated that, for each fixed initial pulse width $2T_0$, the value of the spectral resolution decreases rapidly when the dispersion is smaller than the value determined by Eq.(4.19). The relation between the best spectral resolution and the corresponding initial pulse width $2T_0$ is illustrated in Fig.4.15(a). In Fig.4.15(b), the best spectral resolution is presented as a function of the dispersion.

4.2.2 Numerical results

In this subsection, the higher order dispersion parameters are no longer ignored. As a result, the profile of the dispersed light pulses can only be acquired through numerical simulation. The numerical analysis results using Gaussian pulses and rectangular pulses are presented in Fig.4.16 and Fig.4.17, respectively. The fiber used in the simulation is fiber 2. Other simulation results using fiber 1 and fiber 3 are listed in appendix B. The analytical results are also plotted in both figures for the purpose of comparison. The rectangular pulses used in the simulation have a shape close to the pulse used in the experiments. Fig.4.16 and other results listed in Appendix B which uses Gaussian pulses show that the differences between the analytical results and the numerical results are negligible. This can be explained as the pulse widths used in the analysis are still large such that their spectral width are not comparable to the light frequency. Under this condition, the higher order dispersion has little effects on the light pulse broadening. So the analytical results can provide good direction for resolution analysis when the Gaussian pulse width is greater than 0.03 ns.

Fig.4.17(a) indicates that for a given dispersion value, these rectangular pulses can realize a better resolution value than Gaussian pulses at certain pulse widths. When the pulse width is less than a specific value, the spectrometers using rectangular pulses have worse resolution. But as the pulse width increases, these spectrometers can achieve a better resolution in a small region. If the pulse width keeps increasing, their resolution becomes equal to those using Gaussian pulses. Fig.4.17(b) shows that for a fixed pulse width, the rectangular pulses can help the spectrometers to provide better resolution in a small dispersion value range. When the amount of dispersion is larger than the value in the range, Gaussian pulses can yield a much better resolution. When the dispersion is less than that value, both types of pulses give the same resolution. To further investigate the effects of the pulse shape on the spectral resolution, rectangular pulse with the same width but different C_L and C_R are used to conduct more simulations. The results are presented in Fig.4.18 and Fig.4.19.

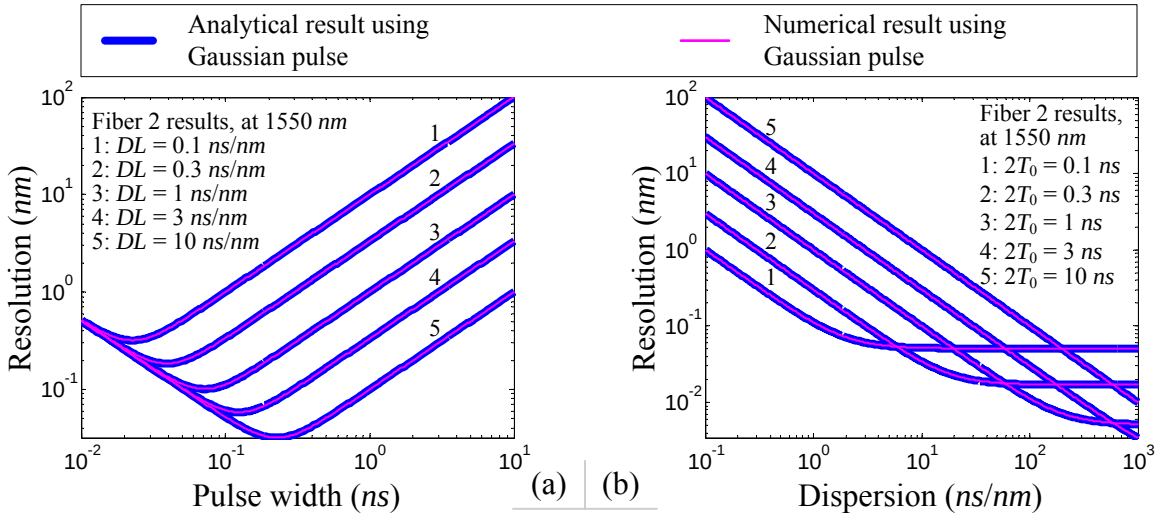

Figure 4.16: Simulation results of the spectral resolution when Gaussian pulses are used

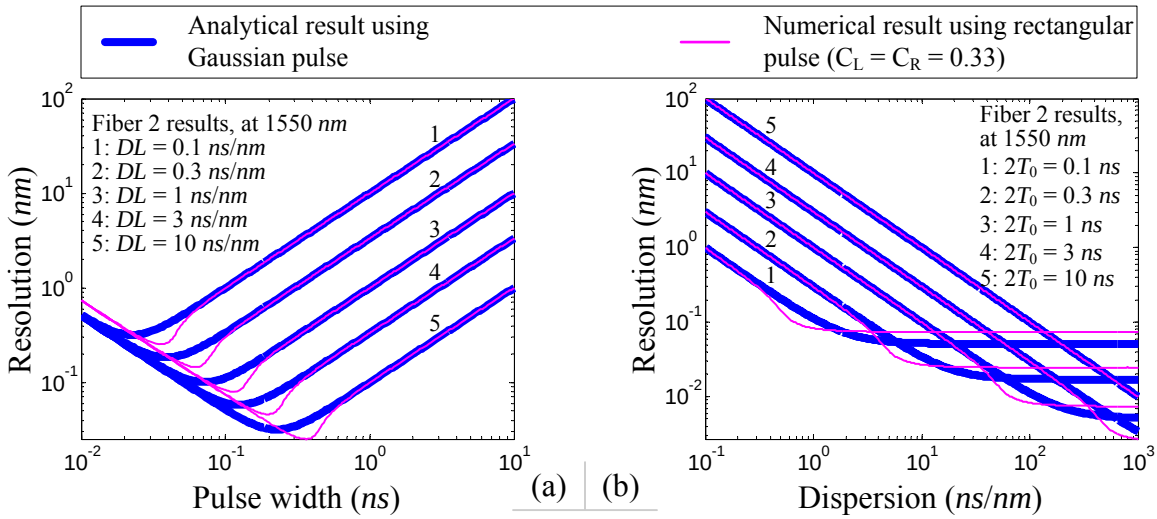

Figure 4.17: Simulation results of the spectral resolution when rectangular pulses are used(1)

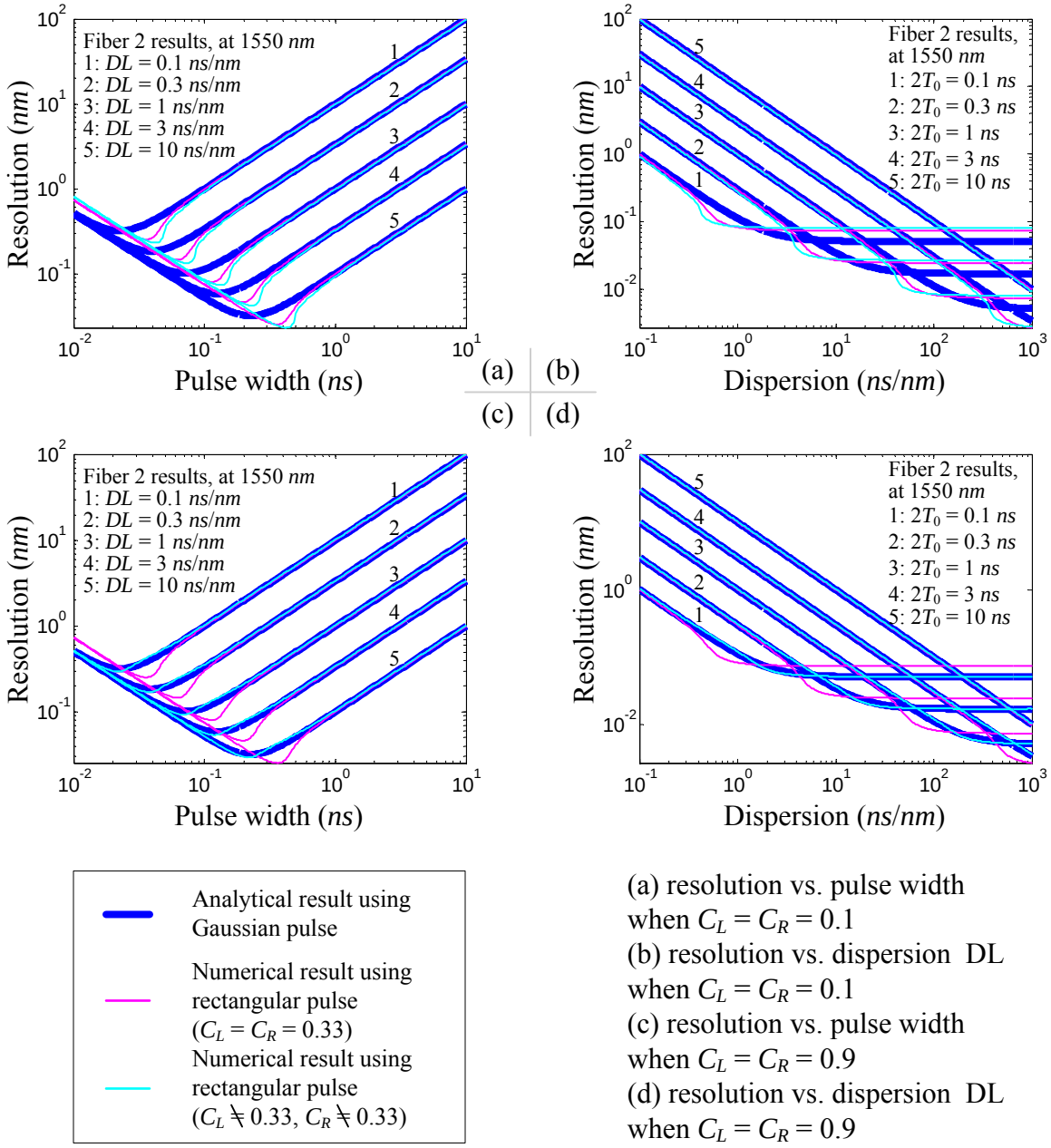

(a) resolution vs. pulse width when $C_L = C_R = 0.1$
(b) resolution vs. dispersion DL when $C_L = C_R = 0.1$
(c) resolution vs. pulse width when $C_L = C_R = 0.9$
(d) resolution vs. dispersion DL when $C_L = C_R = 0.9$

Figure 4.18: Simulation results of the spectral resolution when rectangular pulses are used(2)

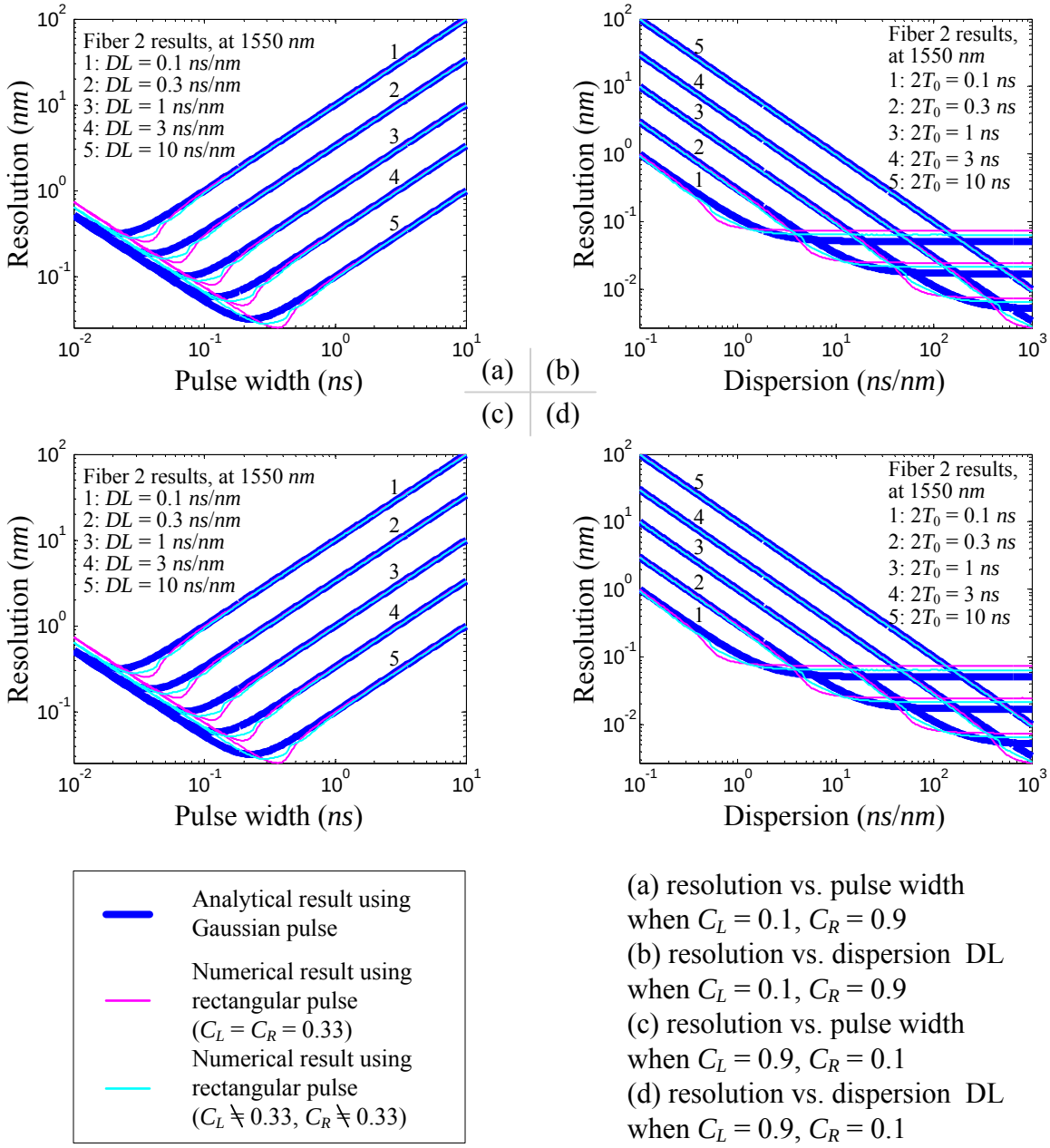

(a) resolution vs. pulse width when $C_L = 0.1$, $C_R = 0.9$
(b) resolution vs. dispersion DL when $C_L = 0.1$, $C_R = 0.9$
(c) resolution vs. pulse width when $C_L = 0.9$, $C_R = 0.1$
(d) resolution vs. dispersion DL when $C_L = 0.9$, $C_R = 0.1$

Figure 4.19: Simulation results of the spectral resolution when rectangular pulses are used(3)

Fig.4.18 shows that the rectangular pulses with sharper edges ($C_L = C_R = 0.1$) achieve the best resolution value for a given amount of dispersion which is less than half of the best resolution value that the Gaussian pulses can achieve with the same dispersion. Fig.4.19 illustrates that the two asymmetric rectangular pulses provide the same results no matter whether the sharper edge is the rising edge or the falling edge. One thing that should be noticed is the reason that the rectangular pulses can improve the spectral resolution is not chirp, but that they have special spectrum structures. This can be proven by changing the sign of the fiber dispersion. If the resolution advantages are caused by chirp, the resolution would not be the same under the same absolute dispersion value with a different sign. In Fig.4.20(a) and (b), the dispersion properties of fiber 2 and fiber 2A are presented. The absolute dispersion values of fiber 2A are the same as those of fiber 2. The only difference is the sign of the dispersion. In Fig.4.20(c) and (d) the results for rectangular pulses ($C_L = C_R = 0.33$) are given. Although the fibers are different, the resolution results are the same. For the results shown in Fig.4.20(e) and (f), the pulses used are still the same rectangular pulse. Linear chirp is added to the pulses and the chirp parameter C is set to 1. When the chirp has the same sign as the dispersion value, the resolution is worse; when the chirp has a different sign as the dispersion value, the resolution becomes better. These results confirm the above conclusions. When the light pulses travel through a dispersive fiber, the Gaussian pulses are continuously broadening (when there is no chirp); whereas the rectangular pulses will have some narrower pulse widths compared to the initial pulse width at certain places due to the reconstruction of pulse through harmonic superposition. This can be seen clearly in Fig.4.21 (the initial pulse widths are all 0.1 ns). In general, properly choosing pulse shape for a certain pulse width and amount of dispersion will give better resolution.

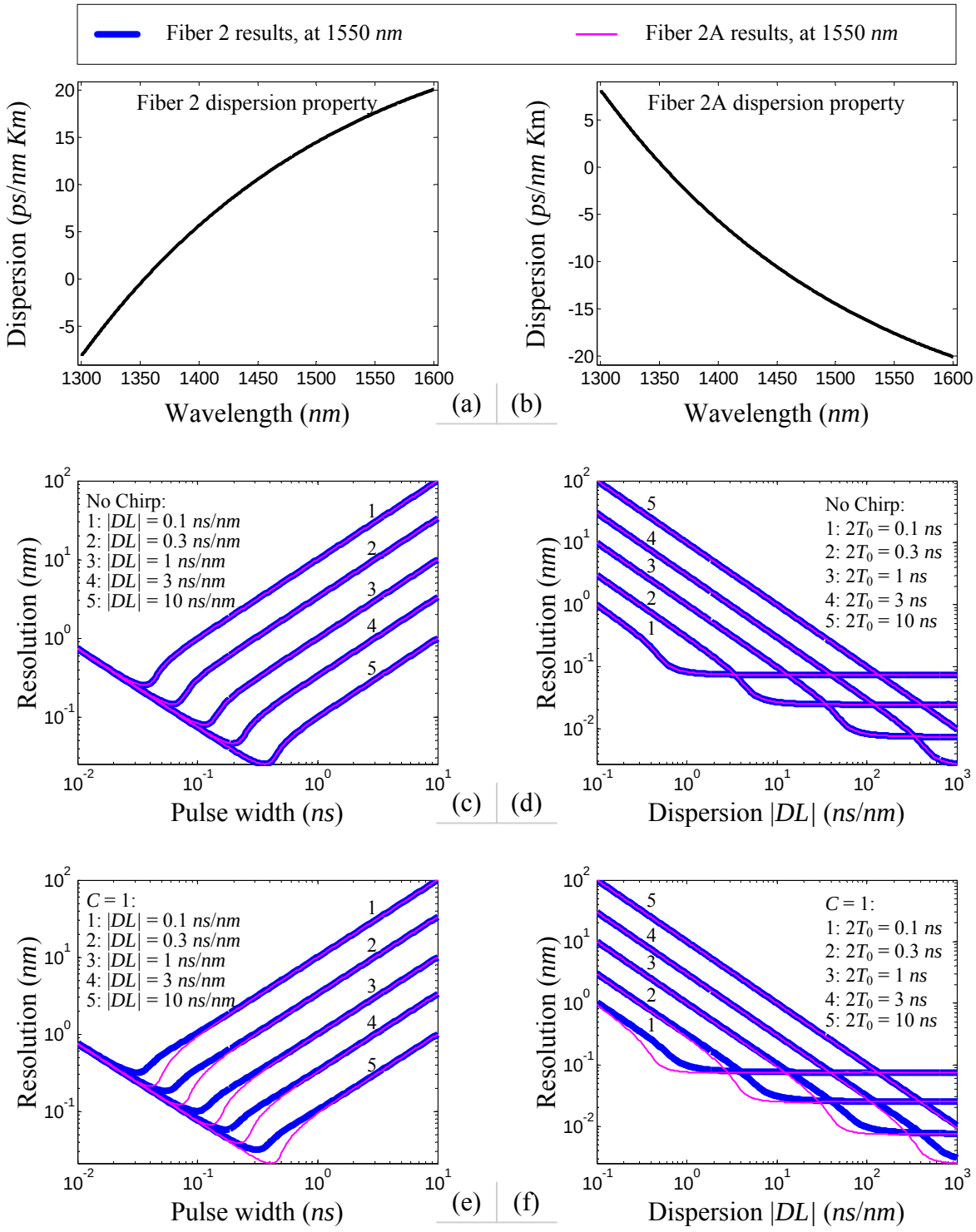

Figure 4.20: Resolution achieved by pulses with and without chirp

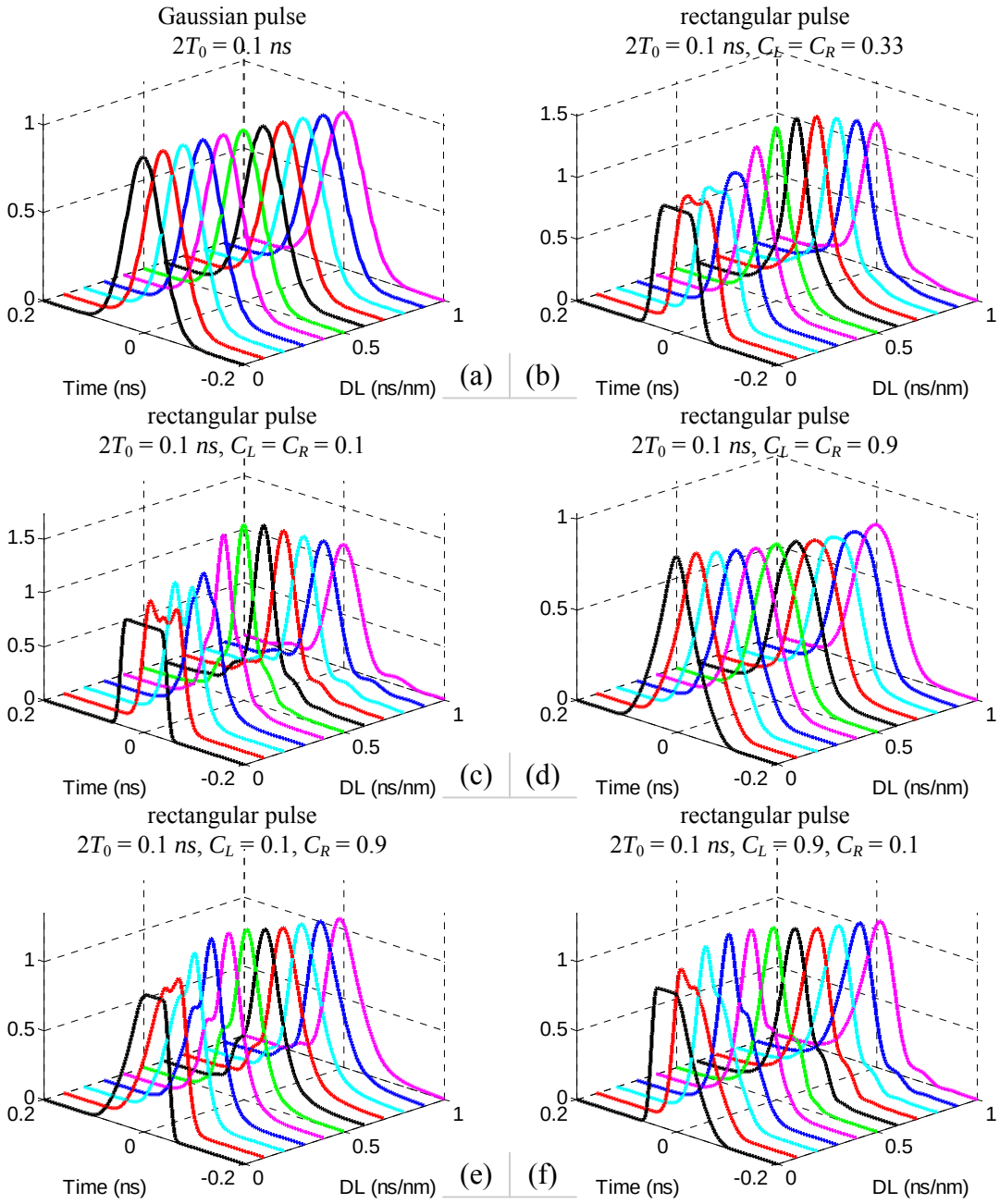

Figure 4.21: Pulse broadening of Gaussian and rectangular pulses

4.3 Speed

In this section, the analysis of speed is based on the ideal conditions. In a real spectrometer, the speed is not only limited by the parameters used in the following analysis, but also related to many other conditions e.g., the performance of the DAQ and the processing speed of the computer. For the purpose of simplicity, only Gaussian pulses are used in the analysis so that analytical results can be derived and the relationship between speed and such major parameters as pulse width, amount of dispersion and resolution can be revealed.

The speed of the spectrometer is defined as the number of spectrum frames acquired per unit time. It is mainly determined by the width of the broadened chromatic light pulses in the time domain. The time interval between two consecutive pulses must be larger than this pulse width; otherwise measurement error could be introduced by the overlap between two consecutive pulses. Three parameters affect the width of the broadened output pulses. They are: the width of the spectrum to be measured, the amount of dispersion introduced by the dispersive fiber, and the properties of the modulation pulse. For a Gaussian pulse, the intensity at $t = \pm 3T_0$ decreases to 10^{-4} of the peak intensity. The width of the chromatic light pulse measured at the 10^{-4} intensity point can be roughly estimated by

$$T_s = \Delta\lambda D_L(\lambda_0) + 6T_0' \tag{4.20}$$

where T_s is the output pulse width and $\Delta\lambda$ is the -3 dB spectral width of the incoming light. The maximum speed is defined as the speed at which the 10^{-4} intensity points of the two adjacent output pulses are overlapped. Therefore the maximum speed is estimated by

$$f_m = \frac{1}{T_s} = \left(\left(\Delta\lambda + 6\sqrt{\left(\frac{T_0}{D_L(\lambda_0)}\right)^2 + \left(\frac{\lambda_0^2}{2\pi c T_0}\right)^2} \right) D_L(\lambda_0) \right)^{-1}. \tag{4.21}$$

When the half initial pulse width T_0 equals the value presented in Eq.(4.19), the best spectral resolution is reached for a given dispersion value. Fig.4.22(a) illustrates the maximum speed as a function of the spectral width when the best spectral resolution for each dispersion value

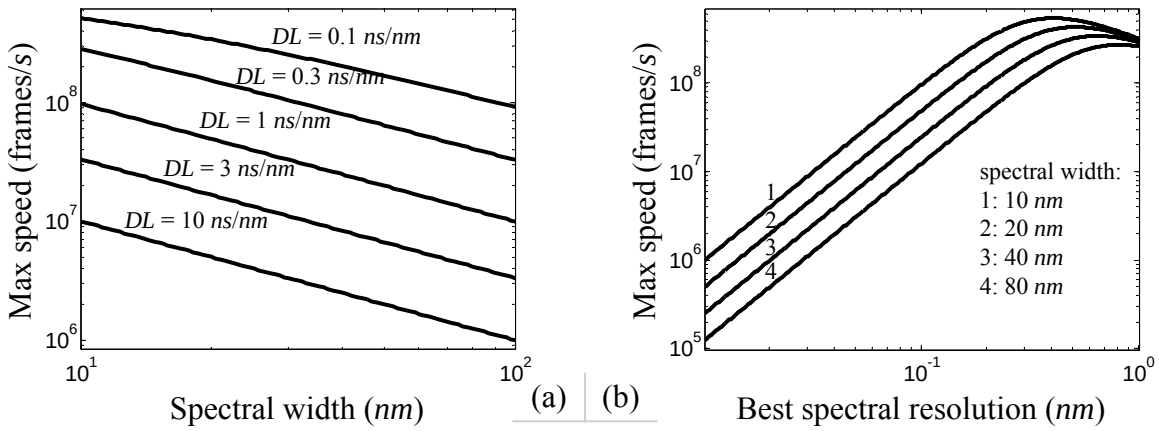

Figure 4.22: Relationships between the maximum spectrum acquisition rate, the spectral width and the spectral resolution

is reached. The best spectral resolution of 0.32, 0.18, 0.10, 0.06 and 0.03 nm correspond to dispersion value of 0.1, 0.3, 1, 3 and 10 ns/nm, respectively. In the Fig.4.22(b), the relationship between the maximum speed and the best resolution is presented.

Fig.4.22(a) indicates that the maximum speed decreases as the spectral width increases or as the total amount of dispersion increases. For all five dispersion values, the measurement speeds are above 10^6 frames/s when the spectral widths are less than 100 nm. Fig.4.22(b) shows that there is a tradeoff between the best achievable spectral resolution and the maximum measurement speed. In addition, for each spectral width, a highest value of the maximum measurement speed exists. On the left side of each curve relative to its highest value, the increase of the dispersion which results in the spectral resolution improvement lowers the maximum measurement speed; on the right side of each curve to its highest value, the pulse broadening causes the decrease of the maximum measurement speed.

4.4 Noise

In the HSFOS, the main noise sources are the O/E converter, the DAQ (the oscilloscope used in the experiment) and the erbium-doped fiber amplifier(EDFA). EDFAs are used to compensate the loss in the optical path. The following analysis is based on experimental results and the contribution of each noise source is determined. The block diagrams of the two setups used in the experiments are shown in Fig.4.23 and Fig.4.24 respectively. The O/E converter used is a HP 11982A which has a bandwidth of 15 GHz and a responsivity greater than 200 V/W (The nominal resopnsivity is 300 V/W). The oscilloscope is a Lecroy LC 574A whose bandwidth is 1 GHz. The output impedance of the O/E converter and the input impedance of the oscilloscope are both 50 Ω. 50 Km SMF-28 single mode fiber is used as the dispersive fiber. The 10 Gb/s modulator is from JDSU which is based on a Mach-Zehnder interferometer and has an extinction ratio of 20 dB and a V_π of 6 V. For each setup, the experiment is conducted through several steps. In each step, a certain device is turned on or off. The noise voltage is acquired by measuring the standard deviation of the voltage signal through the build-in function of the oscilloscope. Each result is derived from 1000 repeated measurements. All the operation steps and the corresponding results are listed in Table 4.2 and Table 4.3. In the tables, the "on" of the modulator is defined as the status that its insertion loss reaches the minimum; the "off" of the modulator is defined as the status that its insertion loss reaches the maximum. In the following analysis, shot noise, thermal noise and amplifier noise in the O/E converter are calculated separately. The definitions for shot noise and thermal noise are listed in Eq.4.22 and Eq.4.23 respectively [89].

$$\sigma_s^2 = 2q(RP_{in} + I_d)B_W = 2q(I_p + I_d)B_W, \tag{4.22}$$

$$\sigma_t^2 = \frac{4k_BTB_W}{R_L}. \tag{4.23}$$

In the above equations, q is the electron charge, R is the responsivity of the photo detector, P_{in} is the incident optical power, I_p is the photocurrent, I_d is the dark current of the detector, B_W is the signal band width, k_B is the Boltzmann Constant, T is the absolute temperature, and R_L is the load resistance.

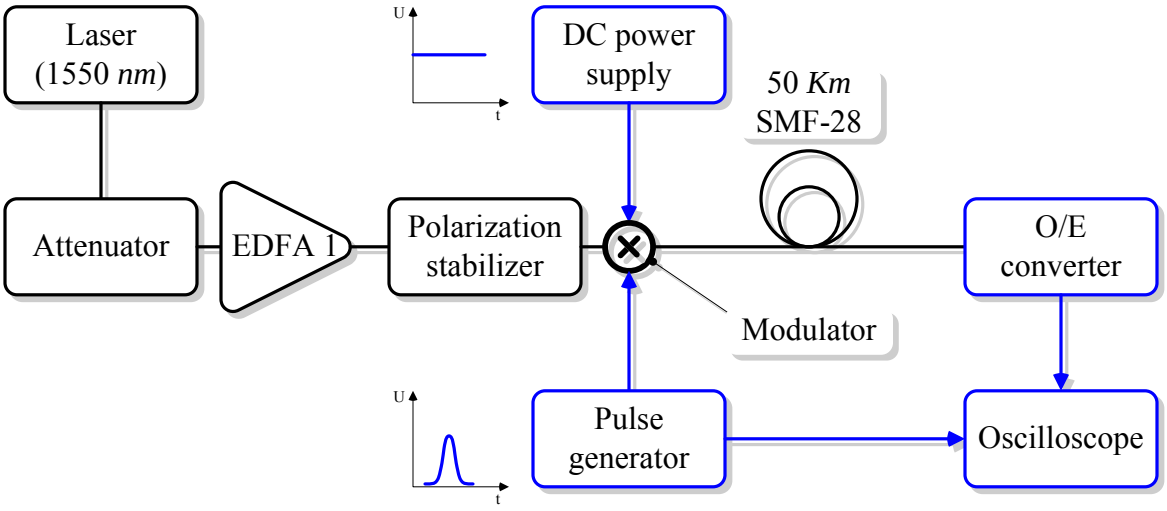

Figure 4.23: Block diagram of experiment setup 1

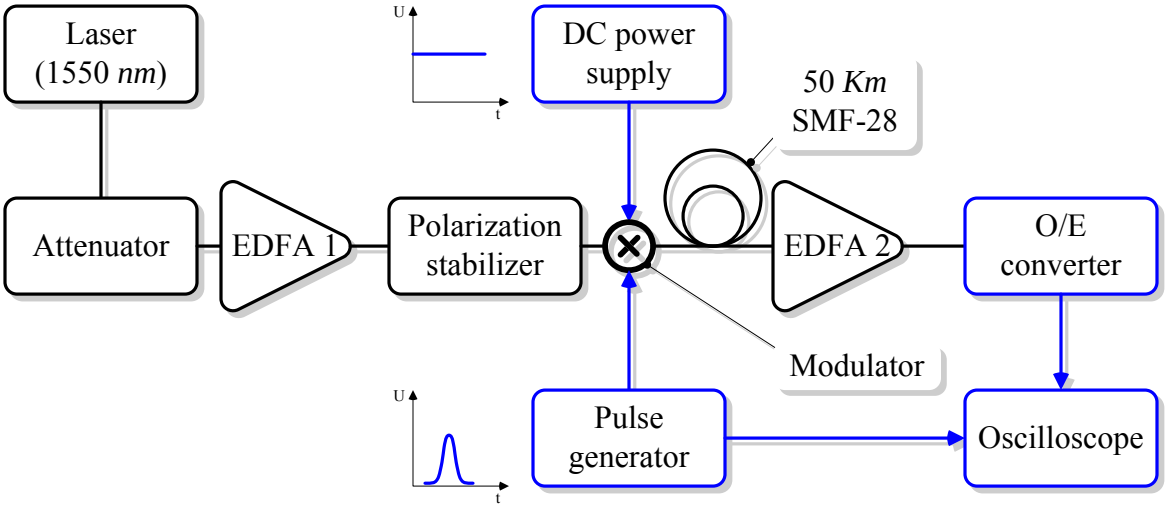

Figure 4.24: Block diagram of experiment setup 2

Table 4.2: Noise measurement results using experiment setup 1

	Step 1	Step 2	Step 3	Step 4	Step 5
1550 nm Laser	off	off	off	on	on
(output power (mW))	-	-	-	(20)	(20)
Attenuator attenuation (dB)	inf	inf	inf	10	10
EDFA 1	off	off	on	on	on
(gain (dB))	-	-	(21)	(21)	(21)
Polarization stabilizer	off	off	on	on	on
modulator status	off	off	off	off	on
O/E converter	off	on	on	on	on
Oscilloscope	on	on	on	on	on
Noise amplitude (mV)	0.22	0.30	0.30	0.30	0.48

Table 4.3: Noise measurement results using experiment setup 2

	Step 1	Step 2	Step 3	Step 4	Step 5	Step 6
1550 nm Laser	off	off	off	off	on	on
(output power (mW))	-	-	-	-	(20)	(20)
Attenuator attenuation (dB)	inf	inf	inf	inf	10	10
EDFA 1	off	off	off	on	on	on
(gain (dB))	-	-	-	(21)	(21)	(21)
Polarization stabilizer	off	off	off	on	on	on
modulator status	off	off	off	off	off	on
EDFA 2	off	off	on	on	on	on
(gain (dB))	-	-	(23)	(23)	(23)	(23)
O/E converter	off	on	on	on	on	on
Oscilloscope	on	on	on	on	on	on
Noise amplitude (mV)	0.22	0.30	0.30	0.30	0.35	23

In order to conduct estimation, we assume the responsivity of the photo detector is 0.8 A/W and the load resistance in the O/E converter is 300 Ω. For setup 1, at step 1, only the oscilloscope is on. The noise of the oscilloscope is calculated as

$$\sigma_{osc}^2 = \left(\frac{0.22 \times 10^{-3}}{50}\right)^2 = 1.936 \times 10^{-11} A^2.$$

In step 2, both the oscilloscope and the O/E converter are turned on, then

$$\sigma_{osc}^2 + \sigma_{O/E}^2 = \left(\frac{0.3 \times 10^{-3}}{50}\right)^2 = 3.6 \times 10^{-11} A^2,$$

$$\sigma_{O/E}^2 = 3.6 \times 10^{-11} - 1.936 \times 10^{-11} = 1.664 \times 10^{-11} A^2.$$

From Eq.4.23,

$$\sigma_t^2 = \frac{4k_B \times 300 \times 10^9}{300} = 5.52 \times 10^{-14} A^2.$$

Since in this step, no light source is turned on, the shot noise in the O/E converter is caused by the dark current. Knowing that the amplitude of the voltage signal is 0.8 mV, this part of shot noise is

$$\sigma_{sI_d}^2 = 2 \times 1.6 \times 10^{-19} \times \frac{0.8 \times 10^{-3}}{300} \times 10^9 \approx 8.53 \times 10^{-16} A^2.$$

Then the amplifier noise is

$$\sigma_{amp}^2 = \sigma_{O/E}^2 - \sigma_{sI_d}^2 - \sigma_t^2 \approx 1.66 \times 10^{-11} A^2.$$

At step 5, the amplitude of the voltage signal is 20 mV. Now the part of the shot noise from the input optical power is:

$$\sigma_{sOp}^2 = 2 \times 1.6 \times 10^{-19} \times \frac{(20 - 0.8) \times 10^{-3}}{300} \times 10^9 = 2.048 \times 10^{-14} A^2.$$

We assume both oscilloscope noise and the amplifier noise do not depend on the amplitude of the signal, then the noise of the EDFA is

$$\sigma_{EDFA}^2 = \left(\frac{0.48 \times 10^{-3}}{50}\right)^2 - \sigma_{osc}^2 - \sigma_{sOp}^2 - \sigma_{sI_d}^2 - \sigma_t^2 - \sigma_{amp}^2 \approx 5.61 \times 10^{-11} A^2.$$

Table 4.4: Noise analysis results for experiment setup 1

Noise name	Symbol	Noise level
Oscilloscope build-in amplifier and ADC noise	$U_{n_{osc}}$	0.22 mV
O/E converter detector shot noise due to light signal	$U_{n_{sOp}}$	42.9 μV
O/E converter detector thermal noise	U_{n_t}	70.5 μV
O/E converter Detector shot noise due to dark current	$U_{n_{sI_d}}$	8.76 μV
O/E converter build-in amplifier	$U_{n_{amp}}$	0.2 mV
Noise from EDFA	$U_{n_{EDFA}}$	0.375 mV

Table 4.5: Noise analysis results for experiment setup 2

Noise name	Symbol	Noise level
Oscilloscope build-in amplifier and ADC nise	$U_{n_{osc}}$	0.22 mV
O/E converter detector shot noise due to light signal	$U_{n_{sOp}}$	0.51 mV
O/E converter detector thermal noise	U_{n_t}	70.5 μV
O/E converter Detector shot noise due to dark current	$U_{n_{sI_d}}$	8.76 μV
O/E converter build-in amplifier	$U_{n_{amp}}$	0.2 mV
Noise from EDFA	$U_{n_{EDFA}}$	23 mV

To make the results easier to read, the equivalent noise levels at the oscilloscope input from different noise sources are converted to voltage and listed in Table.4.4. Using the same method, the equivalent noise levels at the oscilloscope input in experiment setup 2 are also calculated and the results are listed in Table.4.5.

The above analysis indicates that the noise from the EDFA is dominant in both cases. The noise from the oscilloscope and the amplifier in the O/E converter have almost the same contributions to the total noise level. The shot noise and thermal noise of the detector in the O/E converter are negligible compared to the three high level noises. The signal to noise ratio for setup 1 is

$$SNR_1 = 20\log\left(\frac{20\times10^{-3}}{0.48\times10^{-3}}\right) \approx 32.4dB,$$

the signal to noise ratio for setup 2 is

$$SNR_2 = 20\log\left(\frac{2.75}{23\times10^{-3}}\right) \approx 41.6dB.$$

This indicates that although the total noise level of setup 2 is much higher than setup 1, the signal to noise is improved by 9.2 dB through using one additional EDFA in the experiment. The reason for the signal to noise ratio improvement is explained as follows. The signal to noise ratio is better than 41.6 dB at the input of the O/E converter before adding the second EDFA. But the noise from the O/E converter and the oscilloscope have noise levels which are comparable to the signal level at this moment. The EDFA has a better noise figure than that of the O/E converter and the oscilloscope and the signal level improvement results from adding the second EDFA reduces the percentage of the contributions from the O/E converter and the oscilloscope to the total noise level of the system. Further optimization of the experiment setup may result in even better overall signal to noise ratio.

4.5 Summary

In this chapter, the effects of various parameters such as the pulse width, pulse shape, and dispersion property of the fiber, on the accuracy, spectral resolution and spectrum acquisition speed of the HSFOS are thoroughly investigated through analytical and numerical methods. To ensure that the dispersed chromatic light pulse has a profile that could represent the spectrum of the incoming light, two requirements have to be fulfilled. One is the GVD of the fiber used in the spectrometer should not have different signs in the spectral range i.e. the β_1 of the fiber is monotonously increasing or decreasing. The other is that the modulation pulse should have a spectral width not comparable to the frequency of the light so that the shape of the light pulse has no severe distortion or destruction after broadening. To reduce the measurement error, the width of the broadened pulse should be decreased and the results should be normalized. In addition, fiber with small higher order dispersion should be chosen. To improve the spectral resolution, the combination of the initial pulse width, the amount of dispersion and the pulse shape should be properly chosen. Under certain pulse widths and dispersion values, rectangular pulses could achieve better spectral resolution and the reason is not chirp but the pulse reconstruction through harmonic superposition. Further the noise from different noise sources are analyzed based on experimental results. The dominant noise source is the EDFA. The additional EDFA used in the experiment improves the overall signal to noise ratio.

Chapter 5

Experimental Results

In this chapter, the timing method for the HSFOS is introduced at the beginning. Following that the experimental results of the proposed HSFOS are presented in two separate sections for two different types of fiber optic sensors, FP sensors and FBG sensors. The HSFOS is configured in different ways due to different fibers used to achieve the time domain dispersion. For each fiber, the dispersion property of the fiber is tested before the HSFOS is used to record the sensor spectrum. Then the signal demodulation results for corresponding sensors using the HSFOS are provided. Discussion based on the results is made at the end of each section.

5.1 Timing method in the HSFOS

Timing is the procedure through which the length of a period of time is measured or the time point when an event occurs is determined. Timing or a timing method is critical to those devices whose output or operation is related to acquisition of time information. Since the operational principle of the HSFOS is dispersing the sampled incoming light in time domain rather than spatially dispersing the incoming light signal as in conventional spectrometers

to produce the spectrum. The dispersed light signals usually have a short length in the time domain (several nanoseconds to several tens of nanoseconds) of which the occurrence time of each data point represents one specific wavelength in the spectrum of the incoming light, the timing method becomes critical for the spectrometer to generate accurate results. Especially in the third section, where the HSFOS is used to demodulate the signals from FBG sensors, the quality of timing has a direct impact on the quality of the demodulation results. Both the timing accuracy and precision should be considered. In the HSFOS, the accuracy of timing related to the fiber dispersion property measurement and the timing accuracy of the devices used in the system for the purposes of delay, signal conditioning, time measurement and data acquisition. The latter is determined only by the performances of the device. Accurate dispersion property data of the fiber can be acquired from the manufacturer or by using special dispersion measurement tools. In our experiments, the fiber dispersion measurement is conducted based on the available equipment in our laboratory. Obtaining the average of a large number of measurements e.g. average of 1000 measurements, high accuracy could be achieved. In the HSFOS, since each time point only relates to one wavelength, the timing accuracy could be improved by using a light signal with known spectrum to calibrate the results. The precision of the timing in the HSFOS is determined by the timing precision of the equipment used, which includes both the long term and short term timing stability, and the method for the signal processing. The long term timing stability is affected by the drift of the equipment and the short term timing stability is usually called timing jitter and is related to the noise in the equipment. The signal processing method is investigated in this section.

Fig.5.1 shows the block diagram of the experiment setup. A 1550 nm SLED with an output power of 1 mW is used as the light source. This setup is similar to the experiment setup for FP sensor signal demodulation except that the sensor is replaced by a cleaved fiber end so that the light of any wavelength from the light source is reflected back. The purpose of using a SLED is that the dispersed chromatic light pulse signal has the same width in time domain as the signal when a sensor is connected. This helps to decide the amount of time delay

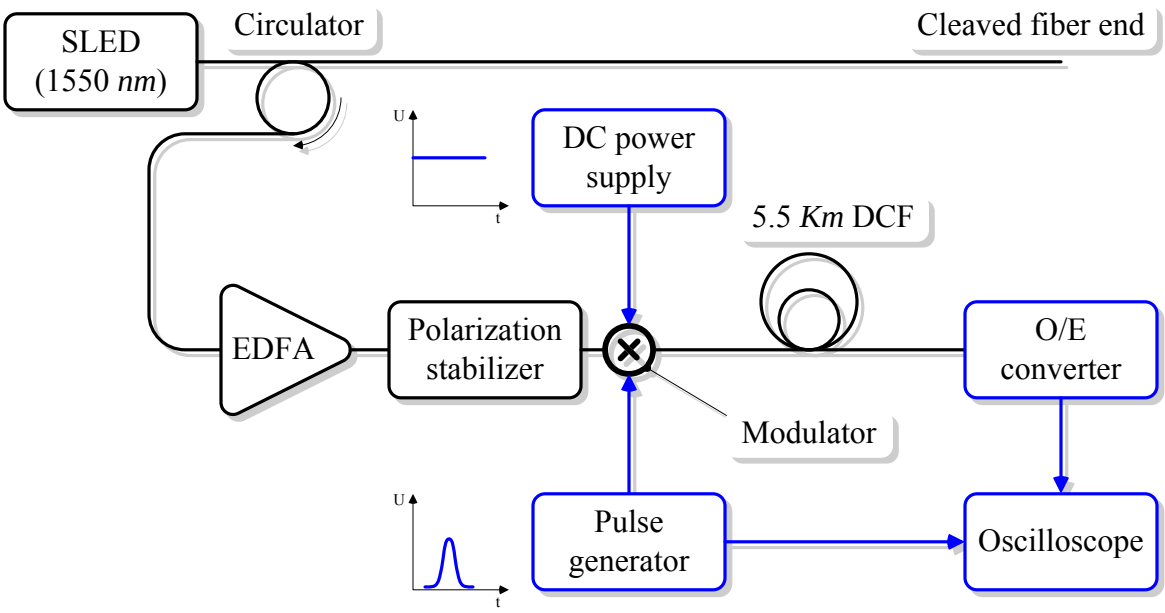

Figure 5.1: Block diagram of the experiment setup

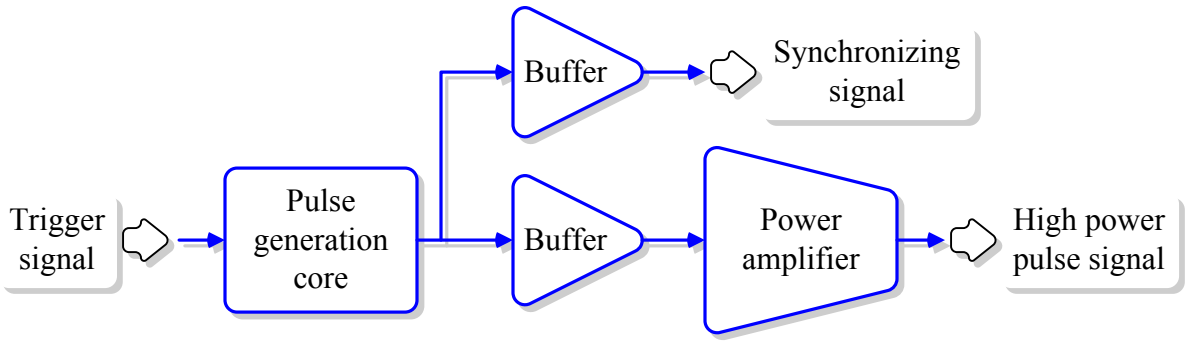

Figure 5.2: Block diagram of the pulse generator

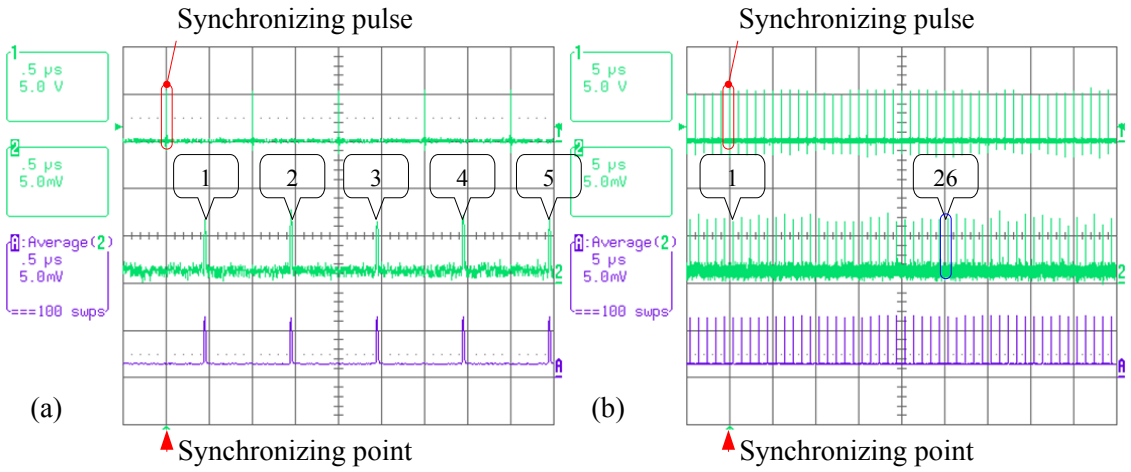

Figure 5.3: Synchronizing pulse in channel 1 and its corresponding pulse in channel 2

between the synchronizing signal and the starting point of data sampling in the oscilloscope in order that the whole dispersed light pulse signal can be recorded without any cropping. The modulator used is a JDSU 10 Gb/s modulator with an extinction ratio of 20 dB and the V_π is 6 V. The O/E converter is a HP 11982A and the oscilloscope is a Lecroy LT 342 (bandwidth: 500 MHz). In Fig.5.2, the block diagram of the pulse generator is illustrated. The generator consists of one pulse generation core, two buffers and one power amplifier. The pulse generation core outputs one low power pulse each time it is triggered by the trigger signal from a signal source. The two buffers are used to isolate the pulse generation core from the synchronizing signal output port and the power amplifier so that the performance of the circuits in the core is not affected by other circuits. The pulse generator can output narrow pulses with pulse width from 6 ns to 18 ns (T_{FWHM}). The design minimized the delay time drift, $\Delta t_{d_{pg}}$, between the synchronizing signal and high power pulse signal.

In this experiment, 6.1 ns (T_{FWHM}) light pulses are used. The trigger signal is a 1 MHz square wave at TTL logic level. Fig.5.3 presents the oscilloscope's display of the sampled signals. The signal in channel 1 is the synchronizing signal and channel 2 displays the electric signal from the O/E converter which represents the profile of the dispersed light signal. In

Fig.5.3, each synchronizing pulse in channel 1 is followed by a pulse in channel 2. Although the two pulses from different channels have the shortest distance between them in the time domain, they may not be related i.e. the pulse in channel 2 following the pulse in channel 1 may not be the corresponding pulse of that pulse in channel 1. Each time the pulse generator is triggered, it generates two pulses. One is the synchronizing pulse for the oscilloscope to synchronize the signal sampling in channel 2. The other is the high power pulse that is used to drive the modulator so that the incoming light is sampled and a light pulse (the sample of the incoming light) is formed. Then this light pulse dispersed by the dispersive fiber and the O/E converter converts the dispersed light pulse into electric pulse and sends the electric pulse to channel 2 of the oscilloscope for sampling. This pulse in channel 2 is thus defined as the corresponding pulse of that synchronizing pulse. The synchronizing pulse in channel 1 is defined as the corresponding synchronizing pulse of this pulse in channel 2. Because of the large delay introduced by the dispersive fiber, the corresponding pulse in channel 2 of each synchronizing pulse in channel 1 is usually far behind that synchronizing pulse in time domain. For the experiment setup presented in Fig.5.1, the corresponding pulse of the synchronizing pulse circled by red line is the 26th pulse behind it as shown Fig.5.3(b) (The pulse circled by blue line).

The time delay between each synchronizing pulse in channel 1 and the pulse behind it in channel 2, $t_{d_{total}}$, is the sum of the follows: the delay from the power amplifier in the pulse generator, $t_{d_{pg}}$, the delay of the modulator, t_{d_m}, the delay introduced by the dispersive fiber, $t_{d_{fiber}}$, the delay in the O/E converter, $t_{d_{O/E}}$, the delay in the oscilloscope, $t_{d_{osc}}$, and the periods of the trigger signal, $m_{pindex} \times T_{trigger}$, and can be expressed mathematically as:

$$t_{d_{total}} = t_{d_{pg}} + t_{d_m} + t_{d_{fiber}} + t_{d_{O/E}} + t_{d_{osc}} + m_{pindex} \times T_{trigger}, \tag{5.1}$$

where $T_{trigger}$ is the period of the trigger signal. The number of the periods, m_{pindex}, is determined by the index difference between the synchronizing pulse before the pulse in channel 2 and its corresponding synchronizing pulse. Only the delay between the synchronizing pulse and its corresponding pulse will not be affected by the periods of the trigger signal. The

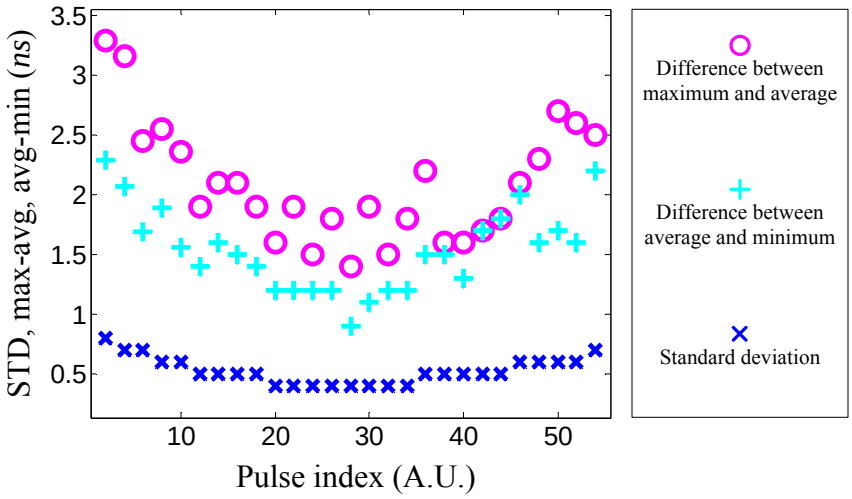

Figure 5.4: Timing jitter measurement results

time delay drift $\Delta t_{d_{total}}$ is defined as:

$$\Delta t_{d_{total}} = \Delta t_{d_{pg}} + \Delta t_{d_m} + \Delta t_{d_{O/E}} + \Delta t_{d_{osc}} + m_{pindex} \times \Delta T_{trigger}, \tag{5.2}$$

where $\Delta t_{d_{pg}}$ is the time delay drift of the power amplifier in the pulse generator; Δt_{d_m} is the time delay drift of the modulator; $\Delta t_{d_{O/E}}$ is the time delay drift of the O/E converter; $\Delta t_{d_{osc}}$ is the time delay drift of the oscilloscope; and $\Delta T_{trigger}$ is drift of period in the trigger signal. The timing jitter $\delta t_{d_{total}}$ is defined as:

$$\delta t_{d_{total}} = \sqrt{\delta t_{d_{pg}}^2 + \delta t_{d_m}^2 + \delta t_{d_{O/E}}^2 + \delta t_{d_{osc}}^2 + m_{pindex} \times \delta T_{trigger}^2}, \tag{5.3}$$

where $\delta t_{d_{pg}}$ is the timing jitter between the synchronizing signal and the high power pulse signal from the pulse generator; δt_{d_m} is the timing jitter in the modulator; $\delta t_{d_{O/E}}$ is the timing jitter introduced by the O/E converter; $\delta t_{d_{osc}}$ is the timing jitter introduced by the oscilloscope; and $\delta T_{trigger}$ is the trigger signal timing jitter in one period of the trigger signal.

From Eq.(5.2), the drift of the time delay could be reduced by using the corresponding synchronizing pulse to synchronize the sampling of the pulse in channel 2. Under this condition,

m_{pindex} equals 0. Moreover, since the drift is a slow process, using online calibration i.e. using a known spectrum to calibrate the spectrometer before each spectrum measurement will largely reduce its effects. Eq.(5.3) indicates that using the corresponding synchronizing pulse to synchronize the sampling can also reduce the timing jitter. For further reducing the timing jitter, high performance equipment with lower timing jitter should be chosen. The delay time measurement results are shown in Fig.5.4. Each data point is acquired based on 1000 measurements. The difference between average and minimum, the difference between maximum and the average and the standard deviation of the measurements are plotted in Fig.5.4. The results confirmed the above analysis about timing jitter.

5.2 HSFOS for FP sensor signal processing

5.2.1 Fiber dispersion property measurement

Since the HSFOS uses time domain dispersion instead of spatial dispersion, the dispersion property of the fiber used in the spectrometer is important for recovering the spectrum of the incoming light from the profile of the dispersed light pulse. In the HSFOS developed for FP sensor signal demodulation, a spool of 5.5 Km dispersion compensation fiber (DCF) is used. The total amount of dispersion introduced by the DCF is about 500 ps/nm around 1550 nm and the insertion loss of the fiber is 6 dB. The block diagram of the experiment setup is shown in Fig.5.5.

In the experiment setup, one tunable laser is used as the light source. The output wavelength of the laser is tuned from 1530 nm to 1570 nm with a step of 5 nm. The modulator is a JDSU 10 Gb/s modulator (extinction ratio: 20 dB, V_π: 6 V), the O/E converter is a HP11982A, and the oscilloscope is a Lecroy LT 342. For each data point, the time delay between the synchronizing pulse and its corresponding pulse from the output of the O/E converter is measured 1000 times and the result is the average of the measurement data. The results

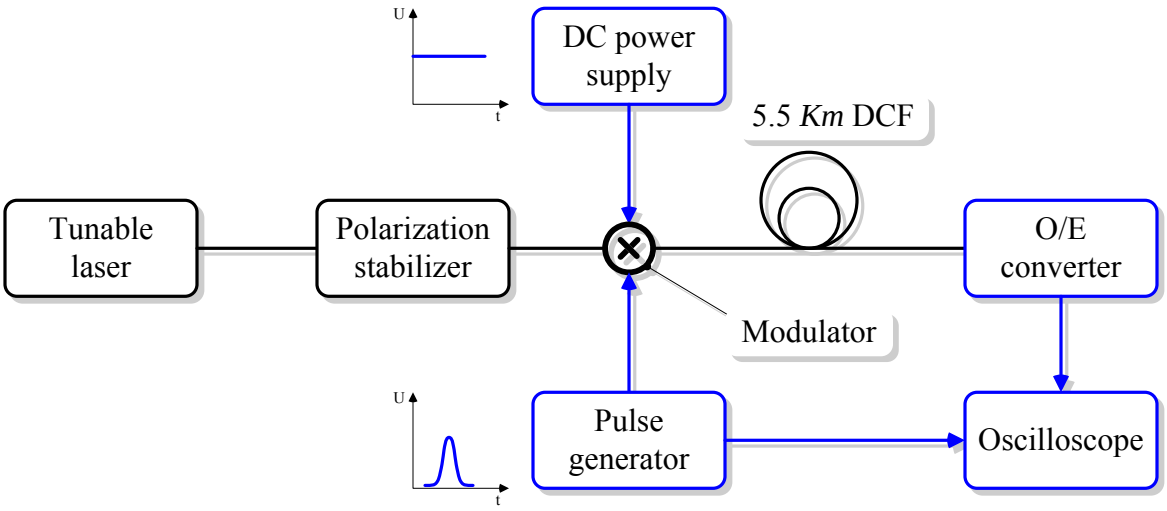

Figure 5.5: Block diagram of the experiment setup for DCF dispersion property measurement

and the processed data are provided in Fig.5.6. In Fig.5.6(a) both the experimental results and fitting results are presented. The polynomial fitting method is chosen with the highest order of 3 which corresponds to the 4th order of the propagation constant derivative in its Taylor's series. The reason for using polynomial fitting is that the propagation constant of the fiber can be expanded using Taylor's series. The results are used in the next subsection for FP sensor spectrum recovery. The first and second order derivatives of the propagation constant β_1 and β_2 are calculated based on the fitting results and are plotted in Fig.5.6(b) and (c) respectively. The dispersion property D is illustrated in Fig.5.6(d). The numerical simulations made in the next subsection use the results shown in Fig.5.6(b)(c)(d) to generate comparable results to facilitate the experimental results investigation.

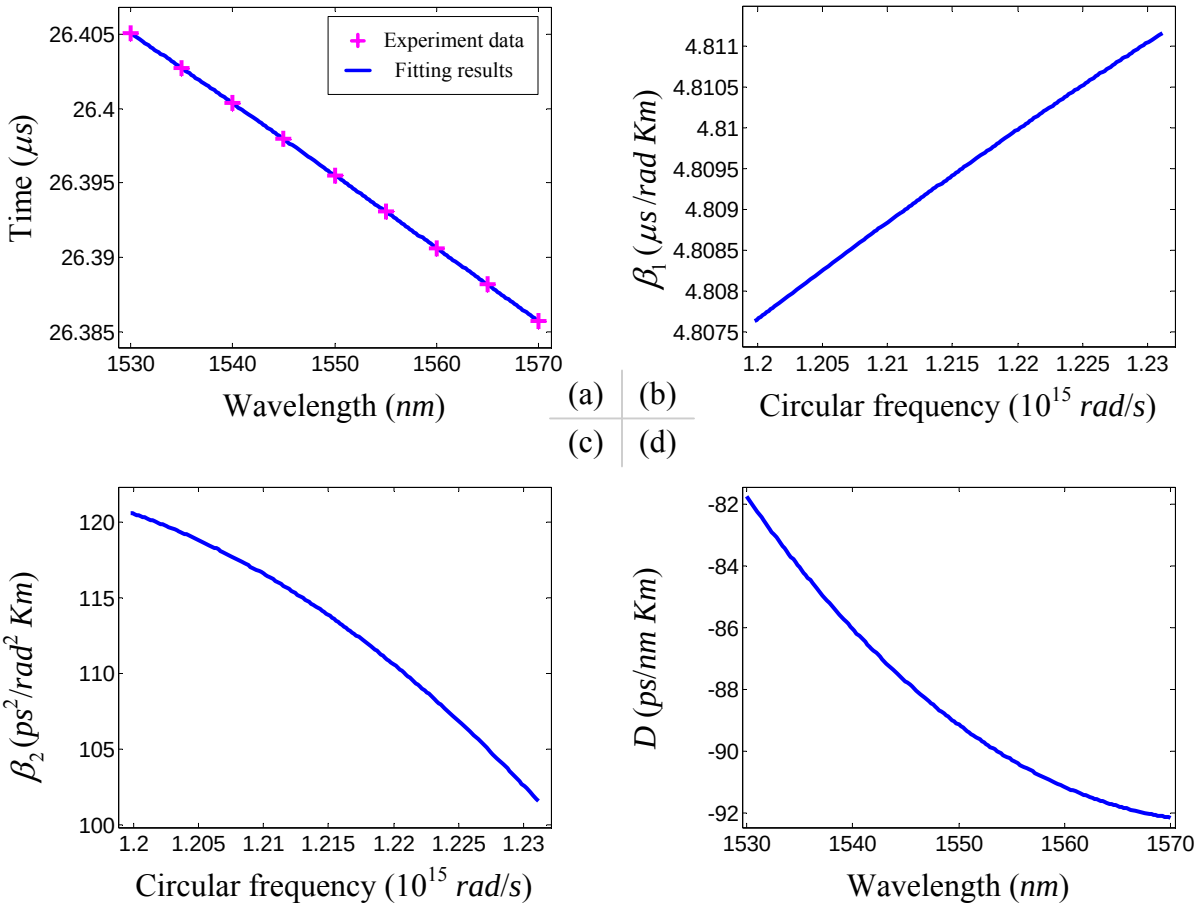

Figure 5.6: DCF dispersion property measurement results

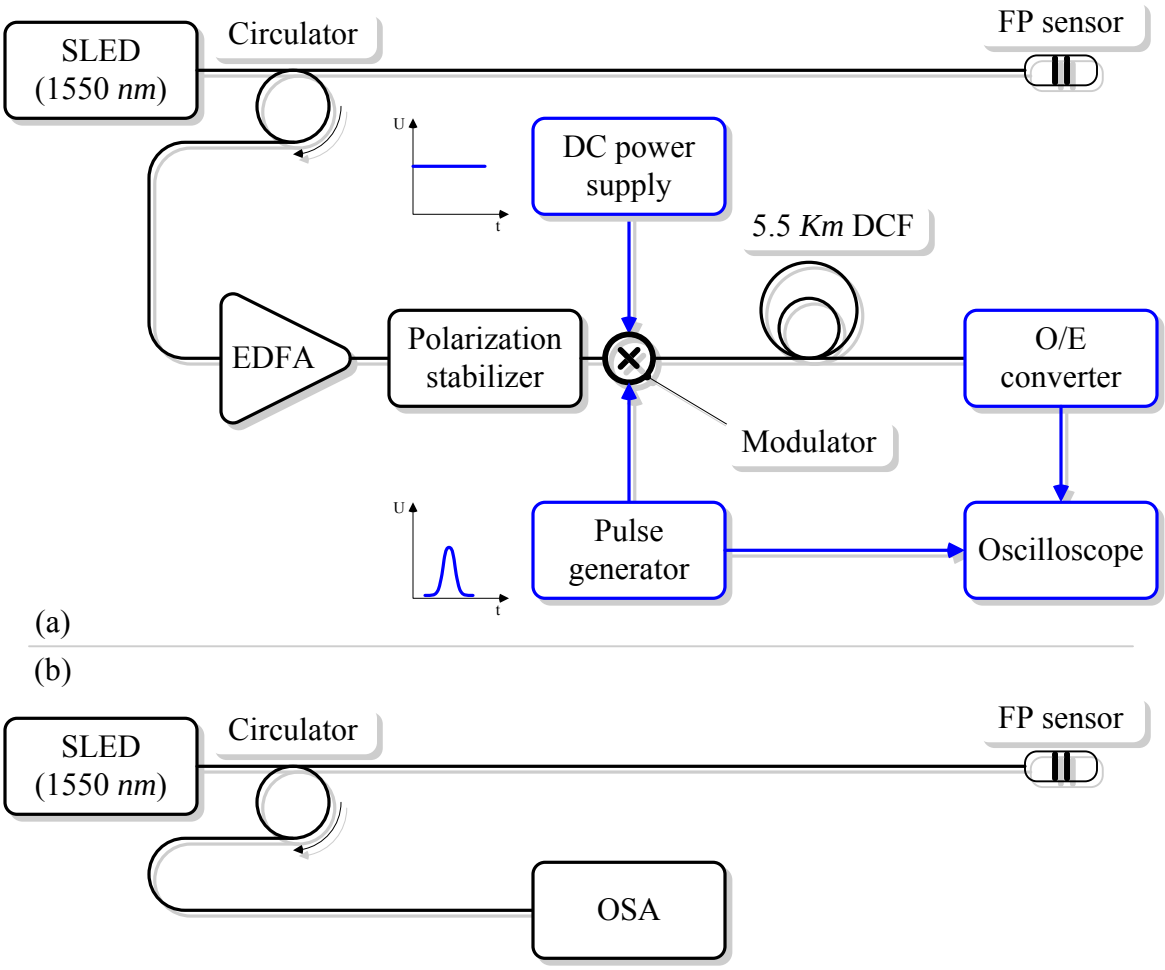

Figure 5.7: Block diagram of the HSFOS for FP sensor spectrum measurement

5.2.2 FP sensor spectrum measurement

The block diagram of the HSFOS for FP sensor spectrum measurement is given in Fig.5.7(a). In this setup, a 1 mW 1550 nm SLED is used as the wide band light source. The modulator is a JDSU 10 Gb/s modulator (extinction ratio: 20 dB, V_π: 6 V). The model of the O/E converter and the oscilloscope are HP11982 and Lecroy LT342 respectively. One EDFA is used to compensate the loss in the DCF and the polarization stabilizer. To evaluate the performance of the HSFOS, one reference system based on an OSA (ANDO AQ 6315A) is

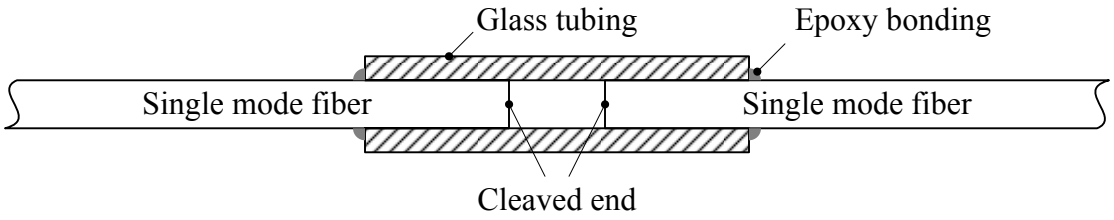

Figure 5.8: Structure of the FP sensor used in the experiment

used and the block diagram is shown in Fig.5.7(b). Two FP sensors with nominal cavity lengths of 63.326 μm (named sensor 1) and 73.812 μm (named sensor 2) are used. The sensor structure is provided in Fig.5.8. The initial width of the light pulses in the experiment is 6.1 ns (T_{FWHM}) and the repetition rate of the pulses is 1 MHz. Each measurement result is the average of 100 samples acquired by the oscilloscope. So the HSFOS in this experiment has an equivalent spectrum acquisition rate of 10000 frames of spectra per second. The fringes of the two sensors directly from the oscilloscope are plotted in Fig.5.9(a)(b). The normalized results are plotted in Fig.5.9(c)(d). The recovered spectra of the two FP sensors using the time-wavelength relationship acquired in the previous subsection are shown Fig.5.10(a)(b). For the purpose of comparison, the spectra of the two sensors measured by the reference system with two different spectral resolution settings i.e. 0.5 nm and 10 nm are provided in Fig.5.10(c)(d).

The sensor spectra recorded by OSA with 0.5 nm spectral resolution is closer to the ideal spectra of the sensors. The spectra recorded by the HSFOS are closer to that recorded by the OSA with resolution setting equals to 10 nm. The main difference between the results from the two spectrometers is that the spectra produced by the HSFOS have distortion at both ends of the spectra. The distortion is due to that the spectral width of the spectrometer is equal to the spectral measurement range. Because of the convolution nature of the spectrometer output expressed in Eq.3.30, the limited spectral width generates errors at both the upper and lower boundaries of the integration. If the spectral width has sufficient margin on both side of the spectrometer measurement range, the distortion would not be displayed

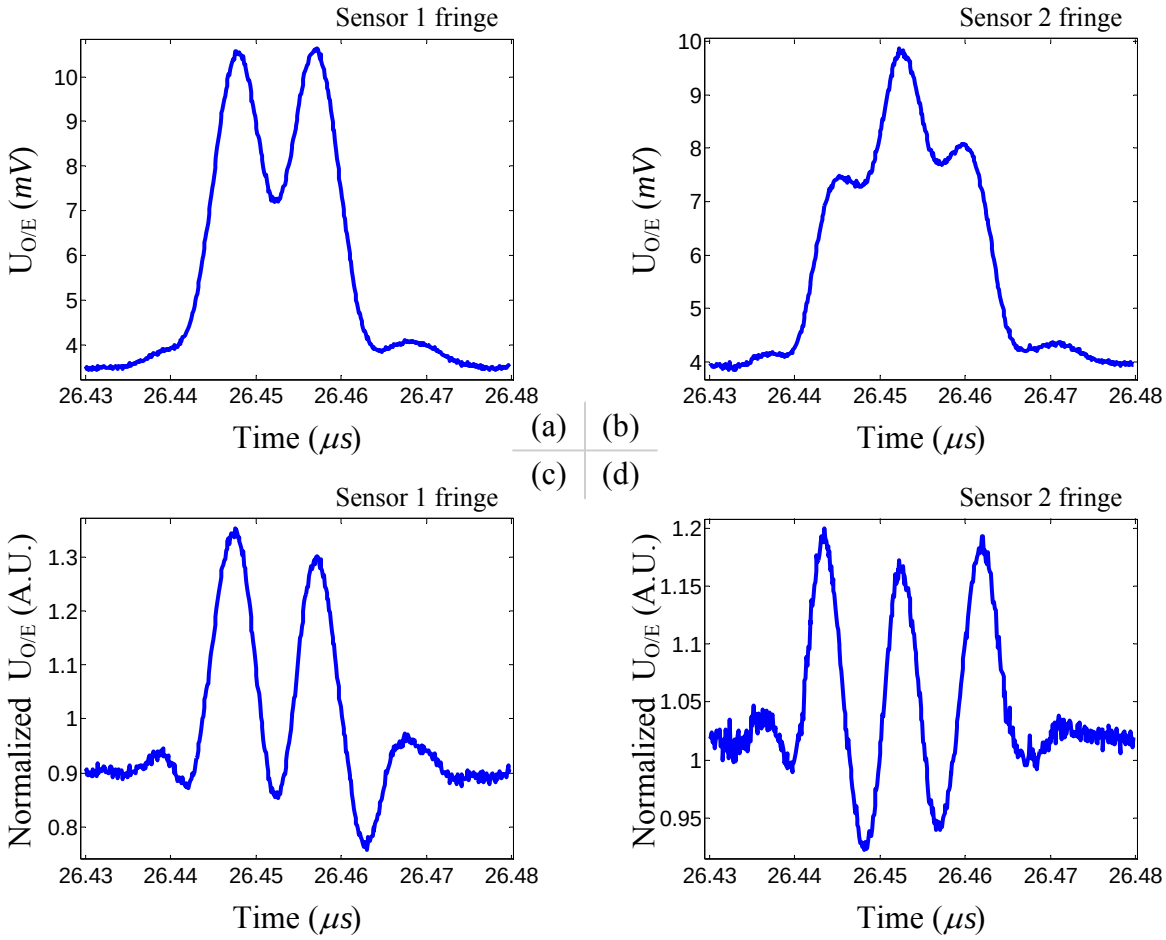

Figure 5.9: Output of O/E converter recorded by oscilloscope

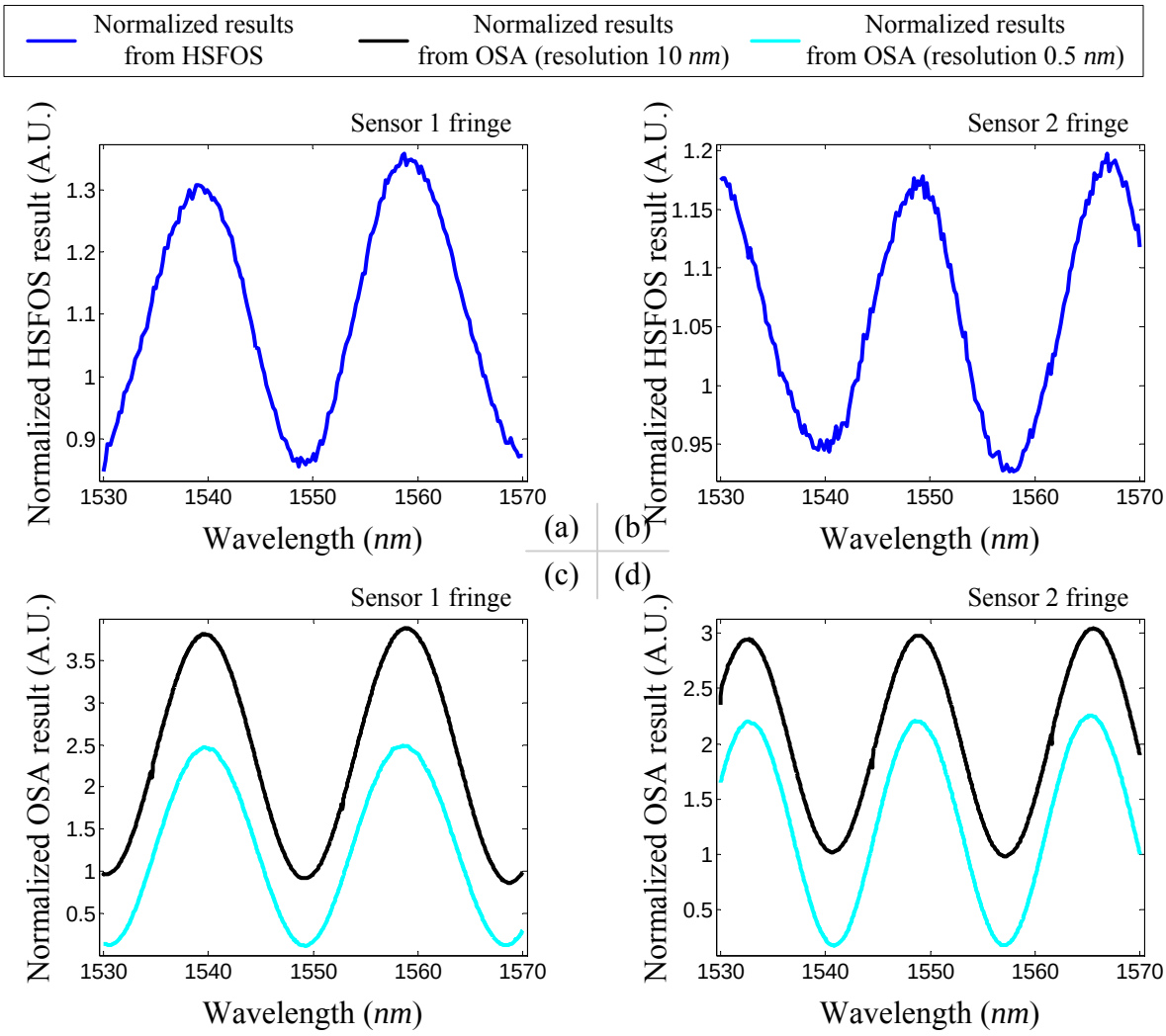

Figure 5.10: Sensor fringes spectra recorded by HSFOS and OSA

in the results. To further explain the cause of the distortion, the operational principle of the HSFOS should be discussed again. As mentioned in previous chapter, the output of the spectrometer is the superposition of both frequency dependent broadened and delayed monochromatic light pulses centered in the spectral width of the spectrometer. This can be expressed using Fig.5.11. In this figure, the blue line represents output from the spectrometer under the condition when the spectral width of the spectrometer is much greater than the measurement range; the red line corresponds to the situation when the spectral width is equal to the measurement range. The monochromatic light pulses centered in the spectral measurement range are drawn using dark gray lines. The pulses centered outside the measurement range but still in the spectral width of the spectrometer are drawn using light gray lines. When the spectral width is much greater than the measurement range, all the light pulses will together form the output for not only the part within the measurement range but also the part outside the measurement range. No distortion occurs within the measurement range. When the spectral width is equal to the measurement range, the part of output within the measurement is changed. The contributions to the output within the measurement range from those light pulses centered outside measurement range no longer exist. This results in the distortion on both ends of the output. Normalization can not correct the error caused by this distortion. The results displayed in Fig.5.10 indicates this. To confirm the above analysis, numerical simulations using rectangular modulation pulses ($C_L = C_R = 0.33$) with 7.07 ns (T_{A0}) pulse width which corresponds to 6.1 nm (T_{FWHM}) light pulse and the fiber dispersion property from the measurement made in previous subsection for the DCF are conducted. The results for the two FP sensors are presented in Fig.5.12.

The red lines in Fig.5.12 show the situation when the spectral width equals to the measurement range. The distortion in the simulation results has exactly the same characteristics as that of results from the experiment. For sensor 1 fringe, the two valleys at both ends of the spectra disappear; for sensor 2 fringe, the first peak to the left disappears and the first peak to the right shifts to right. Moreover, in the results from both the experiment and the

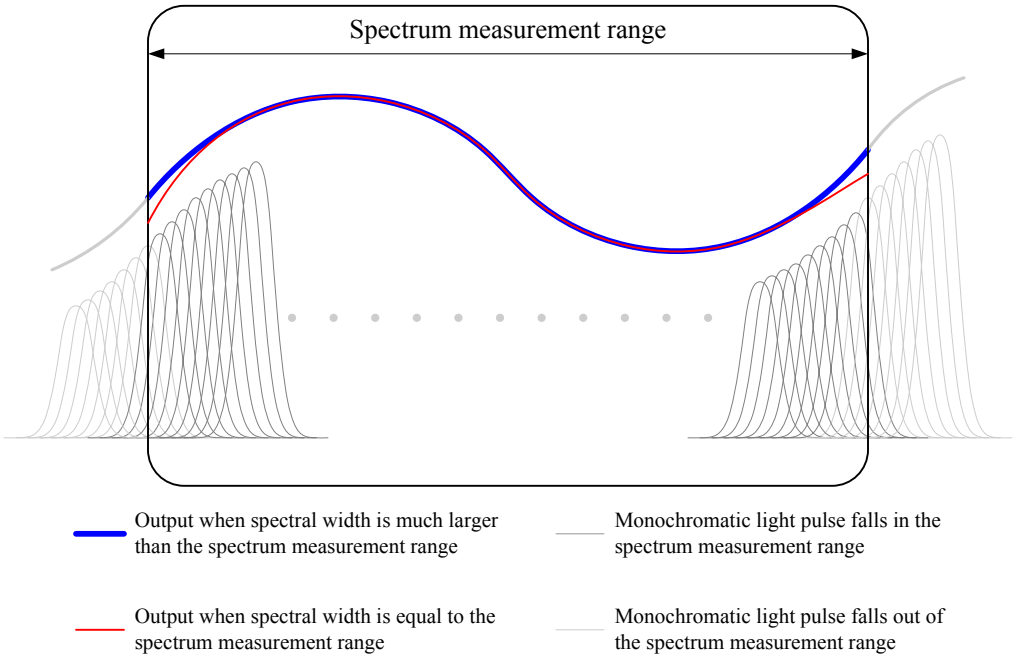

Figure 5.11: Formation of the HSFOS output

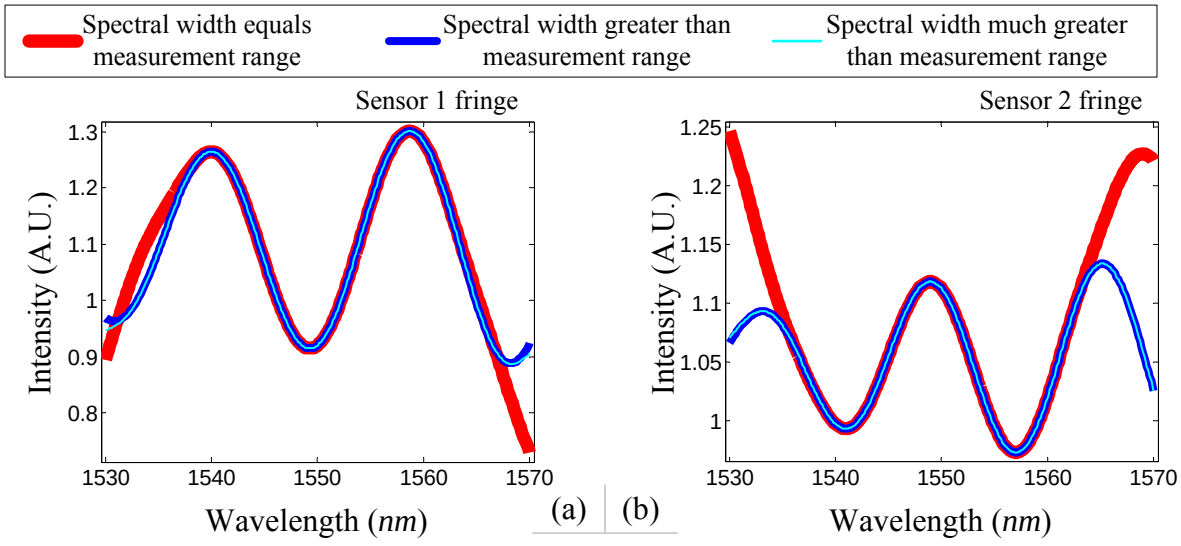

Figure 5.12: Simulation results of the sensor spectra

simulation, the distorted fringe curves have similar shapes at both ends of the measurement range. The simulation results plotted in light blue lines show the situation when there is a margin on both ends of the the measurement range. The width of the margin is determined as follows. First, the half widths T_0' of the broadened pulses at the wavelengths equal to either end of the measurement range are estimated. Then wavelength ranges corresponding to those T_0' at both ends of the measurement range are calculated using the dispersion at corresponding wavelengths. These are the margin used for the simulations mentioned above. The margin calculated in this way is the smallest one for canceling the distortion. The results plotted using dark blue lines in Fig.5.12 present the situation when the size of the margin is much greater than the smallest value. All these results prove that the analysis about the distortion at both ends of the spectra is correct.

Another type of distortion in the results shown in Fig.5.10 is that in each sensor fringe the depths of the valleys are not equal and the heights of the peaks are not the same. Under the 10 nm resolution setting, the results from the OSA also have similar distortion. Whereas in each sensor fringe recorded by the OSA with better resolution, the valleys have the same depth and the peaks have the same height. This type of distortion is caused by the operational principle of the spectrometer due to their convolution nature. The distortion is actually the first type error analyzed in the previous chapter. Moreover, for a FP sensor fringe, the widths of valleys and peaks vary with wavelength. At short wavelengths, the widths are smaller. If the spectrometer has constant spectral resolution in the whole measurement range and the value of the resolution is comparable to the widths of those valleys and peaks, the valleys and peaks will be blurred more at shorter wavelengths. For a real spectrometer, its resolution is not constant but a function of wavelength which is determined by the property of the dispersion element. The calculated spectral resolutions of the HSFOS at different wavelengths using two different pulse widths are plotted in Fig.5.13. The second pulse width corresponds to 0.5 nm resolution at 1550 nm.

Fig.5.13 tells us the resolution of the HSFOS becomes worse at shorter wavelengths for both pulse widths with the DCF used in the experiment. This makes the distortion more severe

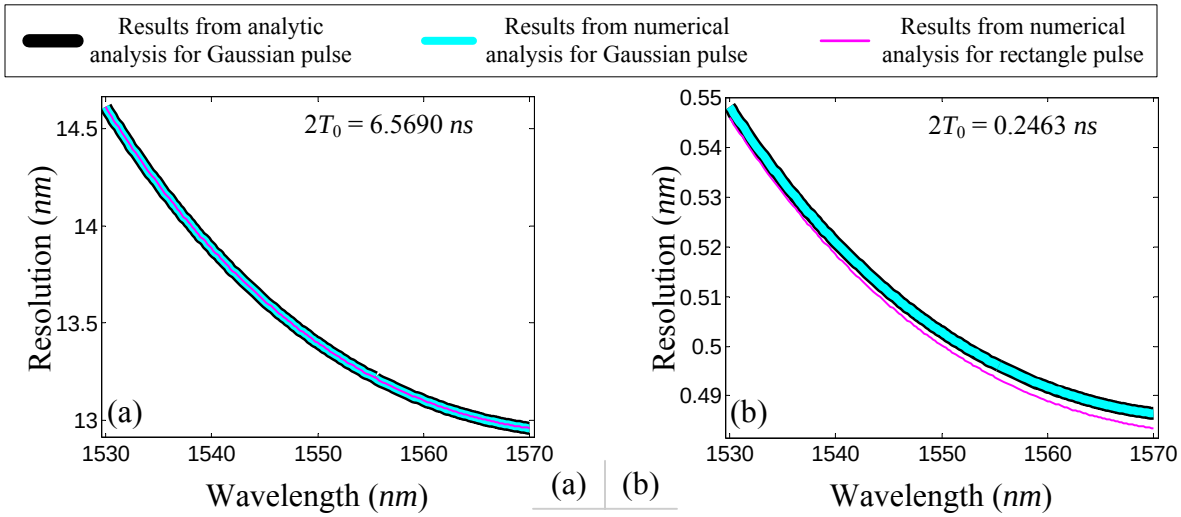

Figure 5.13: Wavelength dependence of spectral resolution

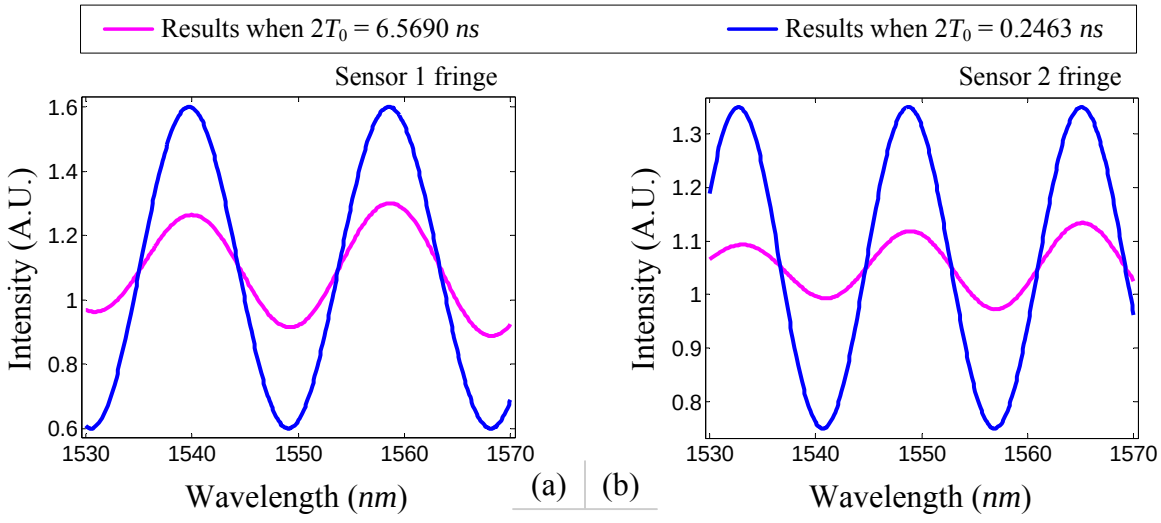

Figure 5.14: Simulation results of two FP sensor spectra under different resolutions

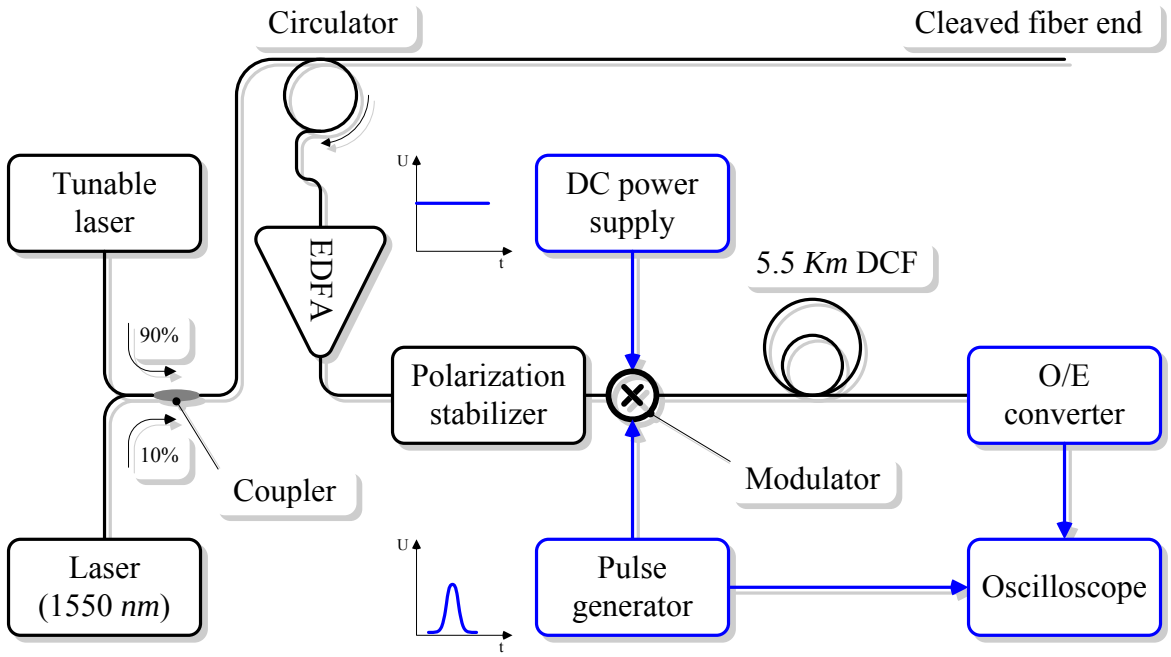

Figure 5.15: Experiment setup for resolution test

at these wavelengths. To reduce this distortion, the resolution of the spectrometer should not be comparable to the widths of the valleys and peaks in the spectrum. The simulation results of FP sensor spectra using different pulse widths are presented in Fig.5.14 which confirm the above analysis. The valleys and peaks have the same depths and heights in the results when the spectral resolution is 0.5 nm.

The resolution test for the HSFOS is also conducted experimentally. The experiment setup is presented in Fig.5.15. In the setup, two lasers, one tunable laser and one 1550 nm laser, are used as the light sources. The experimental results are provided in Fig.5.16 and 5.17 with the simulation results using a pulse with similar characteristics ($T_{FWHM} = 6.1\ ns$, $C_L = C_R = 0.33$) and the dispersion property of the DCF. As illustrated in Fig.5.13, the HSFOS should have a resolution of 13.4 nm at 1550 nm. However the resolution tests show that the real resolution is 15 nm at 1550 nm. In the results shown in Fig.5.16(a) and (c), the HSFOS can resolve two light signals with wavelength difference of 14 nm. But the two

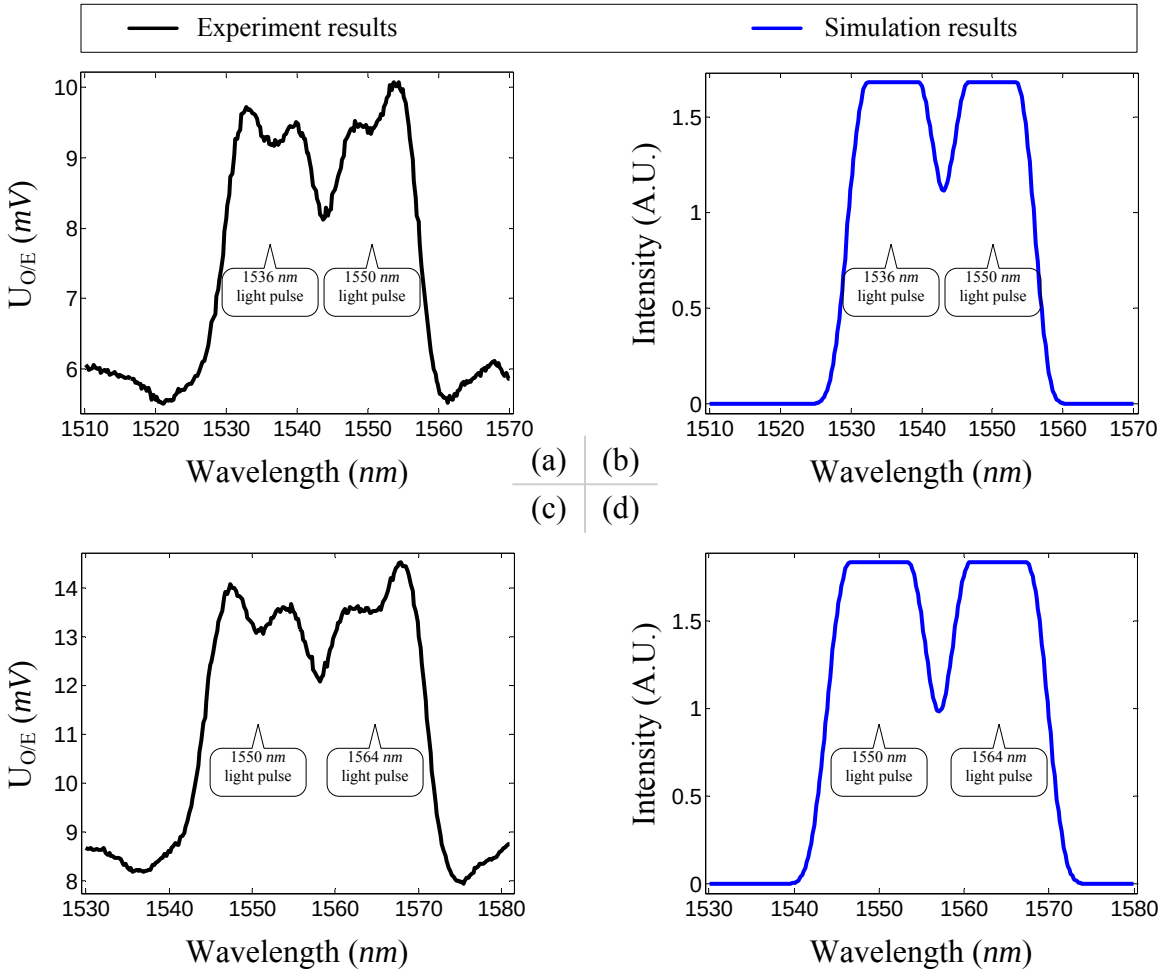

Figure 5.16: Resolution test results

light signal are almost merged together. To make the results more reliable, the resolution is determined to be 15 nm. The difference is caused by the distortion in the pulse shape introduced by the EDFA. In Fig.5.16 and 5.17, when the two pulses which represent two light signals with different wavelengths get closer, the distortion becomes more severe. This makes the valley between the two pulses flat which ultimately results in worse resolution.

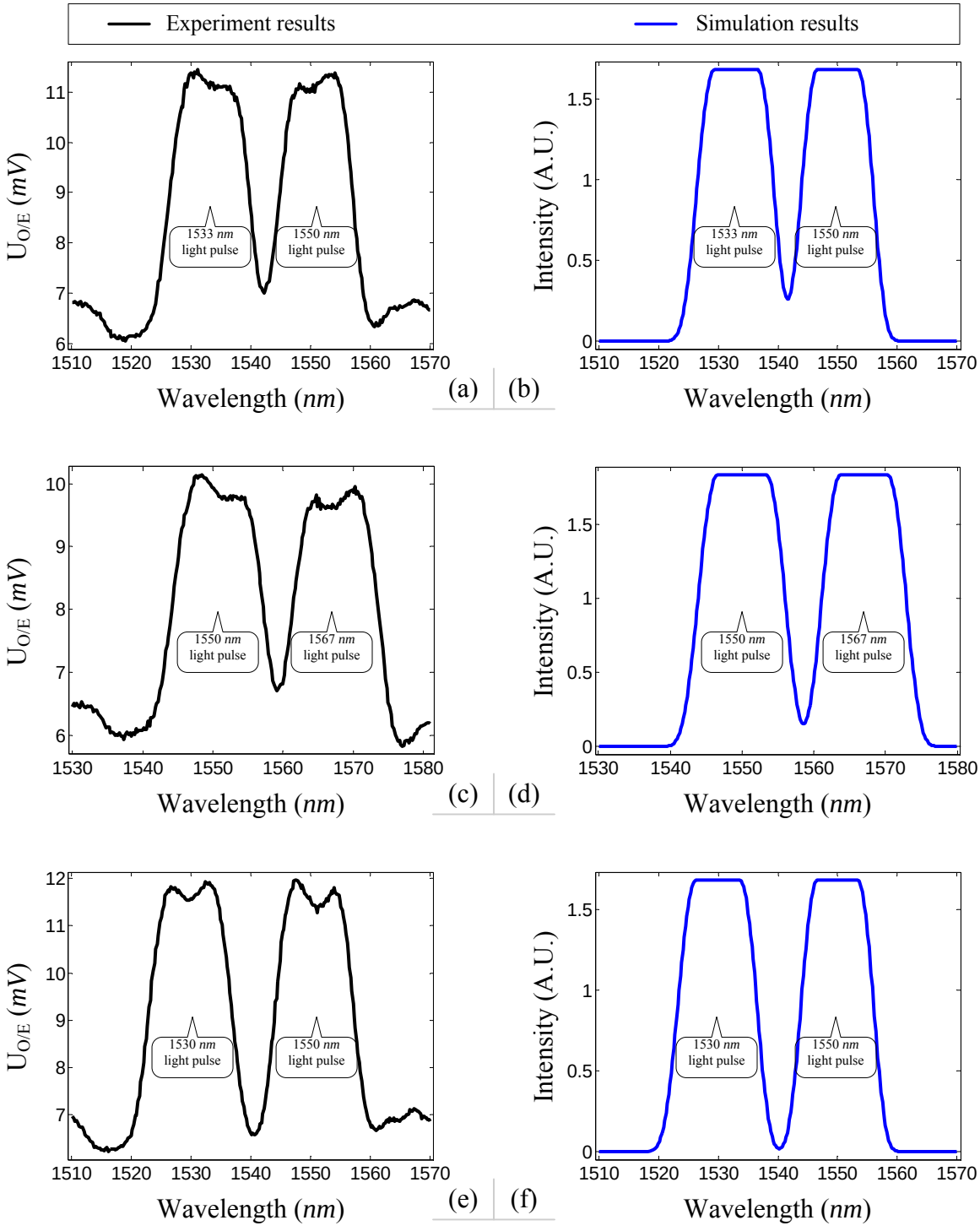

Figure 5.17: Resolution test results (continued)

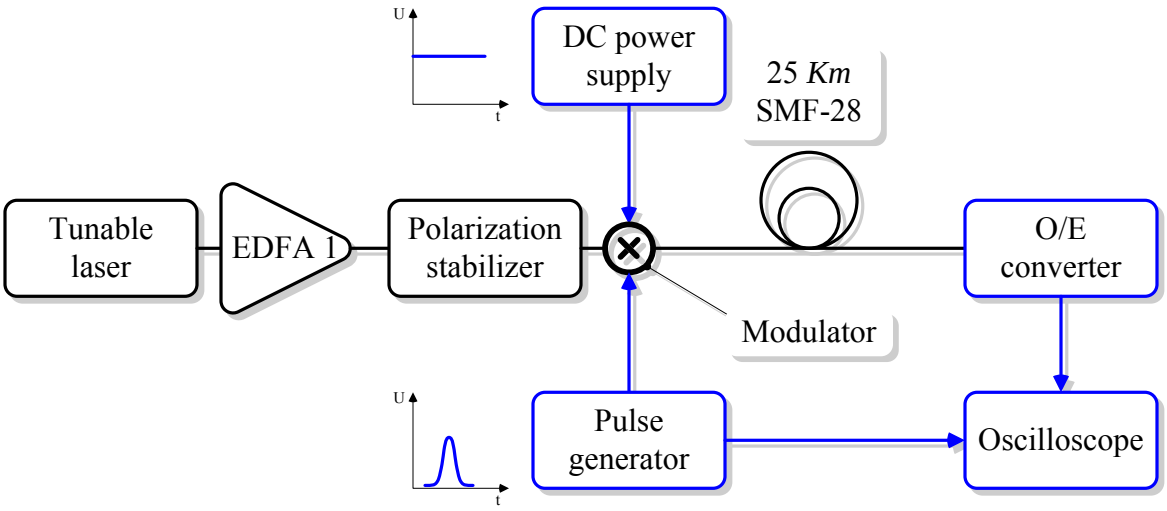

Figure 5.18: Block diagram of the experiment setup for SMF-28 dispersion property measurement

5.3 HSFOS for FBG sensor signal processing

5.3.1 Fiber dispersion property measurement

In this section, another HSFOS is configured for FBG sensor signal processing using standard single mode fiber (SMF-28). To test the dispersion property, 25 Km fiber is used which can provide about 425 ps/nm dispersion and introduces 5 dB insertion loss. The block diagram of the test setup is shown in Fig.5.18. One tunable laser is used as the light source in the experiment. In the experiment, the wavelength is tuned from 1530 nm to 1568 nm with a step of 2 nm. The modulator used in the setup is a JDSU 10 Gb/s modulator (extinction ratio: 20 dB, V_π: 6 V). The O/E converter is a HP 11982A and the oscilloscope is a Lecroy LC 574A. Because the delay introduced by the 25 Km fiber is about 121 μs which is much larger than the delay that the oscilloscope can generate under high timing resolution setting, the delay measured is not between the synchronizing pulse and its corresponding pulse from the O/E converter. Instead, the delay between the synchronizing pulse and the first pulse

following it from the O/E converter is measured. This causes higher timing jitter in the measurement results which directly increases the standard deviation. Moreover, the first derivative of the propagation β_1 can not be acquired directly from the results. The value for β_1 is an estimated value. But the GVD can still be determined directly from the results because there is only a constant difference between the two delays, i.e. the delay between the synchronizing pulse and its corresponding pulse from the output of the O/E converter and the delay between the synchronizing pulse and the first pulse following it from the output of the O/E converter. A constant has no effects on the derivative of the results. The result of each data point is based on 1000 measurements. The results and the processed data are provided in Fig.5.19. In Fig.5.19(a) both the experimental results and fitting results are presented. The fitting method is 3-order polynomial fitting. The first and second order derivatives of the propagation constant β_1 and β_2 are calculated based on the fitting results and are plotted in Fig.5.19(b)(c) respectively. The dispersion property D is illustrated in Fig.5.19(d).

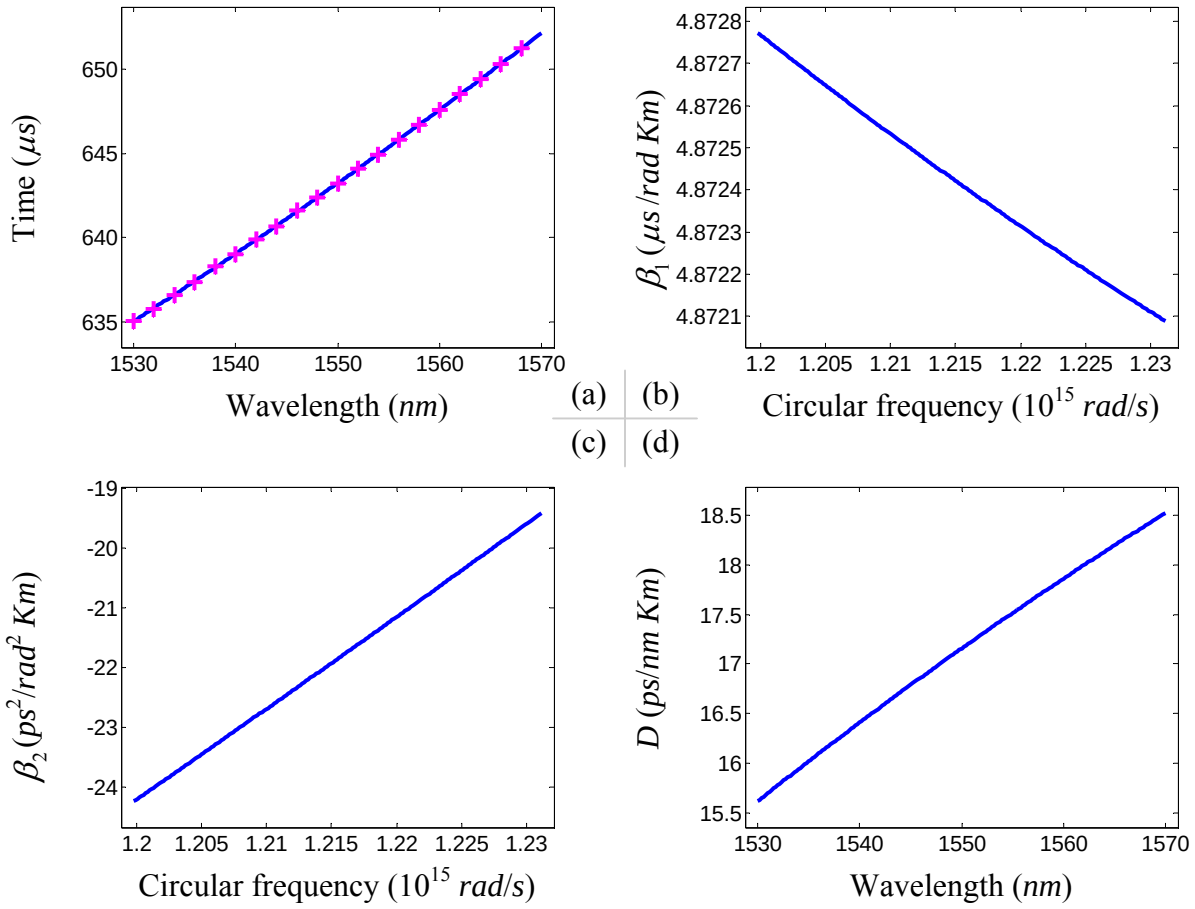

Figure 5.19: SMF-28 dispersion property measurement results

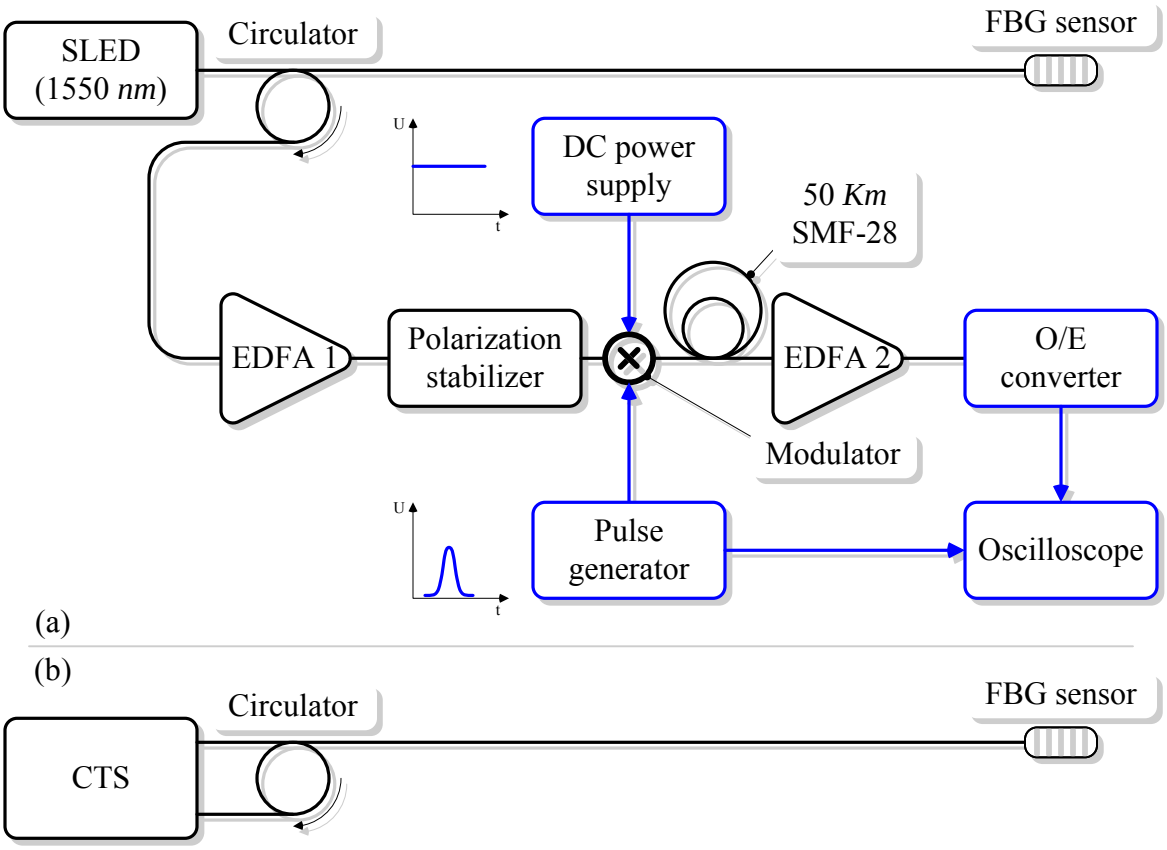

Figure 5.20: Block diagram of the HSFOS for FBG sensor spectrum measurement

5.3.2 FBG sensor signal processing

In order to get better results for sensor signal demodulation, a higher dispersion value is needed in the experiment. The block diagram of the experiment setup is shown in Fig.5.20(a). 50 Km SMF-28 fiber are used in the experiment. In the setup, the 1550 nm SLED acts as the broad band light source. In addition, one JDSU 10 Gb/s modulator (extinction ratio: 20 dB, V_π: 6 V), one HP11982A O/E converter and one Lecroy LC574A oscilloscope are used. The pulse width from the pulse generator is 6.1 ns (T_{FWHM}). The repetition rate is 1 MHz. The oscilloscope is set to do continuous average and each result is the mean of 32 measurements. The equivalent spectrum acquisition rate is 30000 frames per second.

To evaluate the performance of the system, a reference system is used which is based on a component test system (CTS, Micron Optics Si 720) as shown in Fig.5.20(b).

In applications of FBG sensors, measurands affect the grating constant of the sensor which results in reflection peak wavelength shift. FBG sensors produce a reflection light signal with narrow spectral width e.g. 0.1 nm. To demodulate the signals from a FBG sensor, usually a high resolution spectrometer is needed which should have the spectral resolution adequate to resolve the reflection peak in the sensor spectrum. Among the commercially available spectrometers, the best spectral resolution is normally down to 0.01 nm. However high resolution is usually not necessary because the measurand only relates to the position of the peak not the shape of the peak. So a spectrometer with the capability of accurately positioning the peak is enough. Moreover, spectrometers with higher spectral resolution are costly. A HSFOS having this kind of high resolution could even cost more. In this section a new method using a low resolution HSFOS to demodulate FBG sensor signal is presented through over sampling the signal from the O/E converter.

In order to get a clear view of the principle of the method, the difference between two concepts, spectral resolution and spectral positioning resolution, should first be clarified. The spectral resolution is used to describe the ability of a spectrometer to distinguish two adjacent peaks of two spectral components with the same intensity but different wavelengths in one spectrum. The spectral positioning resolution is a measure of a spectrometer's capability to positioning certain spectral component in a spectrum. For the FBG sensor signal demodulation, the most important thing is to achieve a high spectral positioning resolution which is critical for the accuracy of the demodulation rather than high spectral resolution which can provide a clear view of the reflection peak. In most spectrometers, the value of the spectral resolution and the spectral position resolution are highly related or even equal. However in the new spectrometer the spectral positioning resolution can be much higher than the spectral resolution. As shown in Fig.5.21(b), the signal from the O/E converter (shown in Fig.5.21(a)) is sampled by the DAQ or oscilloscope. The pink samples of the signal have a sample rate more than twice the highest harmonics in the signal. According

to the sampling theorem, under ideal conditions, the signal can be recovered from these samples without any information loss. If the blue samples are added, the fidelity of the sampled signal may not be improved. In reality, the amplitude resolution of an DAQ is a finite number which is determined by the bits of the ADC. More samples do provide more information which can improve the fidelity of the sampled signal. Higher sample rate also helps to positioning the signal with higher resolution and accuracy. One simple example is shown in Fig.5.21(c) and (d). In Fig.5.21(c) the leading edge of a pulse is sampled by a DAQ with only one bit amplitude resolution. It is obvious that under this circumstance the higher the sample rate the more accurately the edge can be located. Normally the DAQ will have more than 1 bit resolution, the amplitude information combined with the high sample rate will further improve the positioning resolution. In Fig.5.21(d), a DAQ with 2 bits resolution and the same sample rate can achieve a positioning resolution that is 3 times that the DAQ in Fig.5.21(c) achieves. For a real DAQ, the amplitude resolution is at least 8 bits which will have a positioning resolution 254 times higher than that of the 1 bit DAQ if the same sample rate is used and the amplitude of the signal fill the whole amplitude measurement range of the DAQ. This is the best results the 8 bits DAQ can get. Due to the lower amplitude of the signal and the noise, the effective bits of 8 bits DAQ may only be 4 to 6 bits. The positioning resolution improvement comparing to the 1 bit DAQ is 14 to 62 times. So if the sample rate is 2 GS/s and the number of the effective bits is 6, the highest positioning resolution in time domain is 8 ps.

In the experiment, a FBG strain sensor is used. The wavelength of the reflection peak is measured using the reference system illustrated in Fig.5.20(b). The positions of the corresponding light pulse in time domain is measured by the HSFOS. The sample rate of the DAQ (the oscilloscope) is 2 GS/s and the amplitude resolution is 8 bits. The strain is applied so that the wavelength of the reflection peak varies from 1541.50 nm to 1542.05 nm with a step of 0.05 nm. The experimental results are plotted in Fig.5.22. Each data point is the average of 100 measurements. The results clearly indicates that the HSFOS can achieve a spectral positioning resolution of 0.05 nm which is already enough for many FBG sensor applications.

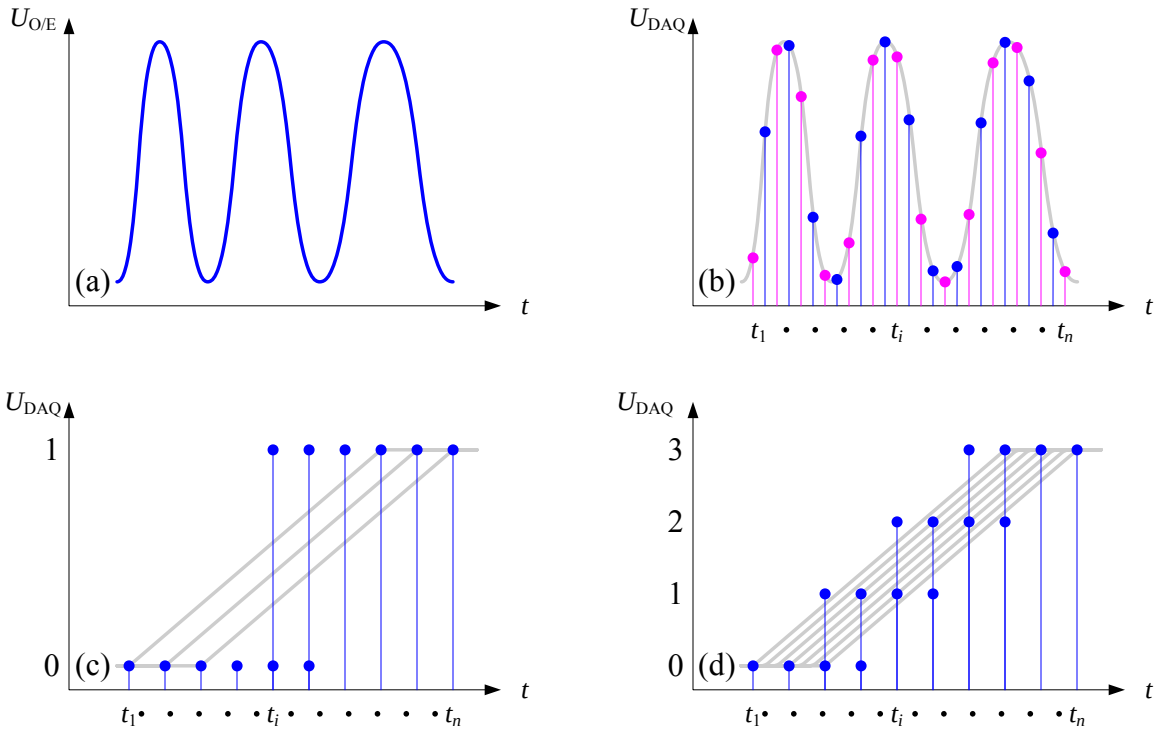

Figure 5.21: Over sampling of the signal

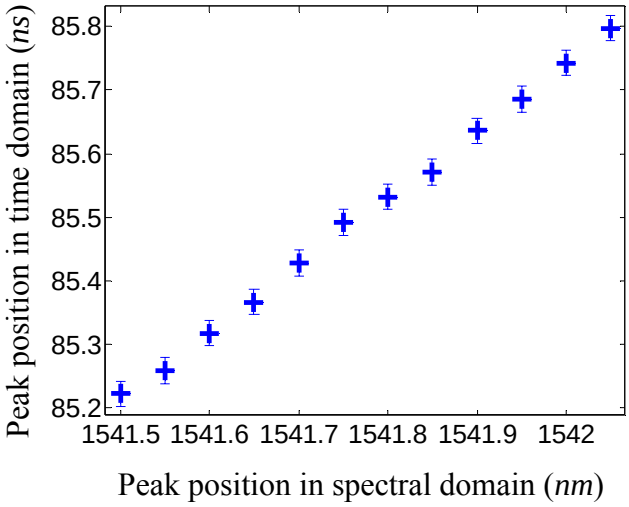

Figure 5.22: Experimental results of HSFOS for FBG strain sensor

5.4 Summary

In this chapter, the timing method of the HSFOS is discussed. Sampling the corresponding pulse of each synchronizing pulse could cancel the effects from the trigger signal on the drift and timing jitter of the system. To further improve the timing performance of the system, higher performance equipment is required. In the second section, the experiment setup for FP sensors signal demodulation is given and the spectra from two FP sensors with different cavity lengths acquired by the HSFOS are provided. Distortion in the output of the HSFOS is investigated. In addition, the spectral resolution of the HSFOS is tested. A 15 nm resolution is achieved by the setup. Numerical simulations based on the mathematical model developed in the previous chapter are made and compared with the experimental results. Both the experiment and simulation results support the conclusion presented as follows: To reduce the distortion at both ends of the spectrum, the spectral width of the spectrometer should be larger than the measurement range and sufficient margin should be made on both ends of the measurement range. To reduce the spectral resolution induced distortion, the value of the resolution should not be comparable to the narrowest valley or peak in the spectrum. At last, the method of using the low spectral resolution HSFOS to demodulate the FBG sensor signal is presented. The experiment result indicates that the HSFOS used in the experiment can achieve a 0.05 nm spectral positioning resolution which makes it capable for FBG sensor signal processing.

Chapter 6

Summary and future work

A high speed fiber optic spectrometer for fiber optic sensor signal processing is proposed and demonstrated in this dissertation. The operational principle for the novel spectrometer is presented through both graphical and mathematical descriptions. Systematic analysis of major system parameters based on a developed mathematical model and experimental results is conducted. Preliminary signal demodulation results for both FP interferometric and FBG sensors are demonstrated.

6.1 Summary of the current work

6.1.1 Summary and conclusions

Fiber optic sensors are demanded by more applications in recent years, but the low speed of the current white light interferometry and the small dynamic range and ambiguity from the existing quadrature phase detection demodulation places a barrier to the intrinsically high capable sensors. The HSFOS proposed has the capability to achieve at least 1 million frames of spectra per second through time domain sampling and dispersing the incoming light together with high speed data acquisition. The white light interferometry with the

HSFOS can maintain the merits of the absolute measurement nature of high accuracy and large dynamic range while obtaining the high acquisition speed.

The mathematical model developed is based on Marcuse's previous work but derived in a different way. In the previous work, researchers usually expand the propagation constant at the center circular frequency ω_0 of the whole chromatic light pulse. This results in complex analytical results and the physical picture of the light pulse evolution is not clear. In these analytical results, the Taylor's series of the propagation constant must be truncated to the third or fourth order so that the derivation of the profile of the dispersed chromatic light pulse could be made. For numerical analysis, the computation tasks are thus heavy. In the newly developed model, the Taylor's series is expanded at unfixed points, i.e. the center circular frequency of each monochromatic light pulse ω' rather than ω_0 so that the profile of the dispersed chromatic light pulse can be derived without any approximation in the propagation constant. Moreover, a clearer physical picture of the light pulse dispersion is formed. The profile of the dispersed chromatic light pulse could be treated as the superposition of all the frequency dependent delayed and broadened monochromatic light pulses. Thus the output of the spectrometer is expressed in the form of LTV system output and can be analyzed through the well established linear system theory. In addition, one approximate model in the form of the LTI system is derived from the accurate model under the assumption that all the monochromatic pulses are uniformly broadened which provides a simpler mathematical expression and physical picture. Further, the new model simplifies the programming for the numerical simulation and largely reduces the computation tasks especially through using the approximate model.

The performance analysis is conducted in four aspects: accuracy, resolution, speed and noise. The accuracy is evaluated using the mathematical model. Two types of errors affecting the accuracy are investigated. Numerical simulation results are provided to support the conclusions. The first type of error is due to the operational principle of the spectrometer. Normalization could help to reduce the error but not to totally cancel it. The error in the normalized results can be dramatically reduced when the widths of the broadened monochro-

matic pulses are no longer comparable to the narrowest valley or peak in the spectrum. The second type of error is from the approximation made for the simplified model. When the initial light pulse width is narrow or large higher order dispersion exists, the broadening of the monochromatic light pulses is more frequency dependent. The difference of the light pulse broadening at different frequency is no longer negligible. To reduce this error, fiber with smaller higher order dispersion is preferred. If the spectral resolution requirement can be met, a wider pulse width and a lower dispersion are preferred. The analysis of the spectral resolution is through both analytical and numerical methods. Different pulse shapes and widths are used. For each fixed dispersion value, one optimal initial pulse width exists which can realize the best resolution. Rectangular modulation pulses with sharper edges achieve the best resolution which is half the value from Gaussian pulses with the same initial pulse width. This is due to the special spectral structure of the rectangular pulse. After a certain amount of dispersion, the reconstruction of the pulse through the superposition of the harmonics form a pulse with pulse width narrower than its initial value. It should be noted that this is not the effect of chirp. The speed analysis is simplified by assuming that the pulse is Gaussian and the Taylor's series of the propagation constant is truncated to the second order. The results indicate that there are tradeoffs between the speed and the spectral width of the spectrometer and between the speed and the resolution. However when spectral width is 100 nm and the resolution is 0.03 nm, theoretically a 1 million frames per second acquisition speed can still be achieved. The noise analysis is done using the experimental results. Although the EDFA is the dominant noise source, the introduction of the second EDFA in the setup still improve the overall signal to noise ratio by 9.2 dB. This is so because the contributions from the O/E converter and the oscilloscope are largely reduced. They are two main noise sources before adding the second EDFA.

The experimental results demonstrate the capability of the HSFOS for FP interferometric and FBG sensor signal demodulation. For FP sensors, the HSFOS could record FP sensor fringe at an equivalent speed of 10000 frames per second with the quality close to the one from the OSA when the resolution setting of the OSA is 10 nm. The spectral resolution

of the HSFOS in the experiment is 15 nm. For FBG sensors, a new signal demodulation method using the low spectral resolution HSFOS is presented. By doing over sampling of the dispersed FBG sensor light signal, the spectral positioning resolution of the HSFOS becomes much higher than its spectral resolution so that the position of the reflection peak of a FBG sensor can be accurately determined. In the experiment, the HSFOS can resolve a change of 0.05 nm in the spectral position of the FBG sensor reflection peak at an equivalent speed of 30000 frames per second. In contrast, the traditional spectrometers typically have a speed of less than 100 frames spectra per second. In summary, the experiments have clearly demonstrated the feasibility of the HSFOS for fiber optic sensor high speed signal processing.

6.1.2 Major contributions

The major contributions of this dissertation are as below

- For the first time a high speed fiber optic spectrometer for high speed fiber sensor signal processing are proposed and its feasibility is experimentally demonstrated.
- A mathematical model is derived through expanding the propagation constant at the center circular frequency of each monochromatic pulse and no truncation of the Taylor's series of the propagation constant is made in the derivation. The result from the model is presented in the form of a LTV system output. The model provides an easier and more accurate way for both analytical and numerical analysis. In addition, a clearer physical picture for chromatic light pulse profile evolution in dispersive fiber is presented.
- An approximate model is developed with the output expressed in a convolution form which represents the output of a LTI system. This model further facilitates the analysis.
- The performance of the HSFOS in accuracy, resolution, speed and noise are investigated.

- A new method for high resolution interrogation of FBG sensors based on the HSFOS is developed. The spectral positioning resolution is improved through over sampling.
- About 10000 lines of codes, including Matlab language, Visual Basic, C language for DSP, have been programmed for signal processing and numerical simulations. Several new signal processing algorithms have been developed and are used not only in the HSFOS project but also adopted in the lab which facilitate the work of other CPT researchers.

6.2 Suggestions for future work

The research conducted exploits new areas for fiber optic sensor signal processing. To further the research, future work is suggested as follows to enhance the performance of the HSFOS and extend its applications.

- **Resolution improvement**

  The resolution of the HSFOS is determined by the following factors:

  1. The amount of dispersion introduced by the dispersive fiber.
  2. The pulse width of the pulse generator.

  The current dispersive fiber used is a DCF or normal single mode fiber (SMF-28). These standard fibers cannot provide high dispersion with low insertion loss. EDFAs could help to compensate the loss at the expense of a limited spectral width, additional noise and distortions to the output of the spectrometer. New fibers may be chosen as better solutions. One of them is photonic crystal fiber (PCF). Some researchers have reported very high dispersion up to 10000 $ps/nm \cdot km$ realized by PCF [90][91]. This should be a possible way to enlarge the dispersion. On the other hand, the pulse width should be reduced. The current pulse generator is built based on the available electronic components in our laboratory from which the narrowest pulse width is 6 ns

(T_{A0}). A new pulse generator should be built or bought to provide 0.1 ns pulse width such that the resolution could be improved to 0.3 nm or better.

- **Signal to noise ratio improvement**

  The loss in the dispersive fiber and low output power of the current light source result in a low signal to noise ratio before an EDFA is used. The EDFA can compensate the loss and the low power of the light source but at the same time limits the spectral width and introduces additional noise and distortion. The current light source is a 1550 nm SLED which has a 1 dBm output power. Now some commercially available SLEDs have an output power up to 20 dBm which might be a good choice. In addition other light sources may also be considered, e.g. supercontinuum. On the other hand, the responsivity of the current O/E converter is too low (less than 300 V/W) so that the high noise level of the oscilloscope lowers the overall signal to noise ratio of the system. One possible solution is to add one high gain low noise post amplifier between the O/E converter and the oscilloscope.

Bibliography

[1] X. Chen, F. Shen, Z. Wang, Z. Huang, and A. Wang, "Micro-air-gap based intrinsic Fabry-Perot interferometric fiber-optic sensor," Appl. Optics **45**, 7760, (2006).

[2] J. Xu, G. Pickrell, X. Wang, W. Peng, K. L. Cooper and A. Wang, "A Novel Temperature-Insensitive Optical Fiber Pressure Sensor for Harsh Environments," IEEE Photon. Technol. Letters. **17**, 870, (2005).

[3] B. Yu, D. W. Kim, J. Deng, H. Xiao and A. Wang, "Fiber Fabry-Perot Sensors for Detection of Partial Discharges in Power Transformers," Appl. Optics **42**, 3241, (2003).

[4] B. Qi, G. R. Pickrell, J. Xu, P. Zhang, Y. Duan, W. Peng, Z. Huang, W. Huo, H. Xiao, R. G. May, and A. Wang, " Novel data processing techniques for dispersive white light interferometer," Opt. Engineering, **42**, 3165, (2003).

[5] M. Han, Y. Zhang, F. Shen, G. Pickrell, and A. Wang, "Signal-processing algorithm for white-light optical fiber extrinsic Fabry-Perot interferometric sensor," Opt. Letters **29**, 1736, (2004).

[6] http://en.wikipedia.org/wiki/Spectrometer

[7] J. M. Hollas, *High Resolution Spectroscop*, 2nd ed., (John Wiley & Sons, 1998).

[8] C. M. Penchina,"Reduction of stray light in in-plane grating spectrometers," Appl. Optics **6**, 1029, (1967).

[9] C. H. Church and L. Gampel, "A wide spectral range ultra-rapid scan spectrometer," Appl. Optics **5**, 241, (1966).

[10] S. A. Dolin and H. A. Kruegle, "Gunter J. PenziasA rapid-scan spectrometer that sweeps corner mirrors through the spectrum," Appl. Optics **6**, 267, (1967).

[11] I. Liberman, C. H. Church, and J. A. Asars, "A high resolution rapid-scanning spectrometer," Appl. Optics **6**, 279, (1967).

[12] J. C. Camm, R. L. Taylor, and R. Lynch, "Synchronized high speed scanning infrared spectrometer," Appl. Optics, **6**, 885, (1967).

[13] J. W. Russell and H. L. Strauss, "Czerny-Turner far infrared spectrometer for the 300-10 cm-1 region," Appl. Optics, **4**, 1131, (1965).

[14] A. R. H. Cole, A. A. Green, G. A. Osborne, and G. D. Reece, "Vacuum grating spectrometer for the mid and far infrared," Appl. Optics, **9**, 23, (1970).

[15] I. F. Silvera and G. Birnbaum , "A far ir spectrometer," Appl. Optics, **9**, 617, (1970).

[16] W. Liller, "Concave gratings for astronomical spectrographs and spectrometers," Appl. Optics,**2**, 187, (1963).

[17] S. Bowyer, R. Kimble, F. Paresce, M. Lampton, and G Penegor, "Continuous-readout extreme-ultraviolet airglow spectrometer," Appl. Optics, **20**, 477, (1981).

[18] B. E. Woodgate, T. Lowinger, and M. Schneider, "Conical focusing crystal spectrometers for cosmic x-ray astronomy," Appl. Optics, **12**, 2759, (1973).

[19] B. P. Byrnak, F. E. Christensen, N. J. Westergaard, and H. W. Schnopper, "Doubly curved imaging Bragg crystal spectrometer for x-ray astronomy," Appl. Optics, **24**, 2543, (1985).

[20] G. G. Shepherd, C. W. Lake, J. R. Miiller, and L. L. Cogger, "A spatial spectral scanning technique for the Fabry-Perot spectrometer," Appl. Optics, **4**, 267, (1965).

[21] M. Clement, B. Moulin, D. Pinet, and P. Stevenin, "Variable magnification spectrometer," Appl. Optics, **13**, 1621, (1974).

[22] A. Ludmirsky, C. Cohen, and Y. Kagan, "Simple fast-scanning Fabry-Perot spectrometer," Appl. Optics, **18**, 545, (1979).

[23] K. C. Herr, and G. C. Pimentel, "A rapid-scan infrared spectrometer; flash photolytic detection of chloroformic acid and of CF2," Appl. Optics, **4**, 25, (1965).

[24] C. W. Hand, P. Z. Kaufmann, and R. M. Hexter, "Kinetic spectroscopy in the infrared: a rapid-scan infrared spectrometer," Appl. Optics, **5**, 1097, (1966).

[25] I. G. Nolt, R. D. Kirby, C. D. Lytle, and A. J. Sievers, "A double pass spectrometer for the far infrared," Appl. Optics, **8**, 309, (1969).

[26] R. H. Hunt, C. W. Robertson, and E. K. Plyler, "A four-pass high resolution spectrometer for the near infrared," Appl. Optics, **6**, 1295, (1967).

[27] W. G. Fastie, "Exit slit mirrors for the Ebert spectrometer," Appl. Optics, **11**, 1960, (1972).

[28] H. J. Babrov and R. H. Tourin, "Performance of a commercial rapid scanning spectrometer in emission and absorption," Appl. Optics, **7**, 2171, (1968).

[29] R. A. Hill, "Rapid scan spectrometers for the diagnostics of transient plasmas," Appl. Optics, **7**, 2184, (1968).

[30] P. Buchhave and C. H. Church, "A wide range, rapid scanning spectrometer for emission and absorption measurements," Appl. Optics, **7**, 2200, (1968).

[31] H. A. Kruegle and S. A. Dolin, "A rapid-scan spectrometer for scanning 2000 A-15 micrometers in 3 sec," Appl. Optics, **8**, 2107, (1969).

[32] R. A. Harber and G. E. Sonnek, "Spectral analysis using the electronic scanning spectrometer," Appl. Optics, **5**, 1039, (1966).

[33] D. J. Baker and A. J. Steed, "Electronic scanning spectrometer for measurements of rapidly changing spectra," Appl. Optics, **7**, 2190, (1968).

[34] M. Harwit and N. J. A. Sloane, *Hadamard Transform Optics*, (Academic Press, Inc., 1979).

[35] B. A. Tinsley, "The circularly symmetric grille spectrometer," Appl. Optics, **5**, 1139, (1966).

[36] B. A. Tinsley, "A grille spectrometer for measurements near 14 micrometers," Appl. Optics, **8**, 1831, (1969).

[37] J. A. Decker, Jr., "Experimental realization of the multiplex advantage with a Hadamard-transform spectrometer," Appl. Optics, **10**, 510, (1971).

[38] J. A. Decker, Jr., "Hadamard-transform exhaust-analysis spectrometer," Appl. Optics, **10**, 24, (1971).

[39] P. Hansen and J. Strong, "High resolution Hadamard transform spectrometer," Appl. Optics, **11**, 502, (1972).

[40] M. Harwit, P. G. Phillips, L. W. King, and D. A. Briotta, Jr., "Two asymmetric Hadamard transform spectrometers," Appl. Optics, **13**, 2669, (1974).

[41] M. H. Tai, D. A. Briotta, Jr., N. S. Kamath, and M. Harwit, "ractical multi-spectrum Hadamard transform spectrometer," Appl. Optics, **14**, 2533, (1975).

[42] F. A. Murzin, T. S. Murzina, and V. B. Shlishevshy, "New grilles for Girard spectrometers," Appl. Optics, **24**, 3625, (1985).

[43] N. Sugimoto, "Hadamard transform active long-path absorption spectrometer system for measurements of atmospheric trace species," Appl. Optics, **25**, 863, (1986).

[44] J. L. Robichaud, W. K. Wong, and R. A. Van Tassel, "Evaluation of a Hadamard-coded photodiode-array spectrometer under low illumination," Appl. Optics, **33**, 75, (1994).

[45] B. Yu, *Development of Tunable Optical Filters For Interrogation of White-Light Interferometric Sensors*, dissertation, (Virginia Tech, 2005).

[46] G. Hernandez and K. C. Clark, "Electro-optic high-resolution Fabry-Perot spectrometer," Appl. Optics, **33**, 1989, (1994).

[47] R. P. Netterfield, C. H. Freund, J. A. Seckold, and C. J. Walsh, "Design of a lithium niobate Fabry-Perot etalon-based spectrometer," Appl. Optics, **36**, 4556, (1997).

[48] N. Sheppard, "The Histroical Development of Experimental Techniques in Vibrational Spectroscopy," *Handbook of Vibrational Spectroscopy*, **1**, 1, (2002).

[49] B. F. Hochheimer and C. F. Bradley, "A Fourier transform spectrometer for the 10-10,000 cm-1 spectral region," Appl. Optics, **8**, 557, (1969).

[50] K. Sakai, "Michelson-type Fourier spectrometer for the far infrared," Appl. Optics, **11**, 2894, (1972).

[51] J. Kauppinen, "Double-beam high resolution Fourier spectrometer for the far infrared," Appl. Optics, **14**, 1987, (1975).

[52] J. Kachmarsky, C. Belorgeot, A. Pluchino, and K. D. Moller, "Far-infrared high-resolution Fourier transform spectrometer: applications to H2O, NH3, and NO2 lines," Appl. Optics, **15**, 708, (1976).

[53] J. Kauppinen, "Working resolution of 0.010 cm-1 between 20 cm-1 and 1200 cm-1 by a Fourier spectrometer," Appl. Optics, **18**, 1788, (1979).

[54] R. P. Cageao, J. Blavier, J. P. McGuire, Y. Jiang, V. Nemtchinov, F. P. Mills, and S. P. Sander, "High-Resolution Fourier-Transform Ultraviolet -Visible Spectrometer for

the Measurement of Atmospheric Trace Species: Application to OH," Appl. Optics, **40**, 2024, (2001).

[55] A. A. Balashov, V. S. Bukreev, N. G. Kultepin, I. N. Nesteruk, E. B. Perminov, V. A. Vagin, and G. N. Zhizhin, "High resolution Fourier transform spectrometer (0.005 cm-1) for the 0.6-100-[mgr]m spectral range (E)," Appl. Optics, **17**, 1716, (1978).

[56] T. Okamoto, S. Kawata, and S. Minami, "Fourier transform spectrometer with a self-scanning photodiode array," Appl. Optics, **23**, 269, (1984).

[57] G. Zhan, "Static Fourier-Transform Spectrometer with Spherical Reflectors," Appl. Optics, **41**, 560, (2002).

[58] M. J. Padgett, A. R. Harvey, A. J. Duncan, and W. Sibbett, "Single-pulse, Fourier-transform spectrometer having no moving parts," Appl. Optics, **33**, 6035, (1994).

[59] J. Courtial, B. A. Patterson, A. R. Harvey, W. Sibbett, and M. J. Padgett, "Design of a static Fourier-transform spectrometer with increased field of view," Appl. Optics, **35**, 6698, (1996).

[60] J. Courtial, B. A. Patterson, W. Hirst, A. R. Harvey, A. J. Duncan, W. Sibbett, and M. J. Padgett, "Static Fourier-transform ultraviolet spectrometer for gas detection," Appl. Optics, **36**, 2813, (1997).

[61] D. Steers, W. Sibbett, and M. J. Padgett, "Dual-Purpose, Compact Spectrometer and Fiber-Coupled Laser Wavemeter Based on a Wollaston Prism," Appl. Optics, **37**, 5777, (1998).

[62] K. Sakai, H. Masumoto, K. Ichimura, and H. Kojima, "High-resolution lamellar-grating Fourier-transform spectrometer for the submillimeter region (E)," Appl. Optics, **17**, 1709, (1978).

[63] G. D. Smith and R. A. Palmer, "Fast Time-resolved Mid-infrared Spectroscopy Using an Interferometer," *Handbook of Vibrational Spectroscopy*, **1**, 625 ,(2002).

[64] C. Rodig and F. Siebert, "Instruental Aspects of Time-resolved Spectra Generated Using Step-scan Interferometers," *Handbook of Vibrational Spectroscopy*, **1**, 641, (2002).

[65] K. Masutani, "Time-resolved Mid-infrared Spectrometry Using an Asynchronous Fourier Transform Infrared Spectrometer," *Handbook of Vibrational Spectroscopy*, **1**, 655, (2002).

[66] http://en.wikipedia.org/wiki/Streak_camera.

[67] J. J. Hillman, D. E. Jennings, and J. L. Faris, "Diode laser-CO2 laser heterodyne spectrometer: measurement of 2sQ(1,1) in 2nu2 - nu2 of NH3," Appl. Optics, **18**, 1808, (1979).

[68] D. A. Glenar, D. Deming, F. Espenak, T. Kostiuk, and M. J. Mumma, "Laser heterodyne spectrometer for helioseismology," Appl. Optics, **25**, 58, (1986).

[69] F. Schmlling, B. Klumb, M. Harter, R. Schieder, B. Vowinkel, and G. Winnewisser, "High-Sensitivity Mid-Infrared Heterodyne Spectrometer With a Tunable Diode Laser as a Local Oscillator," Appl. Optics, **37**, 5771, (1998).

[70] G. Sonnabend, D. Wirtz, F. Schmulling, and R. Schieder, "Tuneable Heterodyne Infrared Spectrometer for Atmospheric and Astronomical Studies," Appl. Optics, **41**, 2978, (2002).

[71] M. B. Sinclair, M. A. Butler, A. J. Ricco, and S. D. Senturia, "Synthetic spectra: a tool for correlation spectroscopy," Appl. Optics, **36**, 3342, (1997).

[72] Y. Tong, L. Chan, and H. Tsang, "Fiber dispersion or pulse spectrum measurement using a sampling oscilloscope," Electron. Letters, **33**, 983, (1997).

[73] Y. Tong and H. Tsang, "Direct time-domain measurement of optical spectra of ultrashort pulses," IEEE LEOS 97, **2**, 242, (1997).

[74] P.V. Kelkar, F. Coppinger, A.S. Bhushan, and B. Jalali, "Time-domain optical sensing," Electron. Letters, **35**, 1661, (1999).

[75] P.V. Kelkar, F. Coppinger, A.S. Bhushan, and B. Jalali, "Time domain optical sensing," IEEE LEOS 99 , **1**, 381, (1999).

[76] J. Chou, Y. Han, and B. Jalali, "Time-wavelength spectroscopy for chemical sensing," IEEE Photon. Technol. Letters, **16**, 1140, (2004).

[77] J. Chou, Y. Han, and B. Jalali, "Binary chemical detector using time-wavelength spectroscopy," IEEE IMTC 04. Proceedings of the 21st, **1**, 10, (2004).

[78] J. Chou, Y. Han, and B. Jalali, "Biochemical sensing using time-wavelength spectroscopy," Sensors for Industry Conference, Proceedings the ISA/IEEE, 165, (2004).

[79] H. Taylor, "An optical analog-to-digital converter–Design and analysis," IEEE Quantum Electron., **15**, 210, (1979).

[80] L. Brzozowski and E.H. Sargent, "All-optical analog-to-digital converter for photonic networks using multilevel signaling," Transparent Optical Networks, 203, (2000).

[81] L. Brzozowski and E.H. Sargent, "All-optical analog-to-digital converters, hard limiters, and logic gates," J. Lightwave Technol., **19**, 114 ,(2001).

[82] S. Bhushan, P. V. Kelkar, B. Jalali, O. Boyraz and M. Islam, "130 Gsa/s Photonic Analog-to-Digital Converter with Time Stretch Preprocessor," IEEE Photon. Technol. Letters, **14**, 684, (2002).

[83] X. Hou, A. Daryoush, W. Rosen, H. Burstyn, and P. Zalud, "Design of an ultra high-speed all-optical analog-to-digital converter," Radar Conference, Proceedings of the IEEE, 520, (2004).

[84] Y. Wang, M. Han, and A. Wang, "High-speed fiber-optic spectrometer for signal demodulation of interferometric fiber-optic sensors," Opt. Letters **31**, 2408, (2006).

[85] D. Marcuse,"Pulse distortion in single-mode fibers," Appl. Optics **19**, 1653, (1980).

[86] D. Marcuse, "Propagation of pulse fluctuations in single-mode fibers," Appl. Optics **19**, 1856, (1980).

[87] D. Marcuse, "Pulse distortion in single-mode fibers. Part 2," Appl. Optics **20**, 2969, (1981).

[88] Y. Wang, M. Han, and A. Wang, "Analysis of a high-speed fiber-optic spectrometer for fiber-optic sensor signal processing," Appl. Optics **46**, 8149, (2007).

[89] G.P.Agrawal, *Fiber-optic communication systems*, 3rd ed., (John Wiley & Sons, 2002).

[90] Y. Ni, L. Zhang, L. An, J. Peng, and C. Fan, "Dual-core photonic Crystal fiber for dispersion compensation," IEEE Photon. Technol. Lett. **16**, 1516, (2004).

[91] A. Huttunen and P. Torma, "Optimization of dual-core and microstructure fiber geometries for dispersion compensation and large mode," Opt. Express **13**, 627, (2005).

Appendix A

Numerical simulation results for accuracy analysis

In the following figures, the numerical simulation results for the inherent error Δ_1 are listed in Fig.A.1∼Fig.A.12. The results for model error Δ_2 are listed in Fig.A.13∼Fig.A.24. The following table presents the conditions of those simulations. In Fig.A.19(a)(b) and Fig.A.22(a)(b), large simulation errors occurred in the left part of the curves due to the zero point of β_2 at 1520 for fiber 1 nm combined with the wide pulse width in the simulations.

Table A.1: The conditions for the numerical simulation

Figure index	Error type	Spectrum type	Pulse type
A.1∼A.3	Δ_1	FP spectrum FP cavity length: 73 μm	Gaussian
A.4∼A.6	Δ_1	Gaussian spectrum 10 nm, centered at 1550 nm	Gaussian
A.7∼A.9	Δ_1	FP spectrum FP cavity length: 73 μm	rectangle $C_L = C_R = 0.33$
A.10∼A.12	Δ_1	Gaussian spectrum 10 nm, centered at 1550 nm	rectangle $C_L = C_R = 0.33$
A.1∼A.3	Δ_2	FP spectrum FP cavity length: 73 μm	Gaussian
A.4∼A.6	Δ_2	Gaussian spectrum 10 nm, centered at 1550 nm	Gaussian
A.7∼A.9	Δ_2	FP spectrum FP cavity length: 73 μm	rectangle $C_L = C_R = 0.33$
A.10∼A.12	Δ_2	Gaussian spectrum 10 nm, centered at 1550 nm	rectangle $C_L = C_R = 0.33$

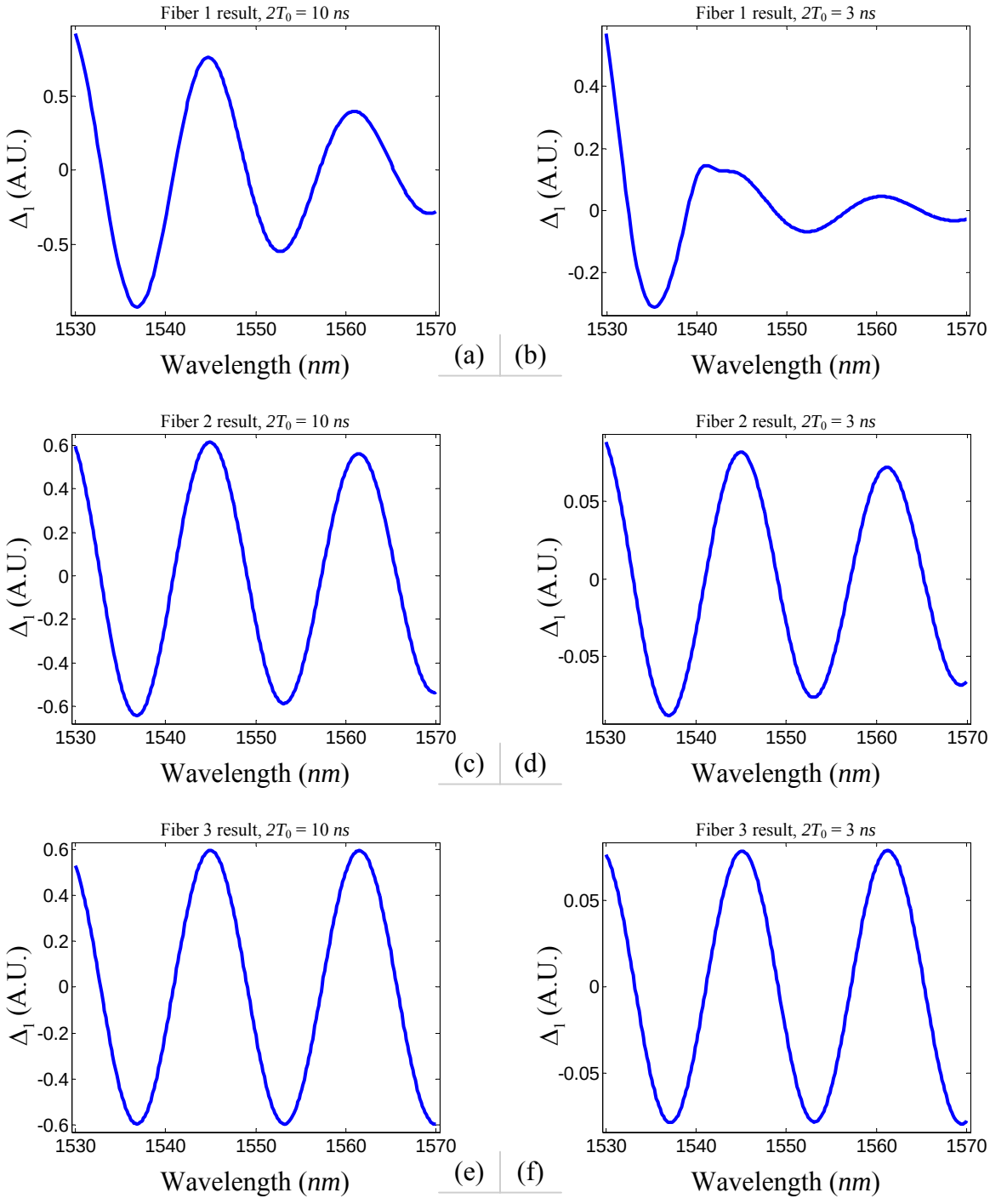

Figure A.1: Numerical simulation results of the inherent error Δ_1 (Gaussian pulse, FP spectrum, $DL = 1ns/mn$)

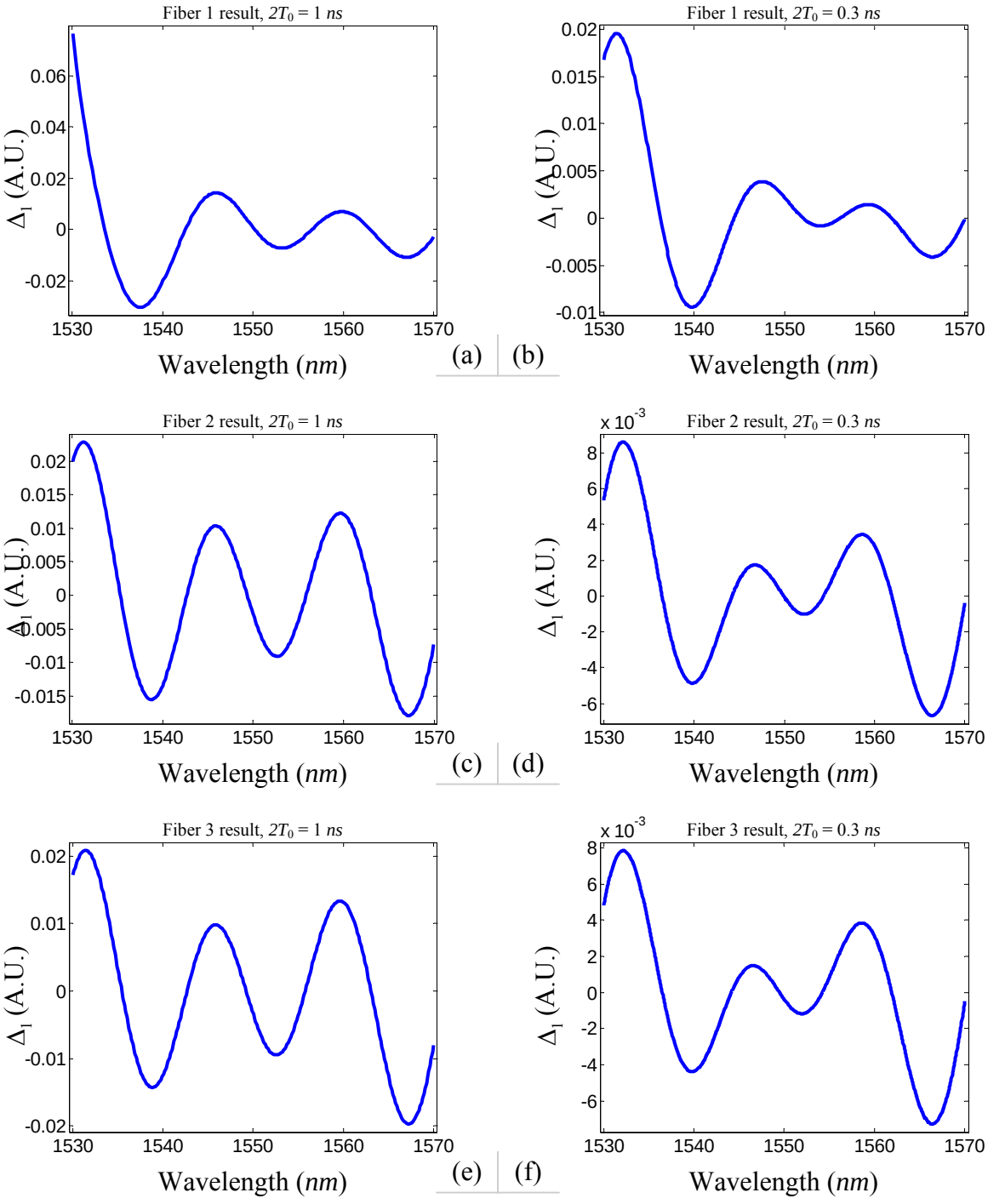

Figure A.2: Numerical simulation results of the inherent error Δ_1 (Gaussian pulse, FP spectrum, $DL = 1ns/mn$) (continued)

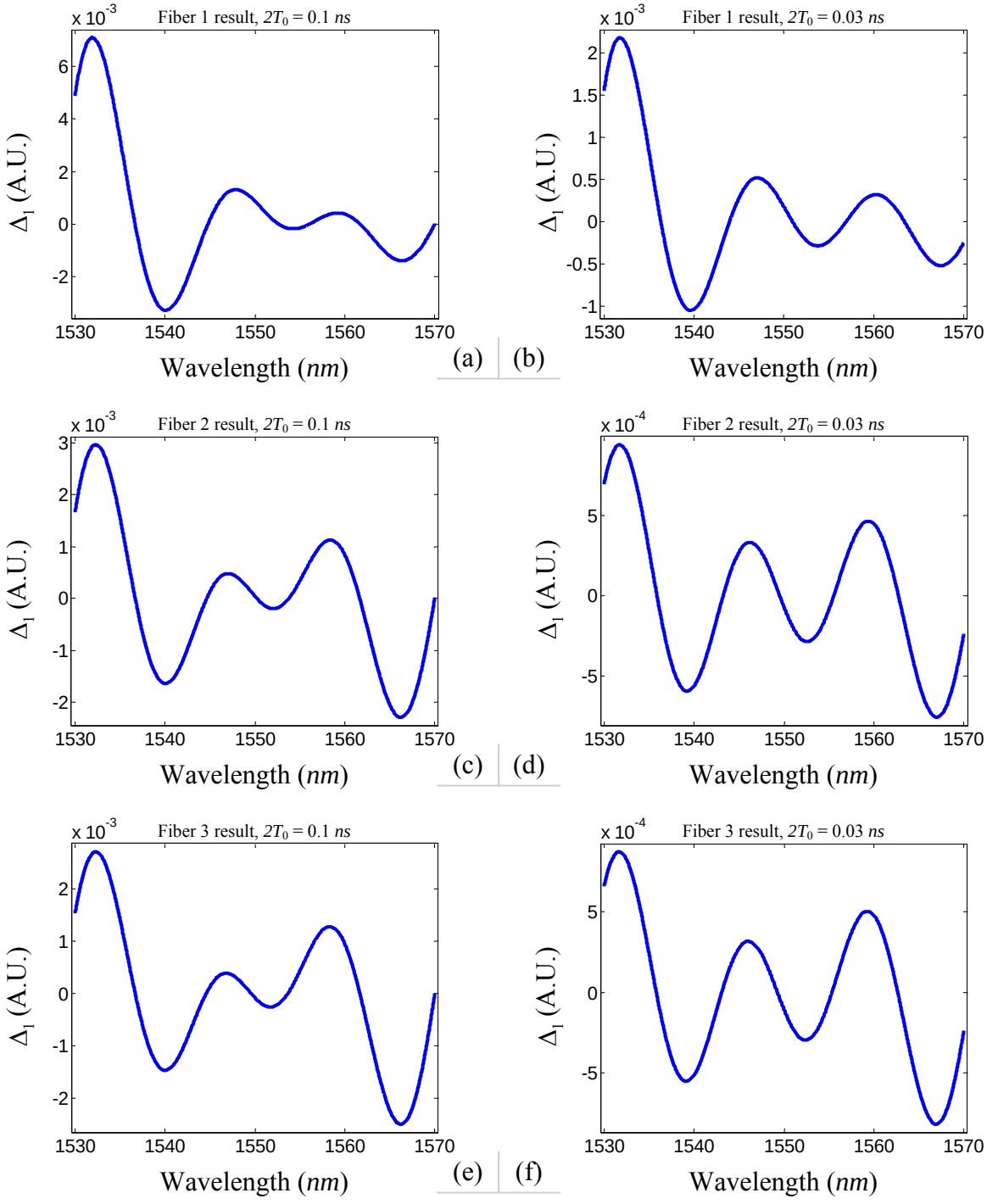

Figure A.3: Numerical simulation results of the inherent error Δ_1 (Gaussian pulse, FP spectrum, $DL = 1ns/mn$) (continued)

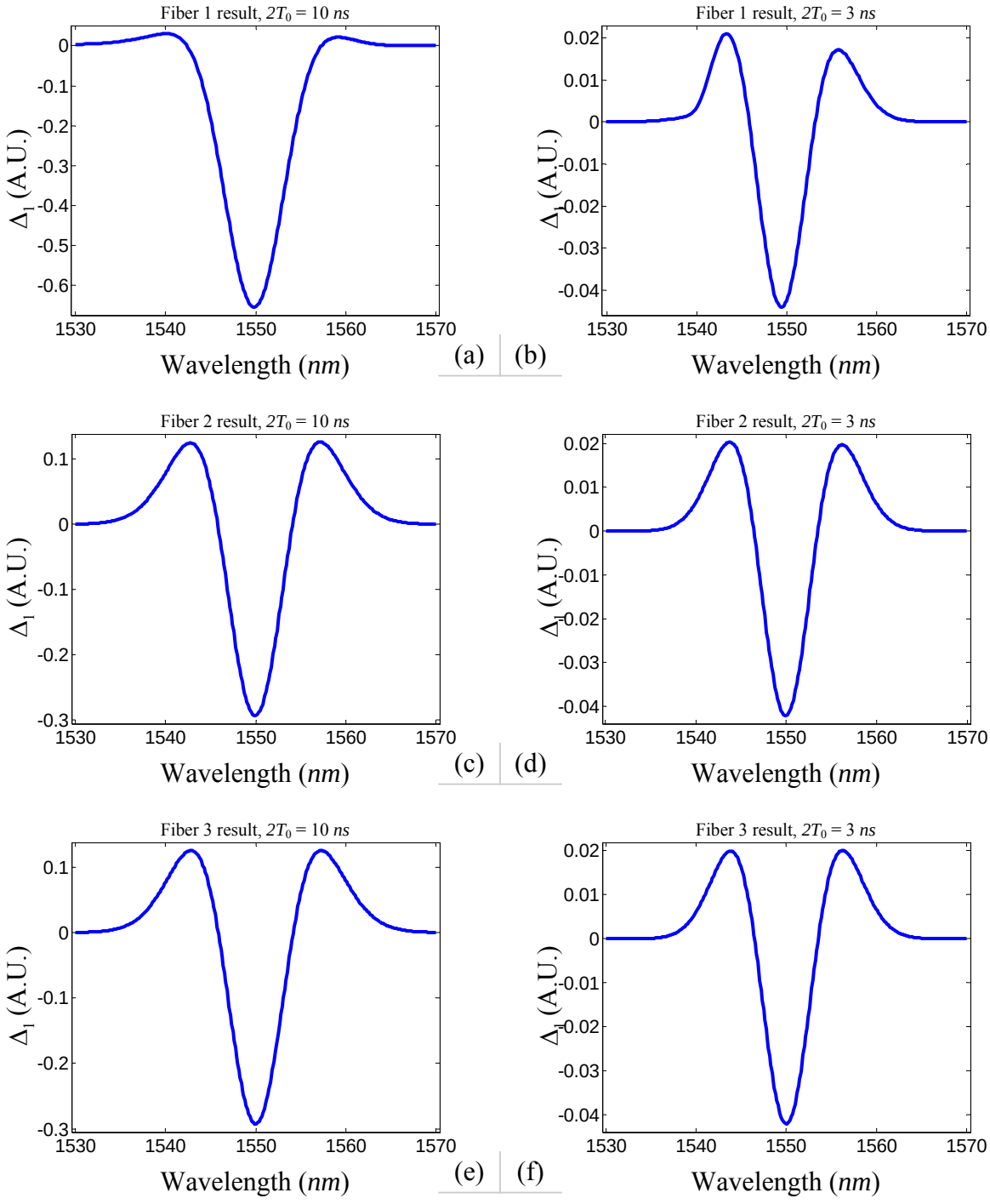

Figure A.4: Numerical simulation results of the inherent error Δ_1 (Gaussian pulse, Gaussian spectrum, $DL = 1ns/mn$)

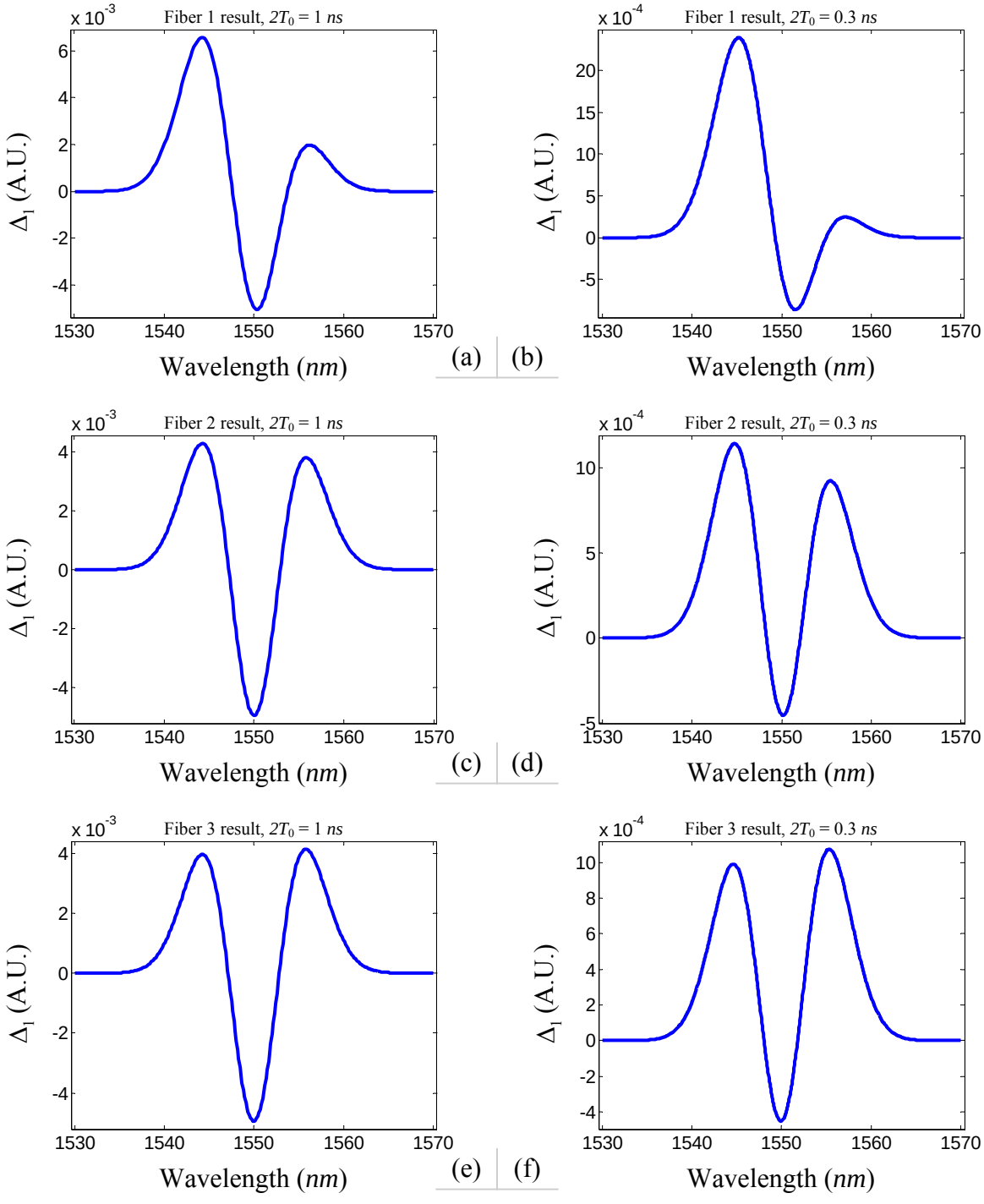

Figure A.5: Numerical simulation results of the inherent error Δ_1 (Gaussian pulse, Gaussian spectrum, $DL = 1ns/mn$) (continued)

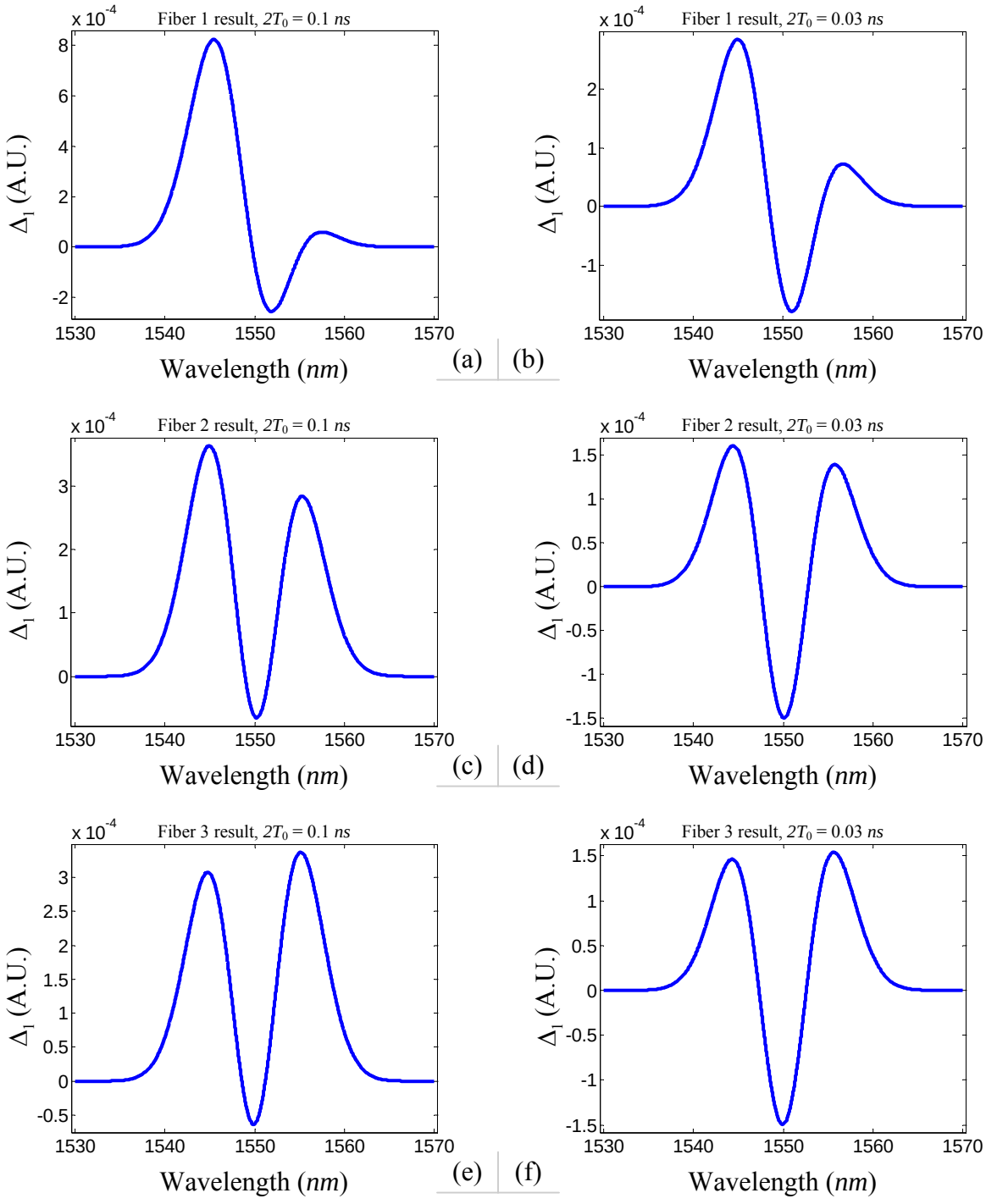

Figure A.6: Numerical simulation results of the inherent error Δ_1 (Gaussian pulse, Gaussian spectrum, $DL = 1ns/mn$) (continued)

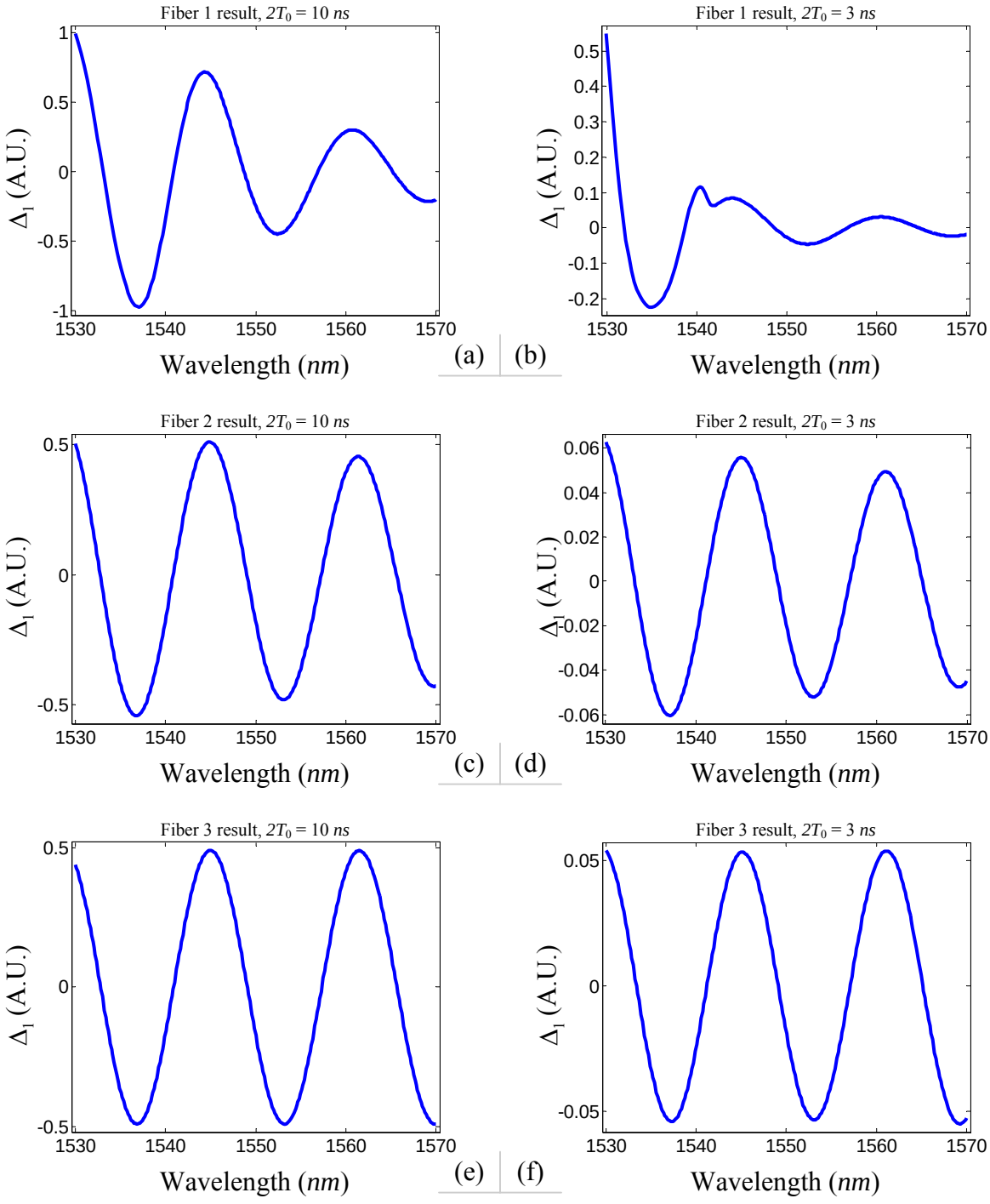

Figure A.7: Numerical simulation results of the inherent error Δ_1 (rectangular pulse, FP spectrum, $DL = 1ns/mn$)

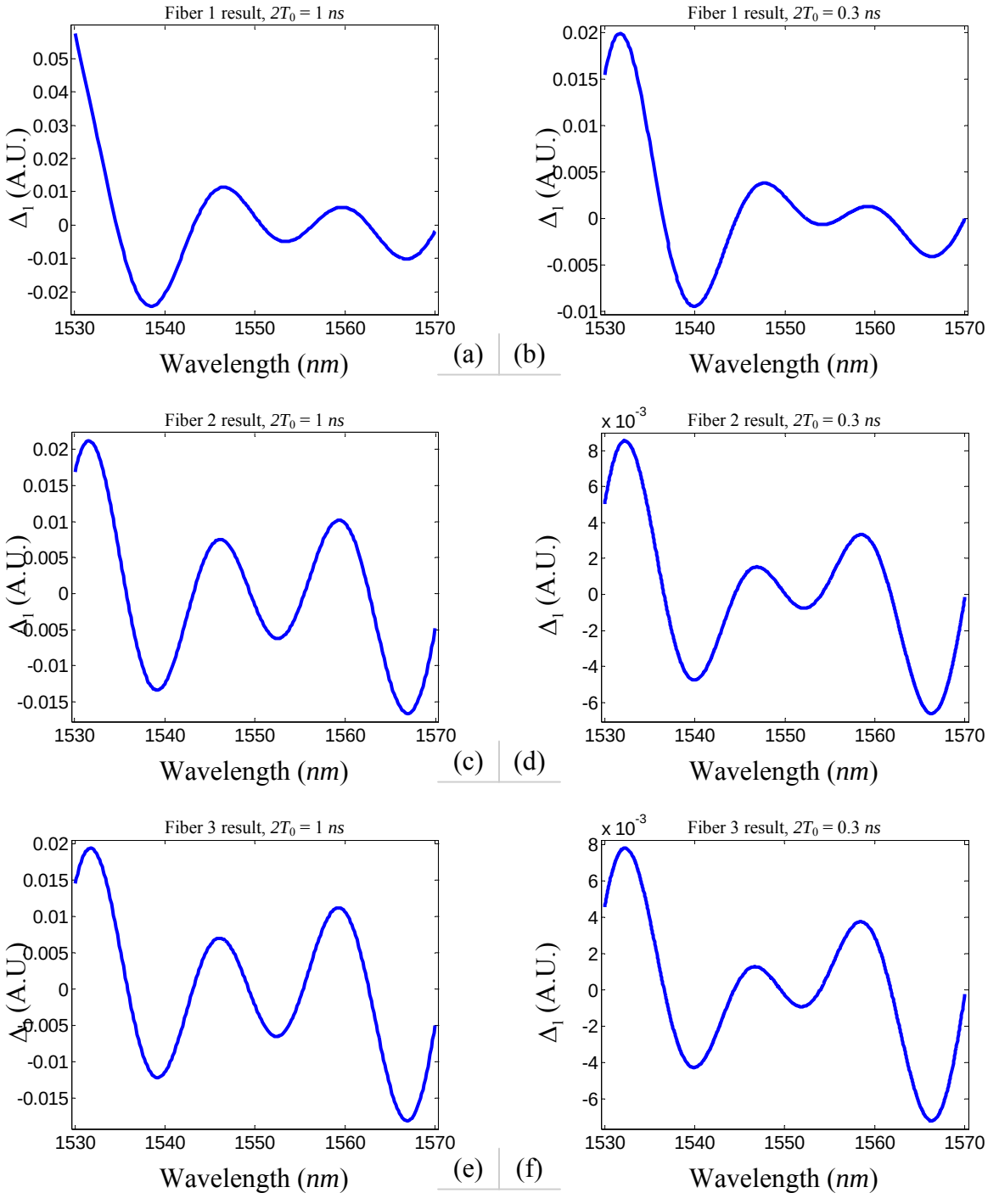

Figure A.8: Numerical simulation results of the inherent error Δ_1 (rectangular pulse, FP spectrum, $DL = 1ns/mn$) (continued)

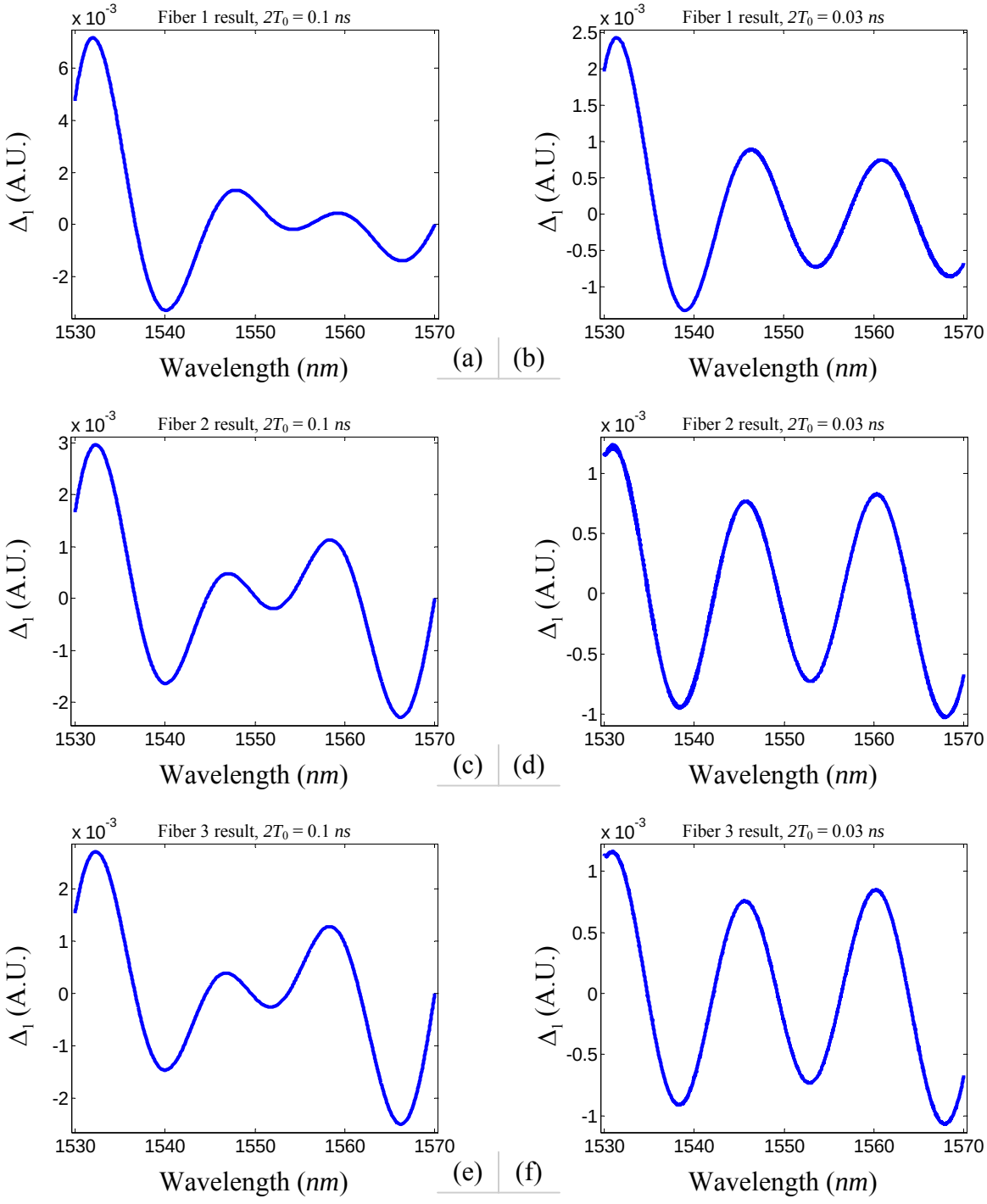

Figure A.9: Numerical simulation results of the inherent error Δ_1 (rectangular pulse, FP spectrum, $DL = 1ns/mn$) (continued)

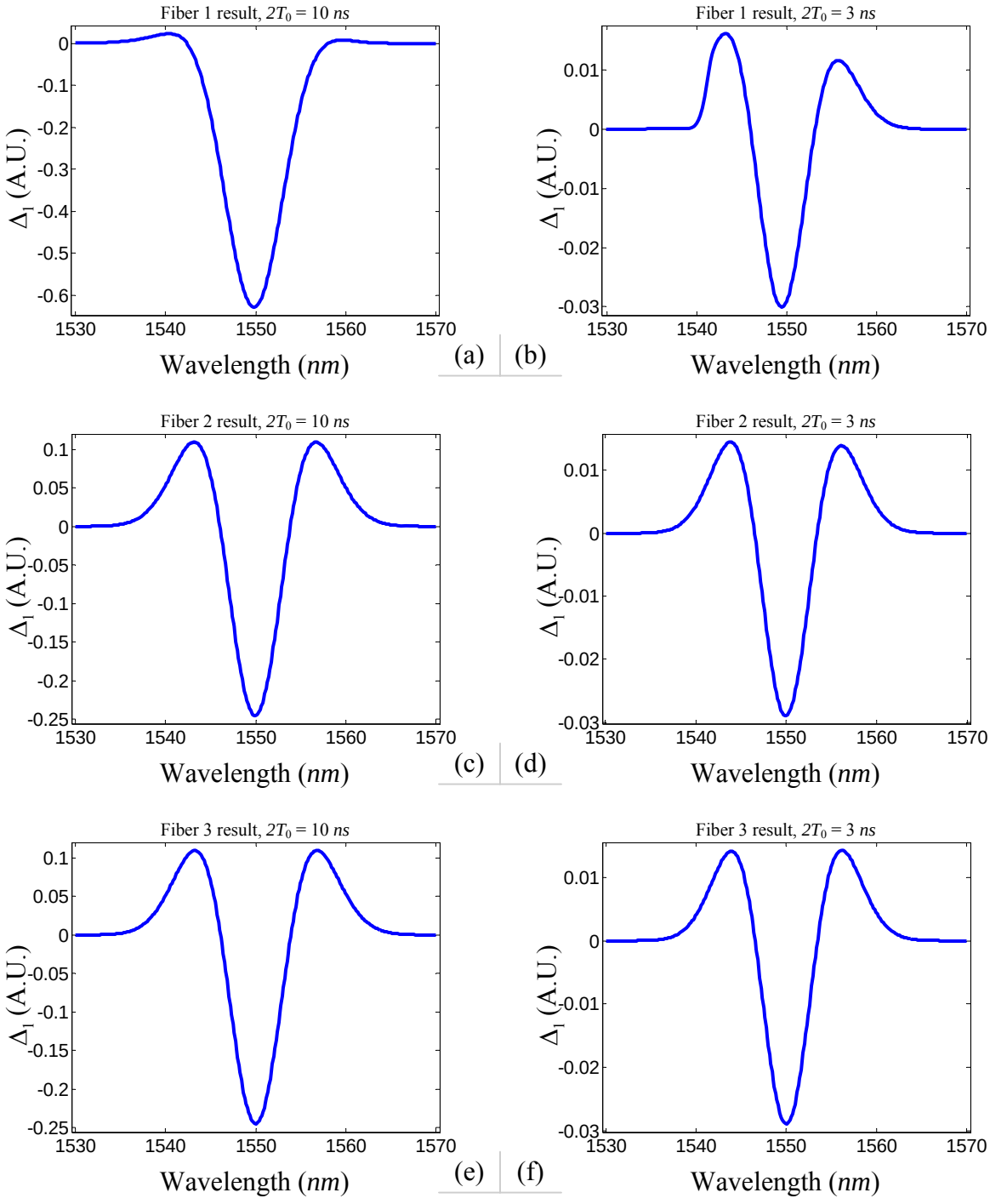

Figure A.10: Numerical simulation results of the inherent error Δ_1 (rectangular pulse, Gaussian spectrum, $DL = 1ns/mn$)

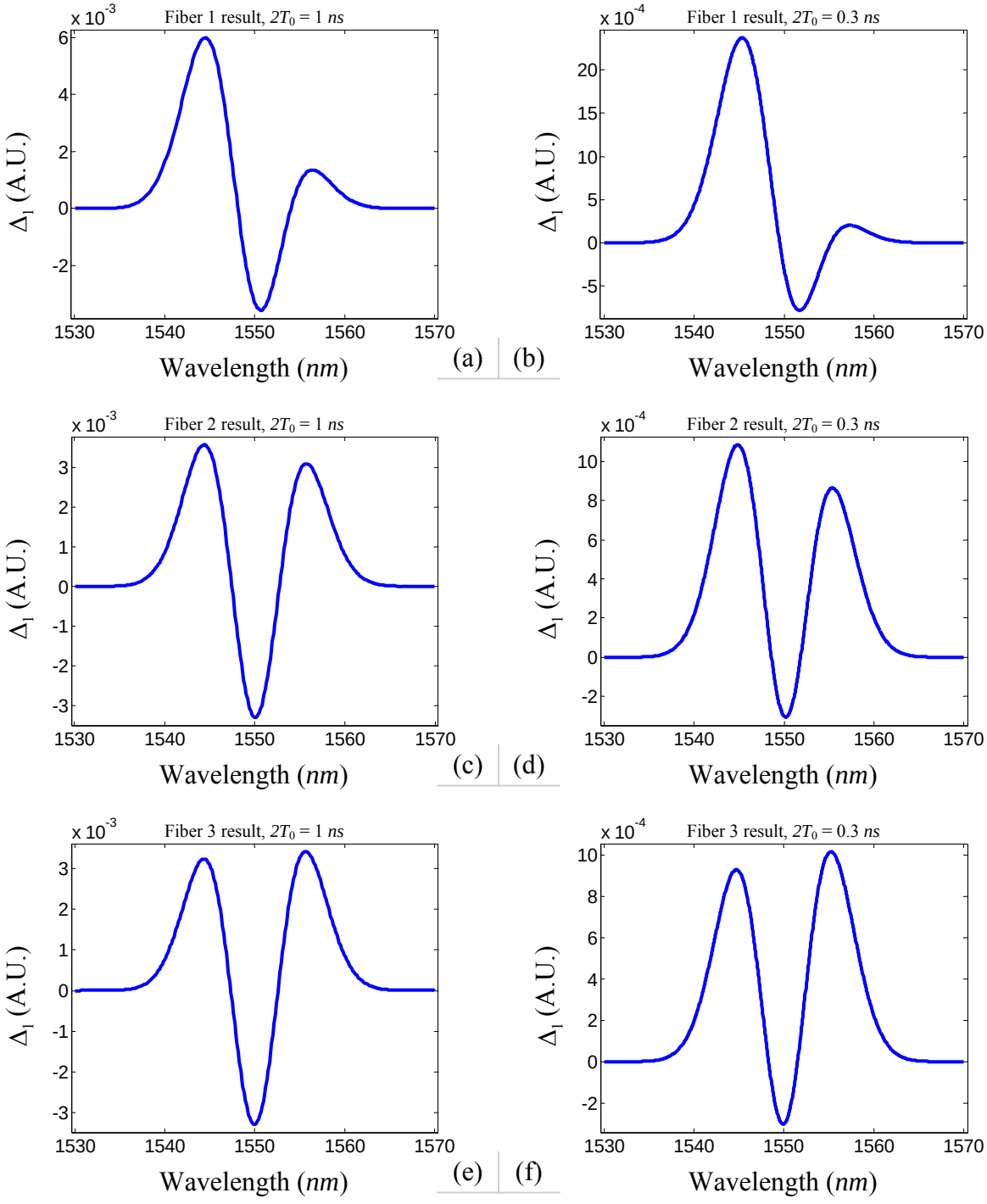

Figure A.11: Numerical simulation results of the inherent error Δ_1 (rectangular pulse, Gaussian spectrum, $DL = 1ns/mn$) (continued)

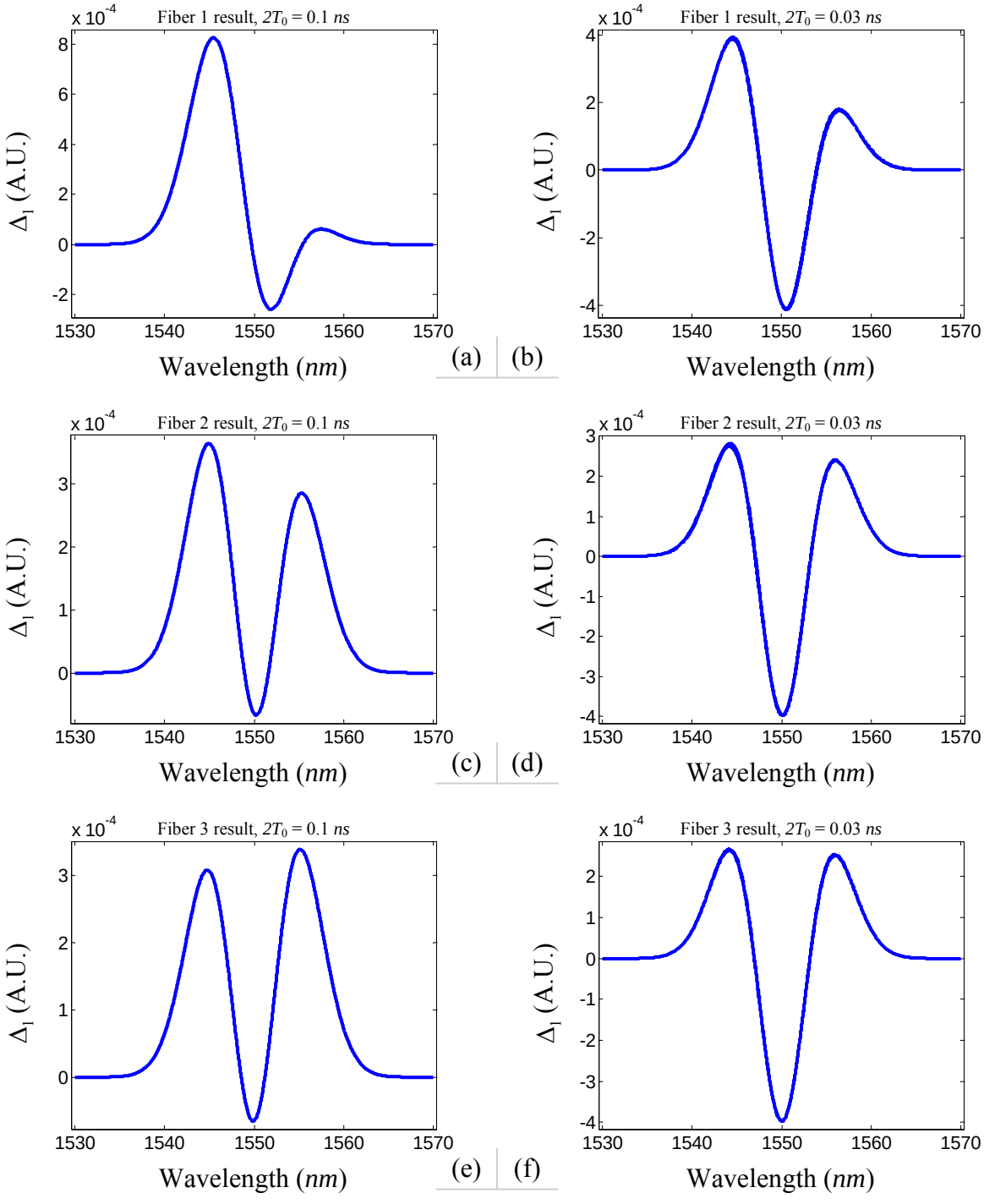

Figure A.12: Numerical simulation results of the inherent error Δ_1 (rectangular pulse, Gaussian spectrum, $DL = 1ns/mn$) (continued)

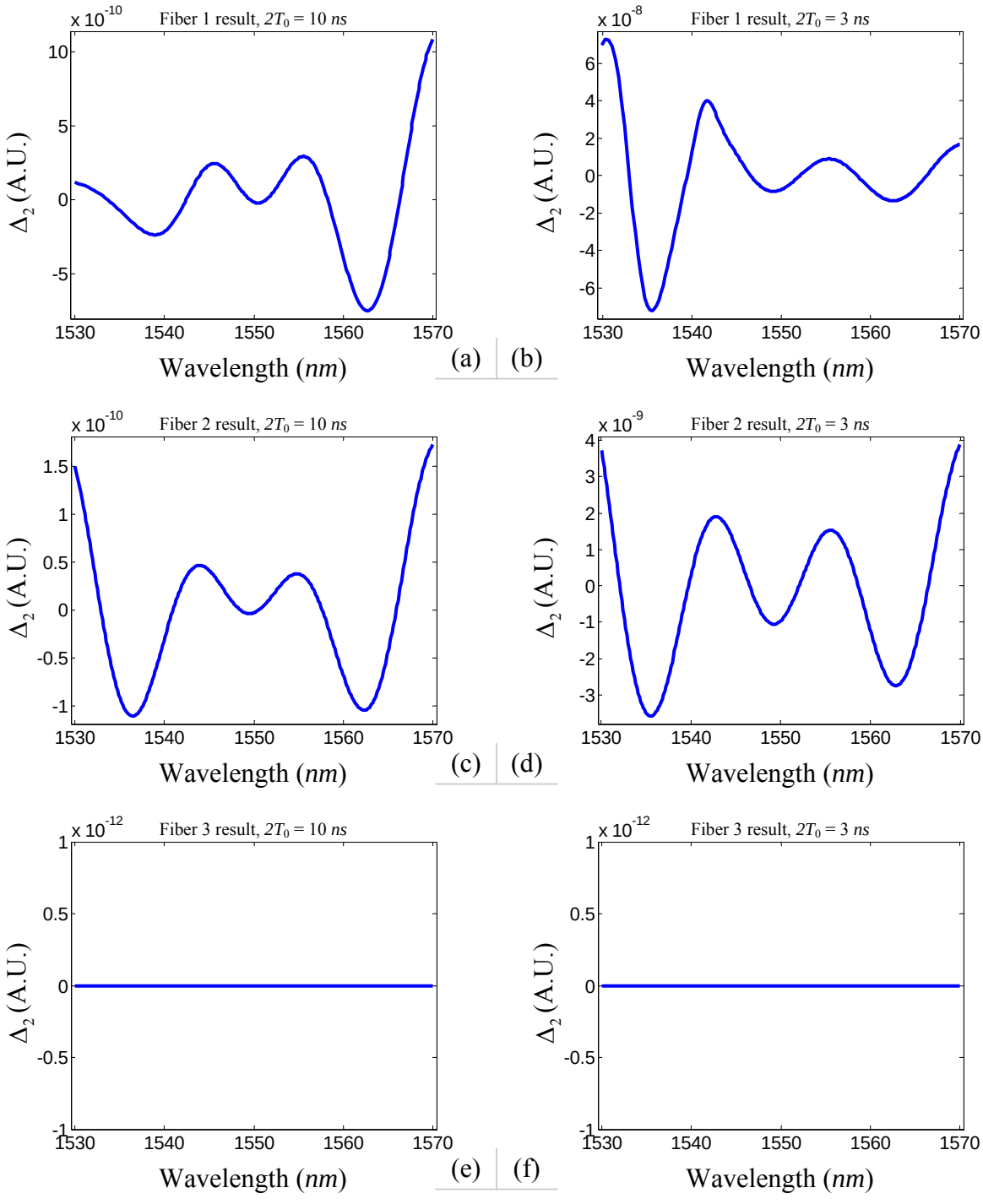

Figure A.13: Numerical simulation results of the model error Δ_2 (Gaussian pulse, FP spectrum, $DL = 1ns/mn$)

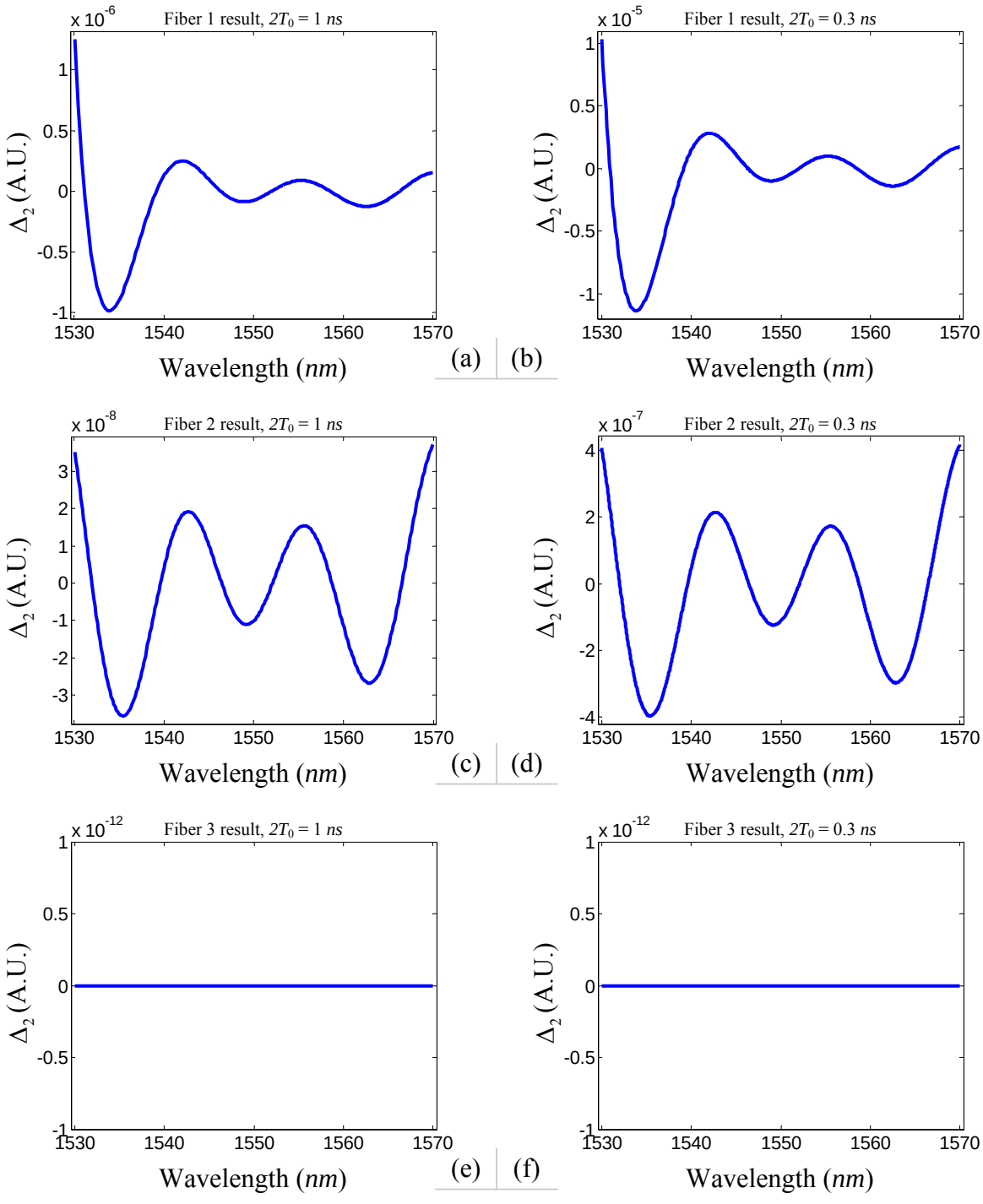

Figure A.14: Numerical simulation results of the model error Δ_2 (Gaussian pulse, FP spectrum, $DL = 1ns/mn$) (continued)

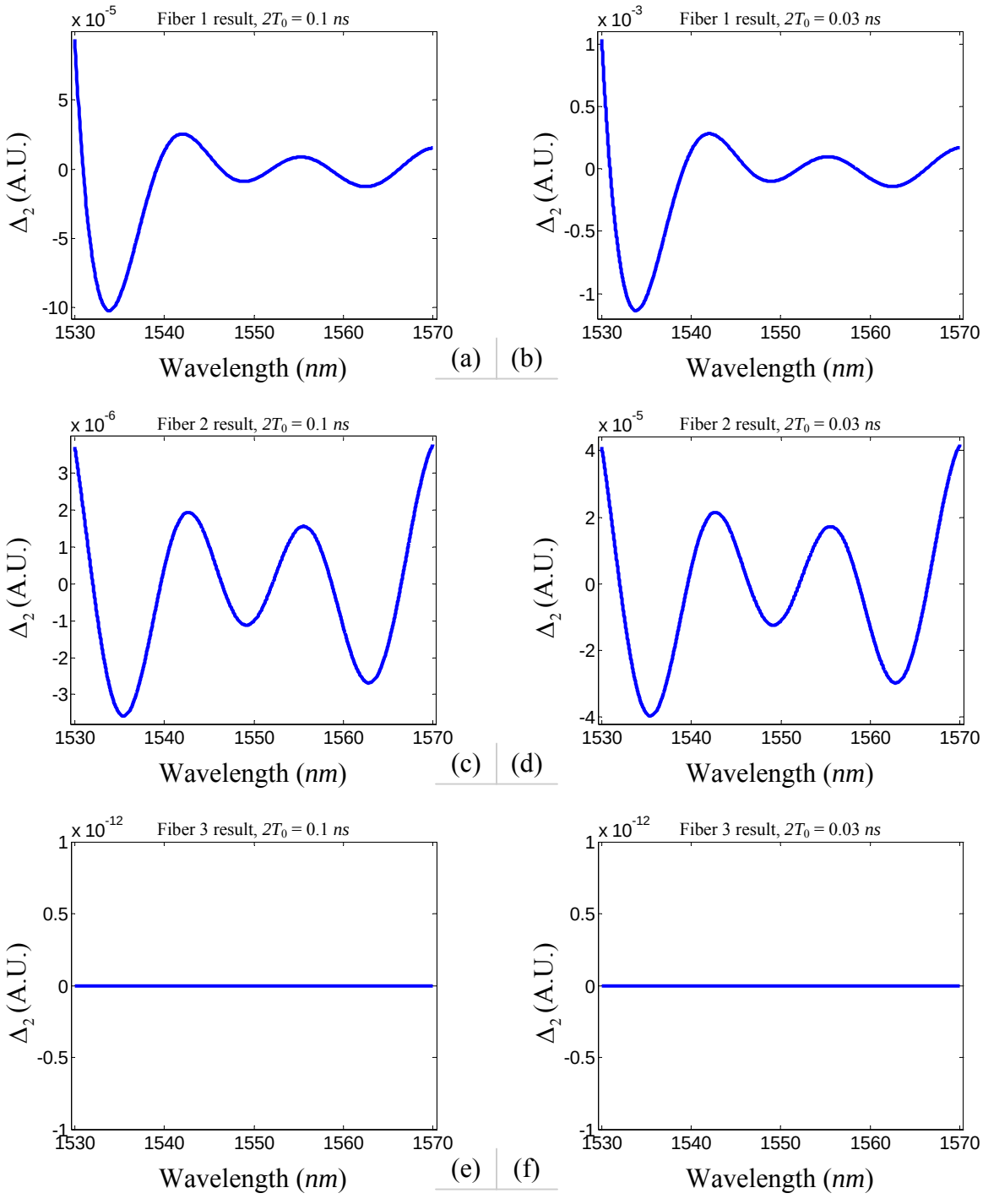

Figure A.15: Numerical simulation results of the model error Δ_2 (Gaussian pulse, FP spectrum, $DL = 1ns/mn$) (continued)

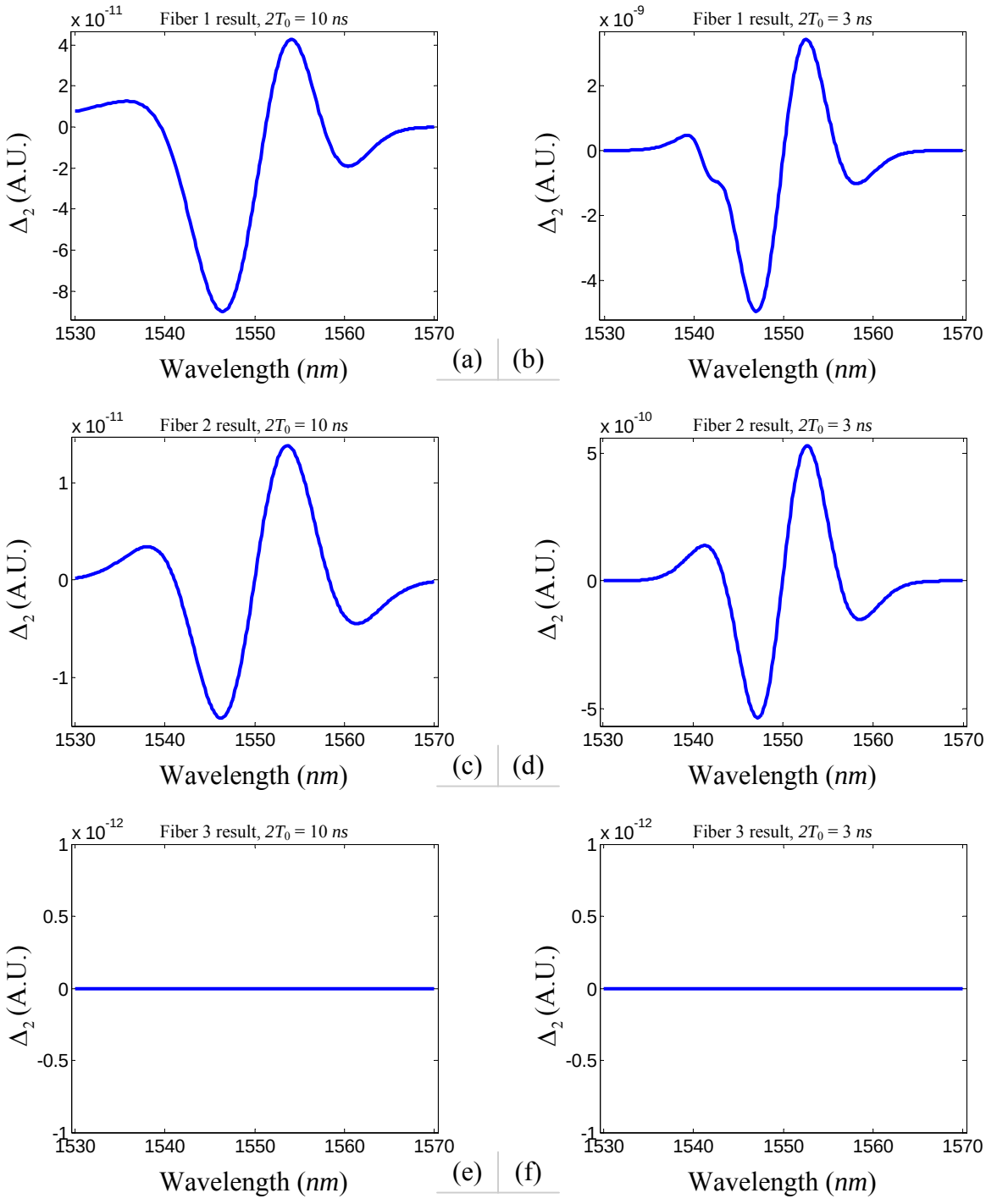

Figure A.16: Numerical simulation results of the model error Δ_2 (Gaussian pulse, Gaussian spectrum, $DL = 1ns/mn$)

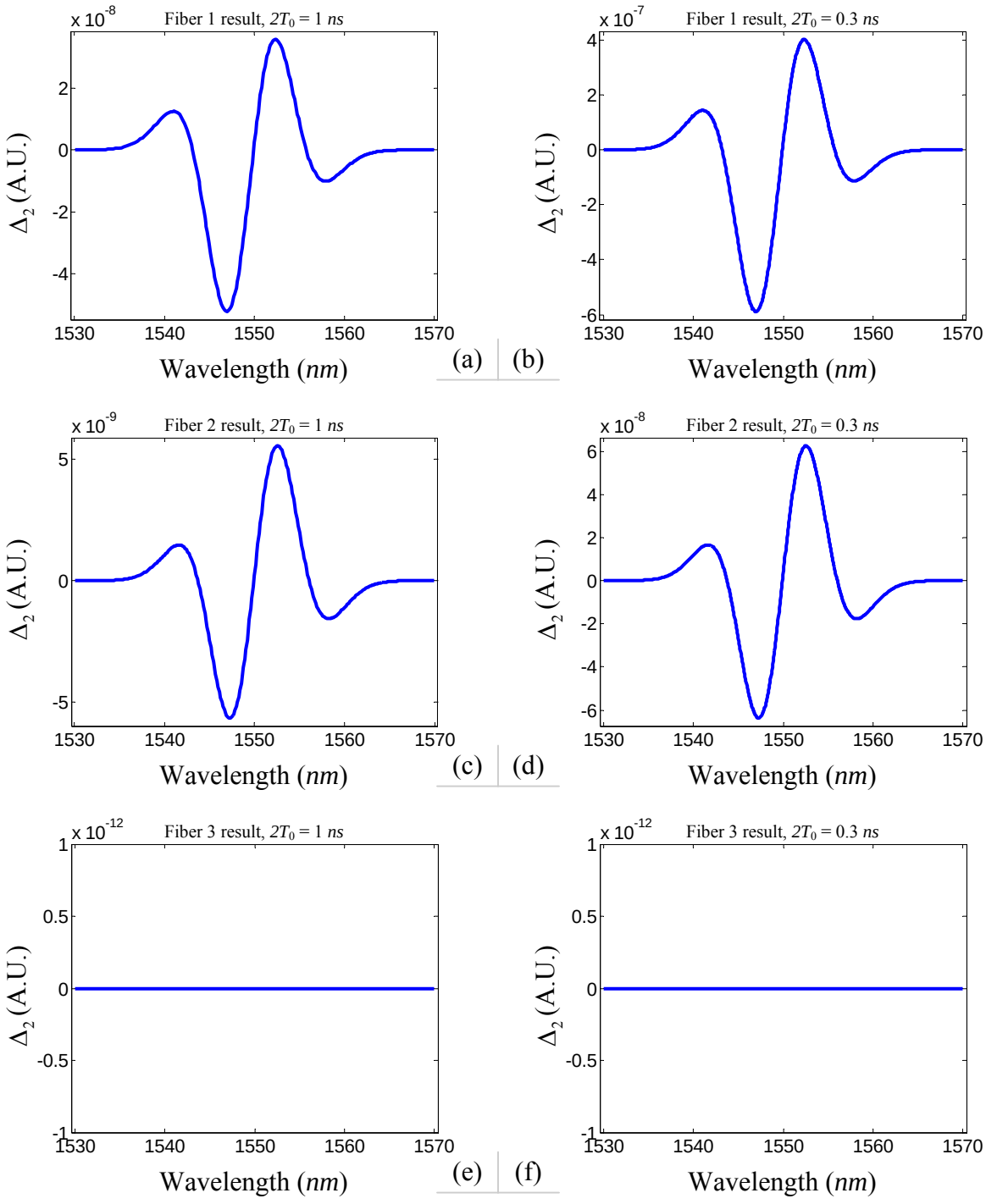

Figure A.17: Numerical simulation results of the model error Δ_2 (Gaussian pulse, Gaussian spectrum, $DL = 1ns/mn$) (continued)

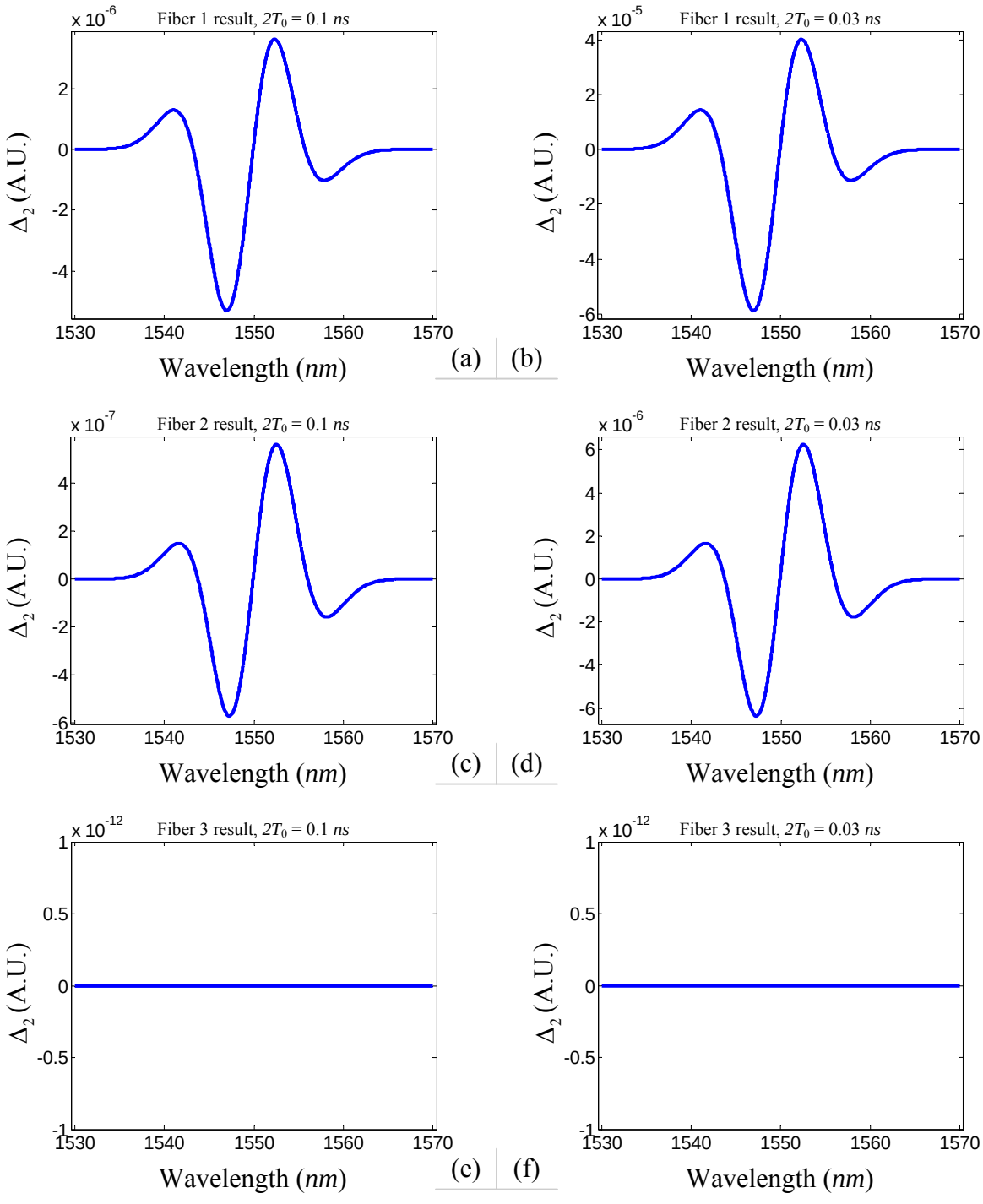

Figure A.18: Numerical simulation results of the model error Δ_2 (Gaussian pulse, Gaussian spectrum, $DL = 1ns/mn$) (continued)

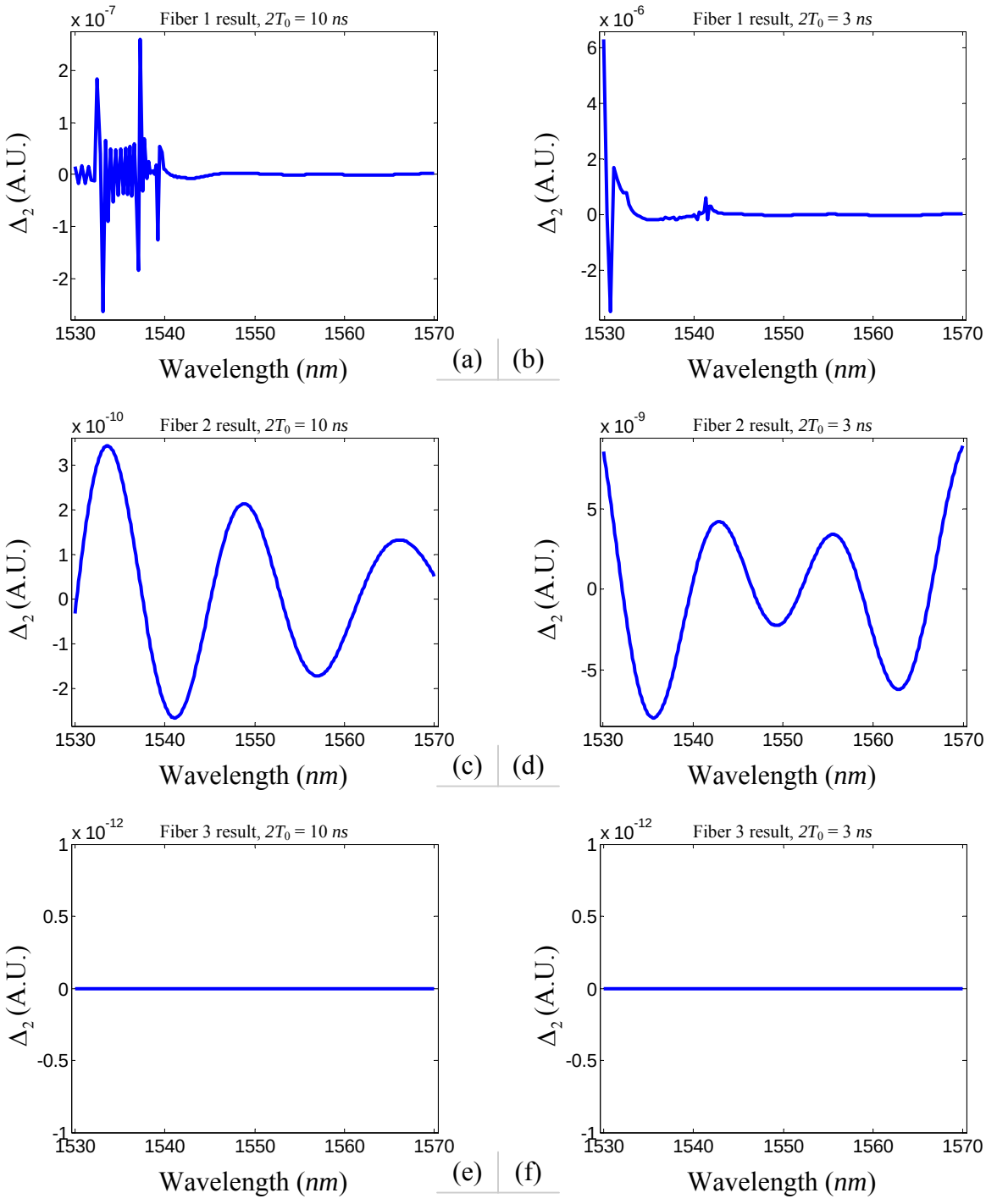

Figure A.19: Numerical simulation results of the model error Δ_2 (rectangular pulse, FP spectrum, $DL = 1ns/mn$)

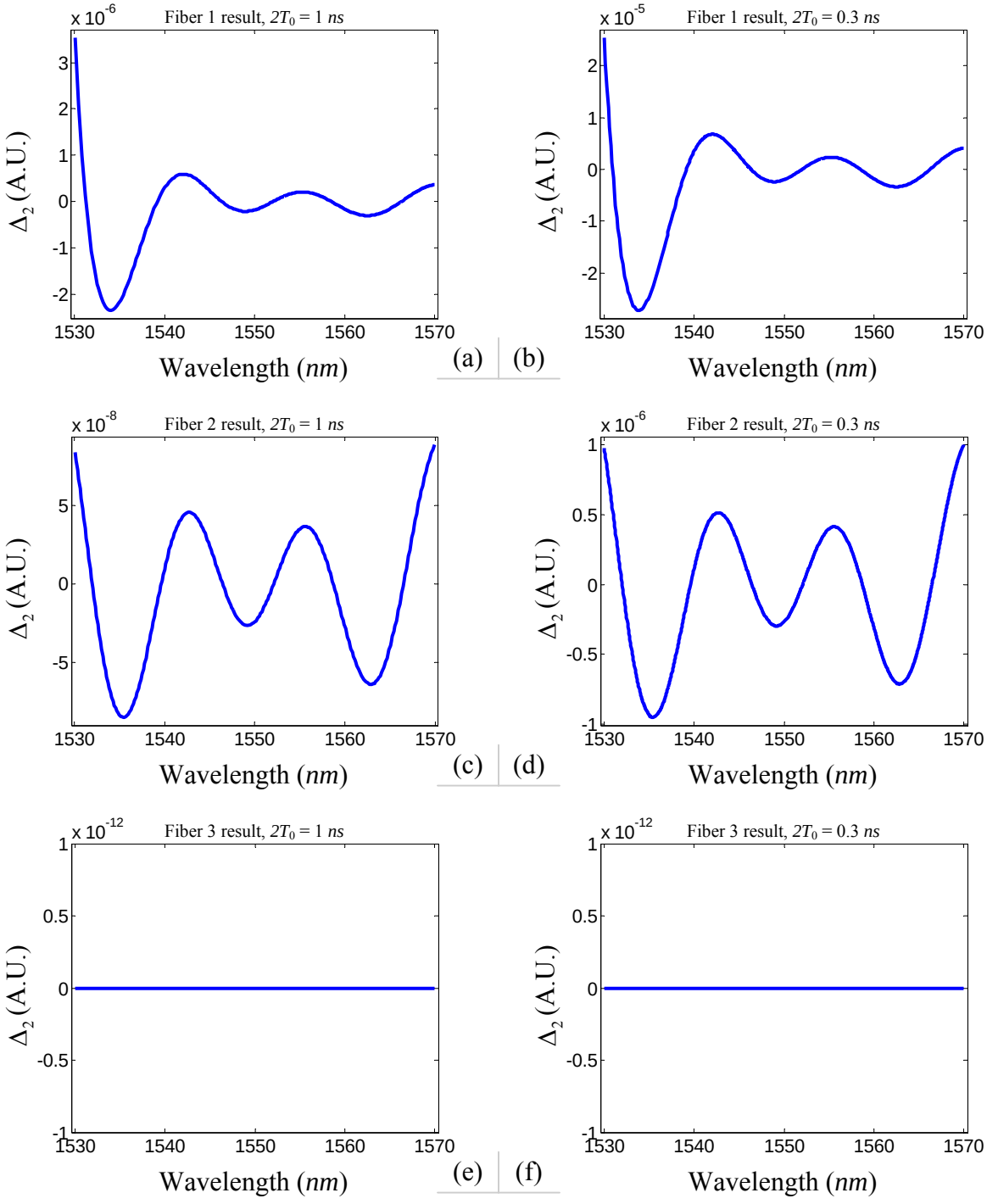

Figure A.20: Numerical simulation results of the model error Δ_2 (rectangular pulse, FP spectrum, $DL = 1ns/mn$) (continued)

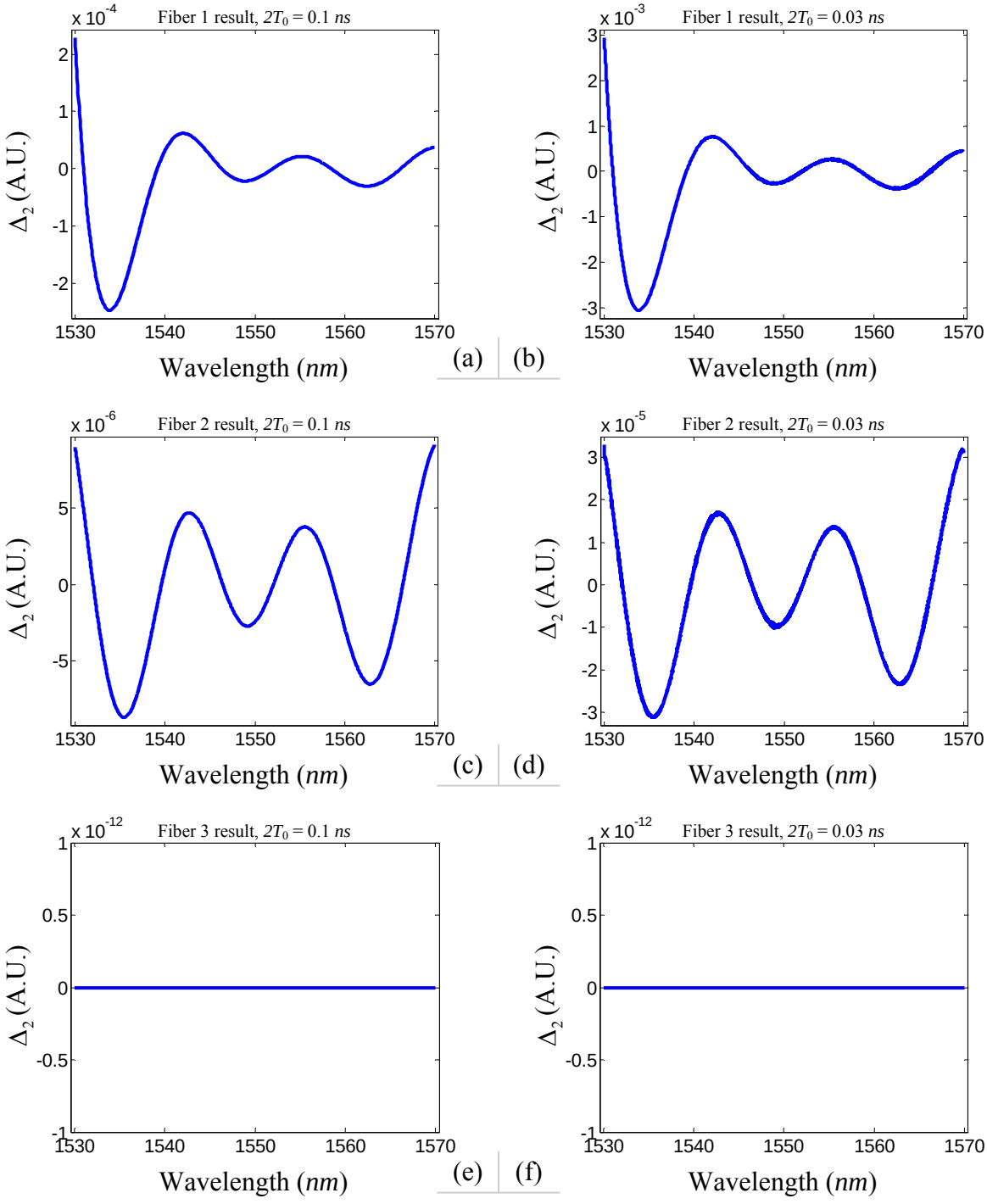

Figure A.21: Numerical simulation results of the model error Δ_2 (rectangular pulse, FP spectrum, $DL = 1ns/mn$) (continued)

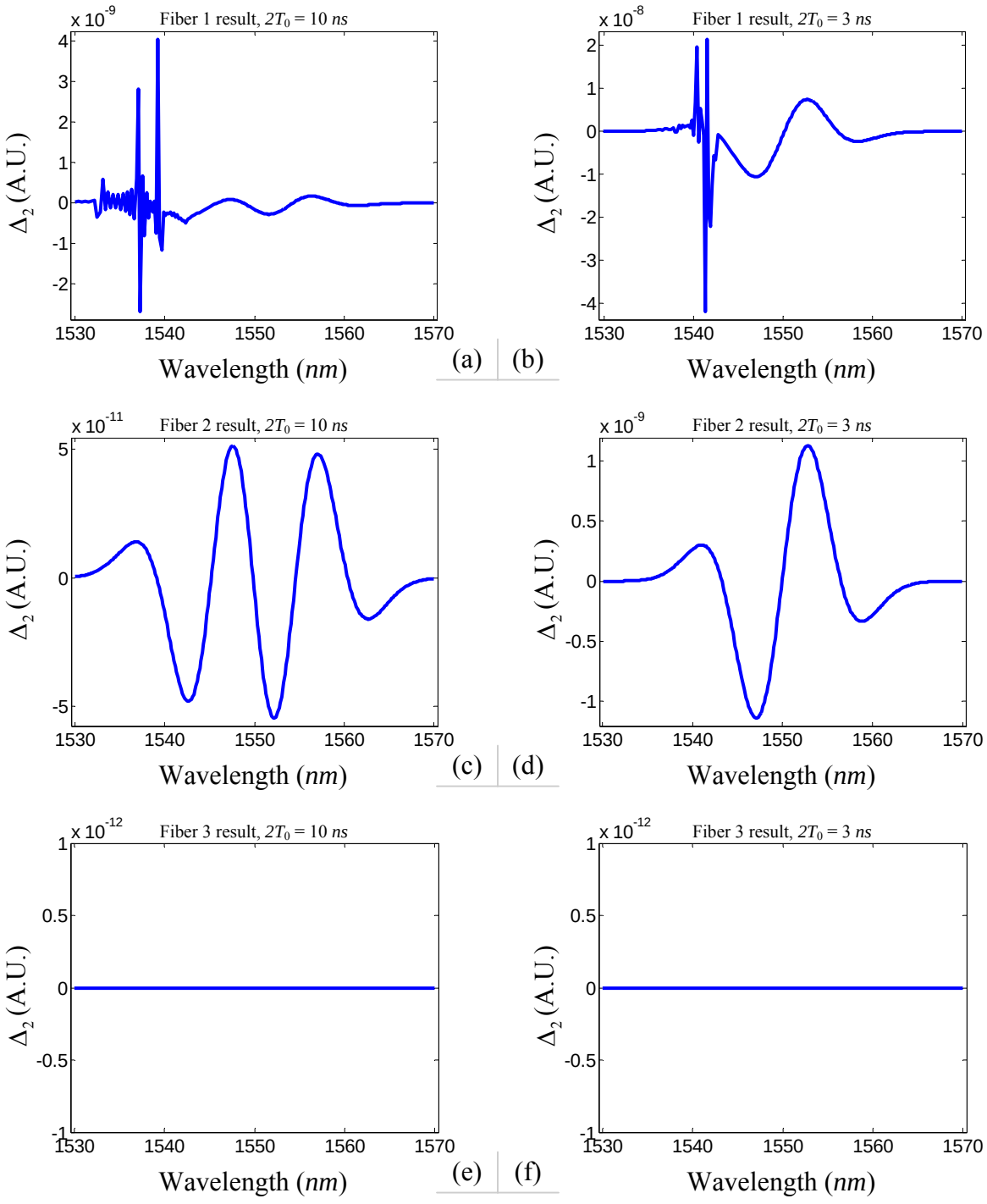

Figure A.22: Numerical simulation results of the model error Δ_2 (rectangular pulse, Gaussian spectrum, $DL = 1ns/mn$)

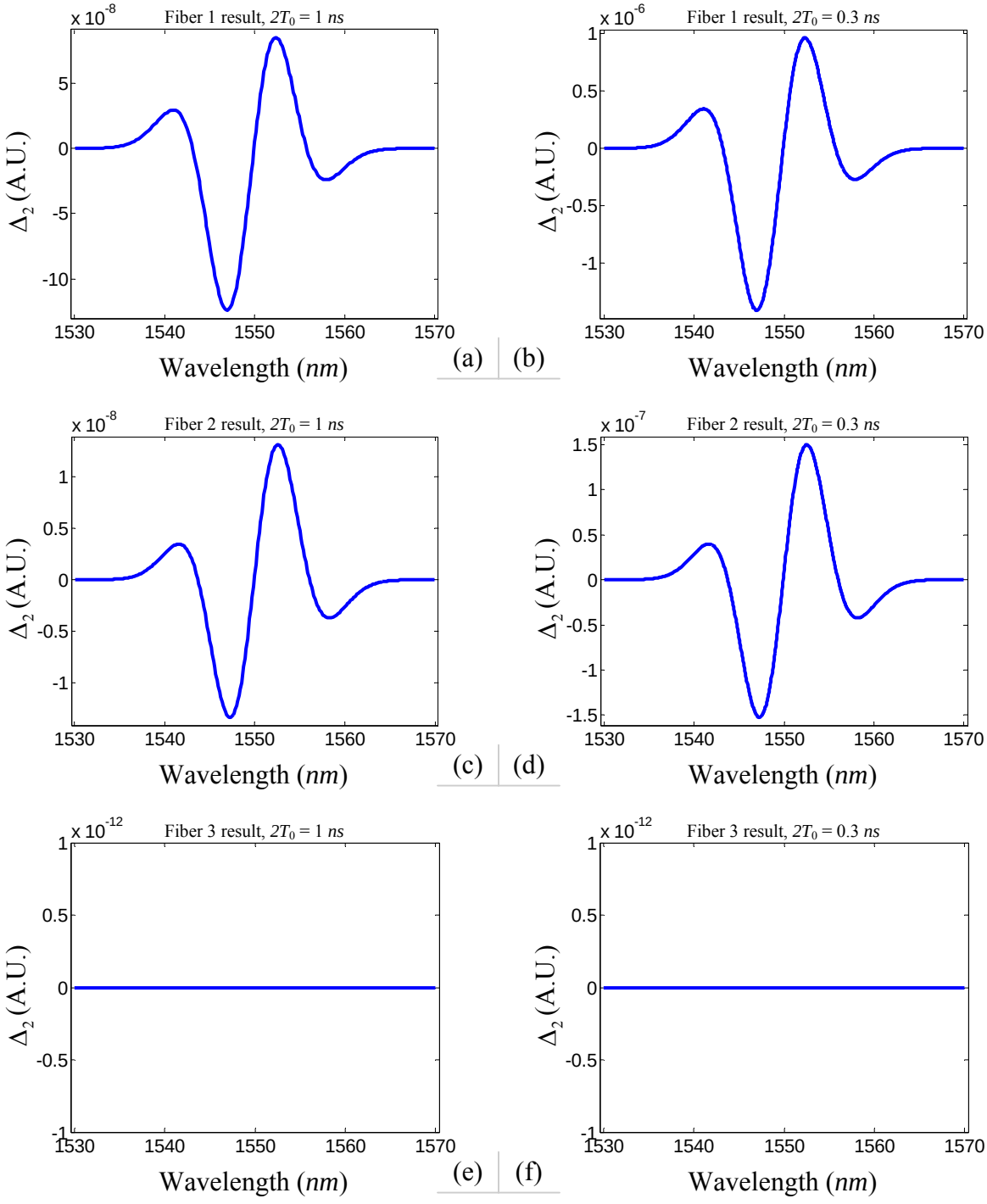

Figure A.23: Numerical simulation results of the model error Δ_2 (rectangular pulse, Gaussian spectrum, $DL = 1ns/mn$) (continued)

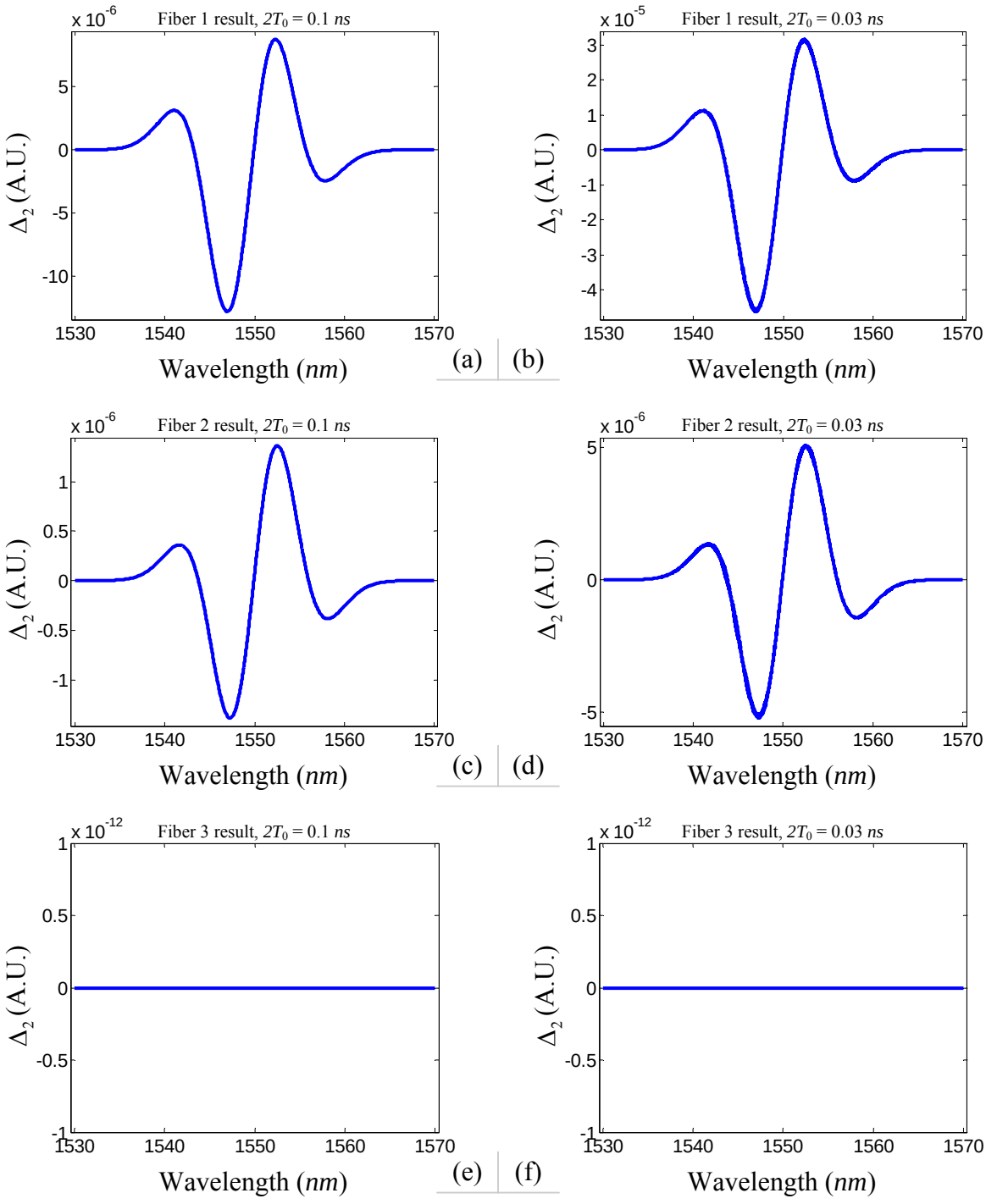

Figure A.24: Numerical simulation results of the model error Δ_2 (rectangular pulse, Gaussian spectrum, $DL = 1ns/mn$) (continued)

Appendix B

Additional numerical simulation results for resolution analysis

In the following simulation, three fibers with arbitrarily selected dispersion properties are used. The dispersion properties are listed in Table.4.1. The pulses used are Gaussian pulses and rectangle pulses. For the rectangle pulses, $C_L = C_R = 0.33$. All the spectral resolution value calculated at 1550 nm.

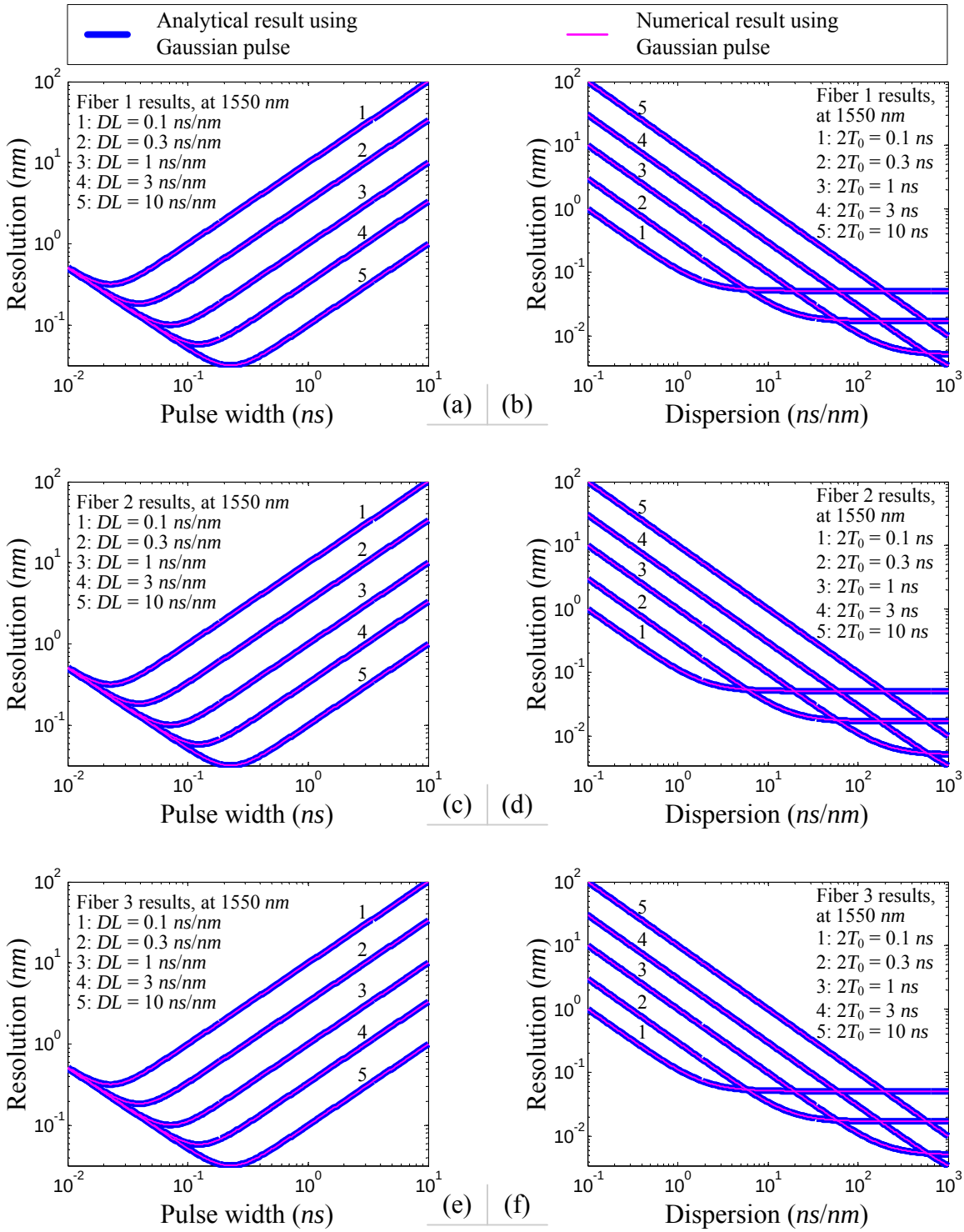

Figure B.1: Numerical simulation results of spectral resolution for Gaussian pulses

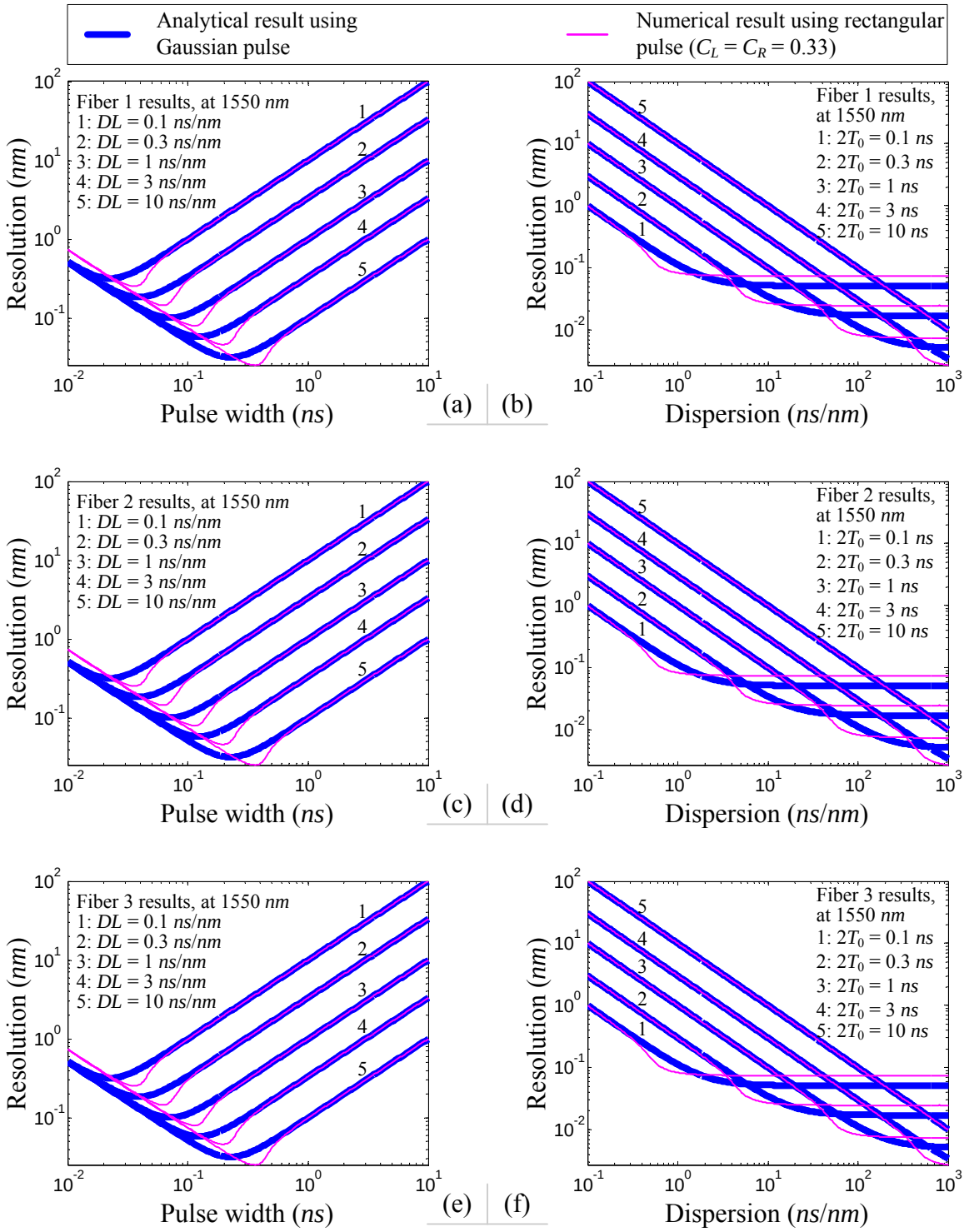

Figure B.2: Numerical simulation results of spectral resolution for rectangular pulses

Vita

Yongxin Wang was born in Beijing, China in 1975. He received his B.S. degree in Precision Instrument Engineering and M.S. degree in Optical Engineering from Tsinghua University, Beijing, China, in 1998 and 2001, respectively. From 1994 to 1997, he was with the National Key Laboratory on Precision Measurement Technology and Instruments, Tsinghua University, Beijing, China, where his research scope covered signal conditioning circuit design and wireless data transmission. From 1997 to 2001, he was a research assistant in the National Key Laboratory on Precision Measurement Technology and Instruments. His research was focused on the signal processing for high precision short distance laser range finding systems which covered the design, make and test of wide band amplifier, high speed digital circuits and mixed signal circuits. From 2002 to 2003, he was with the National Key Laboratory on Precision Measurement Technology and Instruments again, where his research was modeling and developing the optical interferometry system for high precision measurement.

In 2003, Yongxin Wang started his Ph.D. study in the Center for Photonics Technology (CPT) in the Bradley Department of Electrical and Computer Engineering at Virginia Polytechnic Institute and State University (Virginia Tech). He worked on many projects on fiber optic sensor signal processing, algorithm design, fiber sensor design and constancy test of physical constants. He was the originator and the key researcher of the high speed fiber optic spectrometers. He has authored and co-authored 6 journal and conference papers. He also holds more than 5 patents or patent disclosures.

He is a member of the IEEE and OSA.